PARTICLE VAPORIZATION VELOCIMETRY AND QUANTITATIVE SOOT CONCENTRATION MEASUREMENT IN SOOTY FLOWS

A Dissertation
Presented to
The Academic Faculty

by

Ping Yang

In Partial Fulfillment
of the Requirements for the Degree
Doctor of Philosophy in
Aerospace Engineering

Georgia Institute of Technology

December 2007

PARTICLE VAPORIZATION VELOCIMETRY AND QUANTITATIVE SOOT CONCENTRATION MEASUREMENT IN SOOTY FLOWS

Approved by:

Dr. Jerry M Seitzman, Advisor
School of Aerospace Engineering
Georgia Institute of Technology

Dr. Ben T. Zinn
School of Aerospace Engineering
Georgia Institute of Technology

Dr. Jeff Jagoda
School of Aerospace Engineering
Georgia Institute of Technology

Dr. Suresh Menon
School of Aerospace Engineering
Georgia Institute of Technology

Dr. James Mulholland
School of Civil and Environmental Engineering
Georgia Institute of Technology

Date Approved: March 28, 2006

ACKNOWLEDGEMENTS

I would like to, even beyond the words, express my deepest gratitude to my advisor, Dr. Jerry Seitzman. In the special time period of my Master and Ph. D study, and, life in Georgia Tech, his patient and knowledge, invaluable guidance and advice, even more than just a thesis advisor, helped me passed through and finished this thesis work. Second, I would like thanks Dr. Jeff Jagoda, who is also a member of my thesis reading committee, for his special help on my Ph.D study. I would also like to thank Dr. B.T. Zinn, Dr. Suresh Menon and Dr. James A. Mulholland for their many helpful comments and for taking an active part in my thesis committee.

I could not forget those persons who have helped me both on my school study and life during those special years in Georgia tech.

Rick, Kan, Shengquan & Yan couple, Tom Jenkins, Bobby, Cliff, David, Dmitriy, Gabe, Harry, Jason, John, Joshua, Mael, Mohan, Muruganandam, Nori, Priya, Qingguo, Rajesh, Randy, Rob, Ryan, Sasha, Santosh S., Santosh H., Shai, Shashvat, Satish, Thao, Tudor, Venkat and Yedidia. I would also like to thank my friends: Shibo Zhang& Lianghong Chen couple and their family, Zhiming Liu couple, Xianyu Hong couple, Yongchang Li couple and friends in my early time of study in Georgia Tech, Songtao Qiu, Guanpeng Xu, Liang Chen couple, Kejun Cai& Hongjuan Wang couple, Lei Wu, Qinghua Wang, for making my stay in Atlanta memorable.

I would like to acknowledge the following organizations for the support and funding of this work: National Science Foundation, MetroLaser. inc and AEDC.

Finally, I would like to thank my family for their love and support, which encouraged me at every step in my life.

TABLE OF CONTENTS

LIST OF FIGURES

LIST OF TABLES

SUMMARY

Soot is a combustion generated pollutant that is both a direct risk to human health and a contributing source to global environmental change. Soot can also be a controlling factor in heat transfer inside combustion systems. Thus there is a growing interest in being able to measure soot and understand its production in practical, turbulent combustion environments. Therefore, the specific objectives of this research work were: (1) developing a way to measure velocity of sooty regions that is compatible with existing methods for measuring temporally and spatially resolved soot concentration fields and (2) using these methods to make quantitative measurements of soot in an unsteady, turbulent-like combustor. The Particle Vaporization Velocimetry (PVV) technique was developed and is compatible with Laser Induced Incandescence (LII), a soot concentration measurement approach. PVV is a flow tagging approach, where a high intensity laser (~2-3 J/cm^2) is used to vaporize a small region in the soot field. This approach was demonstrated to produce a long lasting and easily readable flow tag that allows for velocity measurements over a wide range of velocities. LII proved to be the best method for detection the motion of the tag after a fixed delay. PVV and LII were used to measure velocity and two-dimensional soot concentration fields in an acoustically excited burner. In addition, images of soot luminosity were obtained. Both laminar and transitional acetylene diffusion flames were studied. The results reveal that strong acoustic forcing can significantly reduce total flame soot, as well as maximum soot concentrations, while simultaneously increasing the average soot temperature. The

influence of acoustically generated vortices on soot formation was studied, and soot and products mixture mostly likely dominant high soot concentration regions. Eventually, these mixtures will be propagated downstream and oxidized as a diffusion flame.

CHAPTER 1

INTRODUCTION

1.1. MOTIVATION

With the growing world economy, the use of fossil fuels, especially in rapidly developing countries such as China and India, is an important factor in economic development. With the growing consumption of fossil fuels, emissions from hydrocarbon-based, power generating processes are a topic of great concern, because they influence both human health and the environment. These emissions include SO_x, NO_x, complex hydrocarbons and particles generated by the combustion process, e.g., soot particles. All these emissions are controlled by the complex chemical and fluid mechanic processes of combustion. These pollutants are typically more dangerous in advanced industrial areas, where there is a relatively high population density.

Among these pollutants, particulate soot is one of particular concern. Particles are able to penetrate into human (and animal) respiratory systems. Especially fine particles (< 2.5 μm diameter) appear to be of primary importance for their ability to penetrate not only into indoor areas but to the depths of human respiratory systems,[1] such as lung capillaries and air sacs. These particles, sometimes in combination with other pollutants, can cause a number of significant health effects; these include aggravation of existing respiratory and cardiovascular diseases, development of new ailments and increased mortality.

In addition, emission of soot into the atmosphere can lead to global environmental problems. For example, particulate matter can cause damage and soiling of materials, and it is has been a major cause of visibility impairment in many parts of the U.S. and is a growing source in developing countries. Soot deposited on leaves of crops, trees and shrubs inhibits photosynthesis and plant growth. Soot in the atmosphere can also directly alter the earth's radiation balance. Soot particulates can directly trap infrared radiation (in solar radiation and from terrestrial emissions). Soot is also associated with enhanced cloud formation due to the increased number of cloud-condensing nuclei,[2] and clouds also act to alter the earth/solar radiation balance. Some recent reports also suggest that small soot particles inside the atmosphere could lead to cooling of the earth by reflecting sunlight back into space.[3] As scientists and decision makers have come to realize the seriousness of this problem, governments (both local and national) in many countries have issued increasingly restrictive laws limiting particulate exhausts from combustion sources. For example, the California Air Resource Board adopted the Diesel Risk Plan in September 2000, which established a goal of reducing 50% diesel PM (particulate matter) emissions by 2010.[4] Recently, the soot emission from aircraft engines is becoming a noticeable source of pollutant at high latitude. In facts, soot emission from military aircraft engines is also a significant infrared signature, which makes the aircraft more vulnerable to be tracked.[5]

The presence of soot particles within combustors is an issue of concern as well. They enhance the transmission of heat and radiation inside the burner. This is problematic in most propulsion and power producing engines. The presence of too many soot particles can also cause coating of surfaces, such as turbine blades and nozzles,

leading to enhanced erosion. Thus particles not only decrease system efficiency, but they can lead to shortened lifetimes of engine systems. However, increased heat transfer rates can be an advantage in devices like boilers and industrial heating systems. So there exists a challenge of controlling soot in combustors; for example, we might wish to enhance the heat transfer properties inside a combustor, while reducing soot emissions to the environment.

Thus, there is a growing interest in being able to understand the production of soot within combustors, especially in practical, turbulent combustion environments. This has also brought an awareness that *in situ* techniques for soot measurements are needed that can provide reliable information in unsteady combustion flows.

1.2. PREVIOUS RESEARCH

Among all flame types, laminar premixed flames have the simplest structure and steady chemical reaction rates; a standard example is the simple Bunsen burner. Understanding laminar premixed flames is a necessary perquisite to the study of turbulent flames, and they have been widely used to understand soot formation processes. There is a large body of experimental data that has been developed in order to elucidate mechanisms of soot initiation, growth and destruction in laminar flames. As summarized by Richter and Howard[6] and Mansurov[7], soot formation inside a flame consists of three major processes:

(1) The first step is nucleation of soot particles from gas phase species. Homann and Wagner[8] in 1967 and Crittenden and Long[9] in 1973, and Violi[10] in 2005 all suggested that acetylene and PAH (polycyclic aromatic hydrocarbons) play key roles leading to the initial molecular parents that form soot.

(2) The second step of soot formation is soot surface growth, which increases total soot mass and soot size simultaneously. Homann and Wagner[8], Benish,[11] and Kazakov and Frenklach[12] describe various possible chemical reactions in this step.

(3) The third process is particle coagulation. According to Frenklach,[13] colliding soot particles coalesce and form new (larger) spherical structures initially; then they agglomerate into fractal, chain-like structures.

Besides soot formation study in basic premixed laminar flames, some research has explored laminar diffusion flames. In 1978, Magnussen *et al*.[14] studied soot in acetylene jet flames. They examined the soot production response to changes in jet Reynolds number, dilution of the fuel with N_2 or water vapor, and fuel preheating. They reported the variation of Reynolds number had a strong effect on soot production. Adding N_2 or water vapor also could reduce soot production. Furthermore, they observed that soot destruction initialized at the boundary of eddies, with soot forming inside the eddies.[14] A light scattering technique was utilized in their experiments. Faeth *et al.*[15,16]experimentally studied soot formation in laminar diffusion flames with several different hydrocarbon fuels. They concluded that soot formed in laminar diffusion flames has similar surface growth rates and structures as that inside laminar premixed flames.

Despite the focus on laminar flame studies, the majority of practical combustion systems involve turbulent, nonpremixed combustion, principally because of the ease with which such flames can be controlled.[17] For example, simple jet flames are used in the making of glass and in cement clinkers. Swirling flows and diverging walls combustion systems are used in many industrial boilers. Flames inside diesel engines are produced by liquid fuel sprays. Overall, these are only a few applications of turbulent nonpremixed

flames; the whole list is too long to complete here. Inside these flames, chemical reactions are highly influenced by turbulence-driven processes. Since turbulent flow itself is a complicated phenomenon that has been studied for nearly two centuries, e.g., at least since the time of Osborne Reynolds,[18] the added complexity of turbulent flames, which combine complicated fluid mechanic, chemical and radiative processes, makes soot studies in turbulent combustion even more challenging.

1.2.1. Unsteady Forced Flames

As is well known, an important characteristic of turbulence is its ability to transport and mix fluid much more effectively than a comparable laminar flow.[19] Therefore, turbulence tends to enhance the mixing of gaseous oxidizer and fuel in nonpremixed flames. In fact, an abundance of studies on turbulent mixing processes has been published. In the literature, it has been demonstrated that an effective approach to simulate (in a controllable manner) important aspects of turbulent flow is to apply an acoustic forcing field to a laminar jet.[20-25] These studies showed acoustically generated vortices can play a critical role in the mixing process.

Alternatively, applying acoustic forcing to flame fields can modulate the flame conditions, i.e., by changing local flow velocity and fuel/air ratio, local soot production can be adjusted. Even though an acoustically forced (laminar) flame is not truly a turbulent flame, it is a very useful approach for controllably reproducing a number of aspects of turbulence. Attempts have been made to study soot formation and evolution in unsteady laminar flames. In the 1980s, Necker,[26] McManus,[27] and Santoro *et al.*[28] demonstrated that an acoustic system can fluctuate the velocity distribution inside a flowfield, similar to turbulent flow. It can generate vortices, thereby enhancing the mass

and energy transport processes and changing the flame surface, e.g., through improving fuel-air mixing. In the 1990s, Smyth[29,30] reported soot concentration changes in open flames measured with laser-induced incandescence, with and without pulsing of a laminar fuel jet. Low frequency (~10 Hz) actuation was used to generate flickering flames with three different hydrocarbon fuels, and the results suggested net soot production rates are highly fuel dependent in the flickering flames, likely due to variations in fuel residence time.

In 1992, Zinn[31] suggested acoustically forcing not only increases the combustion rate, but also lower CO and soot emission. In 1993, Kim[32] *et al*. investigated a pulsed C_3H_8 flame with schlieren photography and laser light scattering imaging techniques. Additionally, hot wire anemometry was used to measure the velocity profile close to the jet exit. They found that soot decreased after acoustic forcing. They noticed that a forcing frequency at the fundamental resonant frequency of the apparatus could vary the flow velocity most, generating the strongest vortices, which could cause ambient air flow to "collapse" inside the fuel tube. They called this "collapse mixing", which thereby inhibited soot chemistry.

It should be noted that most of the work on pulsed flames mentioned above was based on forcing the fuel jet instead of the whole burner. Near the jet exit, the acoustic forcing generates shear layer instabilities, forming vortex structures.[33] In the far field, buoyancy generated by high flame temperature is the dominant unsteady effect. [34]

In 2004, Ezekoye *et al*.[35] applied both high and low magnitude acoustic forcing to an entire chamber with an axisymmetric acetylene diffusion flame inside. Mainly based on laser extinction technology, the experimental results show that there exists a critical

acoustic velocity, *i.e.* below this velocity, local soot concentrations increase with increasing acoustic forcing; above the critical velocity, soot concentrations decrease with increasing of acoustic forcing. Furthermore, they compared soot inside the forced jet flame with partially premixed flames, and suggest a partial premixing mechanism is responsible for the soot variation inside the cyclically forced flame. Furthermore, direct acoustic forcing of an incinerator has been shown to effectively enhance flame radiation and reduce soot emissions.[36]

1.3 SOOT DIAGNOSTICS

1.3.1. Soot Concentration Measurement Techniques

To examine soot production inside flames, local soot concentration measurements are necessary. There are a number of established techniques for measuring soot properties, including physical sampling methods,[37, 38] and laser scattering and extinction.[28, 39] Physical sampling methods provide useful information on soot properties such as chemical composition and structure, which are harder to ascertain from nonintrusive techniques. However, physical sampling is naturally intrusive; local flow parameters can be changed by the presence of the probe, thus generating measurement uncertainty. In addition, real-time information is hard to obtain with sampling probes, due to the time delay and effective averaging inherent in most approaches. Other techniques, like laser scattering and laser extinction are nonintrusive diagnostic techniques.

Laser light scattering from soot particles is an imaging technique with good spatial and temporal resolution, thus making it especially useful for fluctuating or turbulent flows. However, it uses elastically scattered light, and in the many combustors, laser scattering is susceptible to large background interferences from ambient dust,

reflection from windows and other particles such as liquid droplets. Also, the scattering signal intensity is very sensitive to the effective optical diameter of the soot particles.[40] The scattering signal is weighted more towards bigger particles.

The extinction technique is different from scattering, in that it is primarily proportional to the soot mass, or effectively volume, of the soot that the light beam encounters along a line of sight.[40] Because the soot particles in flame and exhausts are generally much smaller than the wavelength of the light source, the total amount of light absorbed by soot particles is almost independent of particle size.[40] If the soot concentration in the measurement region is very low, it is very difficult, however, to detect the small loss in the laser intensity. Also, dust in normal air can be a source of background extinction. As a line-of-sight technique, extinction also has poor spatial resolution along the beam path.

Laser-induced incandescence (LII) is a relatively new, nonintrusive, laser-based technique.[41 42] It detects the radiation signal emitted from laser heated, high temperature particles. The LII technique combines the advantages of both scattering and extinction. Like elastic scattering, LII is an imaging technique with excellent spatial resolution, and it provides a strong signal. Since the signal primarily corresponds to the amount of laser energy absorbed, LII, like extinction, is mostly sensitive to the soot mass concentration (or volume fraction for a known soot density). Generally, LII signal data acquisition time is very short (less than 1 μs, and usually less than 100 ns). Thus LII images can be used to determine nearly instantaneous, *in situ*, soot field information; this is especially useful in turbulent flame measurements, where local velocities can be very high and time scales

small. In addition, extensions of LII have also been developed for particle size measurements.[18, 19]

1.3.2. Velocity Measurement

To control total soot emission from combustor, soot production rate need to be measured, that is to say, soot velocity needs to be measured besides soot concentration. In addition, local soot production rate can be calculated based on local soot concentration and soot flow velocity.

For flow velocity measurement, there are a number of established techniques; all have their individual advantages and drawbacks in combustion and soot laden flows. Probe techniques, such as hotwires, are problematic; for example they are prone to soot coating and clogging. In addition, single-point measurements have limited utility in unsteady combustion, where field measurements provide added spatial information.

A number of nonintrusive, optical techniques have been developed for velocity measurement. Most require, however, a single particle in the detection volume[43] (or in a pixel for imaging methods).[44,45] These include Laser Doppler Velocimetry (LDV) and Particle Image Velocimetry (PIV), with the latter providing at least two-dimensional maps (planes) of two velocity components. Unfortunately, these methods have limited applicability in flows with dense particle loadings. For particles no bigger than 100 nm and generously small measurement volumes, both LDV and PIV are normally limited to particle volume fractions below ~0.1 ppb. In addition, these techniques cannot generally be used to discriminate between particles of different elemental composition; all particles that elastically scatter contribute to the signal. Thus application in soot laden flows can be problematic.

For gas velocity measurements, a number of other optical techniques have been developed to remove the need for particle seeding. These can be categorized as flow tagging velocimetry, [43,45] and include Ozone Tagging Velocimetry (OTV) and Hydroxyl Tagging Velocimetry (HTV). These techniques rely on creation of tagged regions (marks) in the flow (a line, crossing lines, grids, etc.) at some initial time. The locations of the marked regions are then interrogated at some known time delay, usually by a planar imaging technique. The displacement of the regions is used to determine the velocity component(s) in the plane of the imaging sheet. But OTV and HTV are limited in their applicability. OTV can not be used in high temperature flows, such as combustors, turbine and exhaust flow. HTV, which relies on photodissociation of water to create OH, can not work in cold regions where there is no hot H_2O, or in regions where OH is rapidly consumed by chemical reactions, for example in soot oxidation zones.

Therefore, there is currently no optimum optical technique for achieving velocity measurements in sooty flows.

1.4 OBJECTIVES OF RESEARCH

1.4.1. Development of a New Laser Based Velocity Measurement Technique (PVV)

The first objective of the current work is development of a laser-based technique for velocity measurements in sooty flames that is compatible with LII for nearly simultaneous soot concentration measurements. The approach developed here is based on soot particle vaporization induced by a high intensity laser pulse. A soot free region can be produced and used for flow tagging velocimetry. The thesis examines various experimental issues necessary to explore the utility of the approach and to determine the optimum experimental conditions. These include the optimum laser intensity for creating

the marking region, the marking region life time (longer lifetime permit more accurate velocity measurements at low speeds), and is the best method of detecting the marking region.

1.4.2. Quantitative Soot Measurements in an Acoustically Forced Flame

The second objective of this thesis is to apply quantitative soot diagnostics (for concentration and to some extent velocity) to understand the effects of acoustic excitation that lead to the reductions in soot emissions and changes in radiation observed in Ref. 36. The approach to this objective is to study a fuel jet flame under different Reynolds number conditions, with and without acoustic forcing of the combustor. By examining the soot distribution and soot structure inside the forced flames, the interactions between the flowfield and the soot production will be determined.

1.5. THESIS OUTLINE

The remainder of this thesis is composed of the following chapters. Chapter 2 provides a brief and basic background for soot formation and destruction mechanisms. I also introduce the principles and theoretical background for the LII technique, laser vaporization of soot, and for soot detection techniques. Chapter 3 describes the experimental setup, including the combustors and flowfields employed, the measurement devices used, and some of the data reduction procedures. Chapter 4 presents the development of the Particle Vaporization Velocimetry (PVV) technique, including characterization experiments in various flows and velocity measurements in an acoustically forced burner. Chapter 5 presents quantitative soot concentration measurement inside the acoustically excited combustor. Chapter 6 concludes the thesis

with a presentation of the outcomes of this research and recommendations for future work.

CHAPTER 2

BACKGROUND OF SOOT FORMATION AND SOOT DETECTION TECHNIQUE

In this chapter, the basic concepts for soot formation and destruction, and LII Laser diagnosis technique are briefly introduced.

2.1. SOOT FORMATION AND DESTRUCTION PROCESSES

Soot is carbonaceous particles formed in gas-phase combustion by fuel rich reactions. The normal soot particles are mostly composed of graphitic carbon material. Under electron microscope examination, soot appears as aggregated, branched chain-like structures, and composed of groups of primary particles, which are approximately spherical and have diameters on the order of nanometers to tens of nanometers.[46]

The soot formation and oxidation can be described by a "hydrocarbon polymerisation theory", as stated by Gaydon,[47]

> In the presence of excess of fuel molecules, free radials initiate chain polymerisation processes which lead to the formation of higher hydrocarbons which decompose thermally to solid carbon and hydrogen. In the presence of sufficient oxygen the radicals are removed by reaction with this and do not cause so much polymerisation.

Different fuels have different sooting tendency, and there are many different soot formation mechanisms proposed for different fuels. The mechanisms involve many

chemical and physical steps. Currently, the soot formation steps are generally considered to be the following: (1) formation of initial molecular soot precursors, (2) condensation and surface growth, (3) coalescent coagulation to form larger primary particles, (4) agglomeration of primary particle to form branched soot particles. Figure 2-1 shows a schematic of the general soot formation process

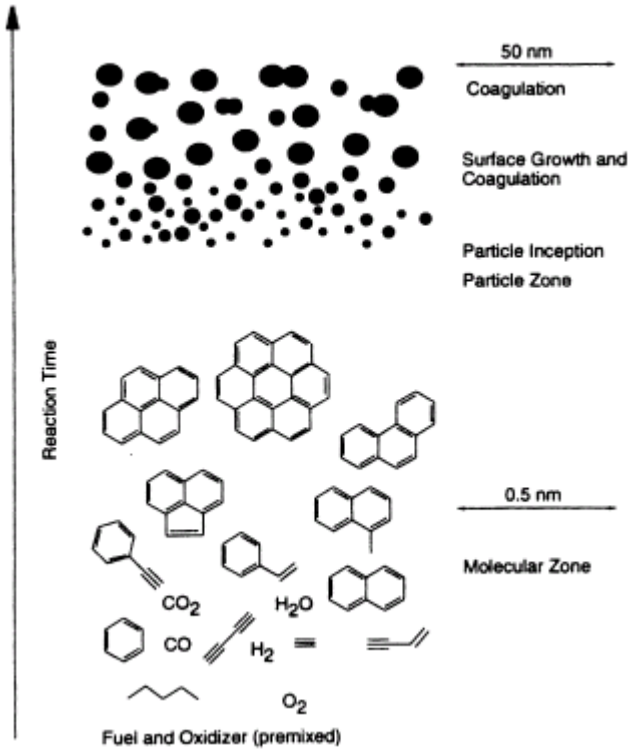

Figure 2-1. Soot formation processes in premixed flames from Ref. 48.

2.1.1 Soot Formation in Acetylene Flames

Acetylene was chosen to be the fuel in the current study. Acetylene is usually considered an important soot precursor species in most hydrocarbon combustion systems.[49] During pyrolysis, acetylene molecules can form highly active small radicals, such as C_2H and C_2H_3. These radicals continue reaction with each other or other acetylene molecules and then form polyacetylene (including polyacetylene radical) molecules. The nonstop reaction between these radicals and acetylene molecules, with

removal of H, leads to the formation of aromatic rings and polycyclic aromatic hydrocarbons (PAH). Mass growing of high mass PAHs via physical or chemical condensation forms the incipient soot particles, which can evolve to (larger) primary soot particles through surface reactions with gas-phase molecules or coagulation between small incipient soot particles. Branching agglomeration of primary particles forms large soot particles. The soot formation processes in acetylene flame are illustrated in Figure 2-2.

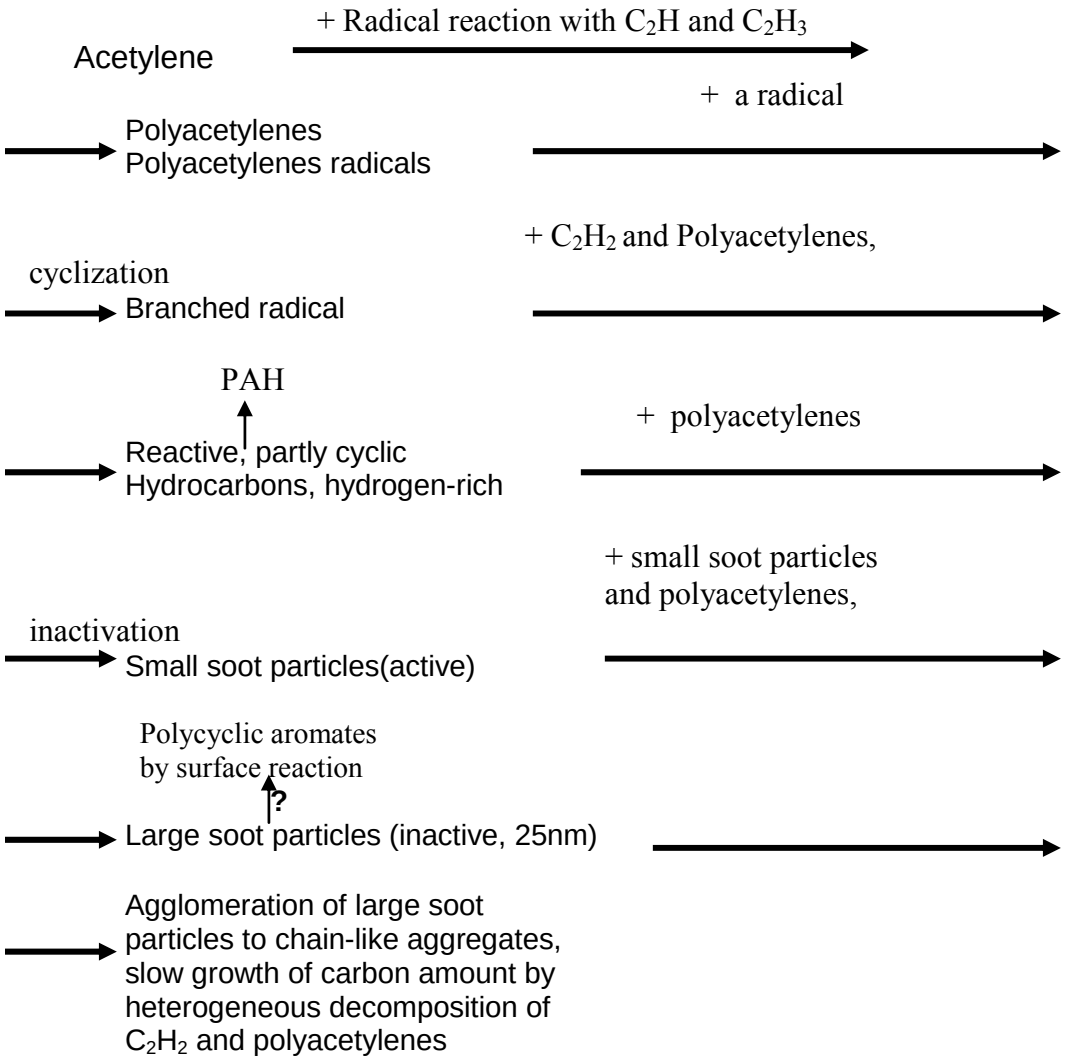

Figure 2-2. Soot formation processes in acetylene combustion (after Ref.50).

2.1.2 Thermodynamic Property Effects on Soot Formation

Temperature:

Soot formation is initialized at 800-1000ºC. During the soot formation processes, temperature plays a very important role. In premixed flames, oxidation rates increase faster than pyrolysis rates. Thus the higher the flame temperature is, the lower the sooting tendency. In pure diffusion flames, there is no oxidizer contacting the fuel region; thus the flame's sooting tendency increases with an increase of temperature.

Pressure

In diffusion flames, variations in pressure only have minor effect on the soot formation process. However in premixed flames, soot formation is found to be proportional to $p^{1.25}$ (Ref.51).

2.1.3 Soot Formation Time Scales

In premixed flames, the total soot formation process usually occurs in 10-30 ms.[52] Similarly, the soot formation time in diffusion flames is closer to 15ms.[53] These times are about one order of magnitude larger than the characteristic time-scales for combustion reactions, but shorter than the time-scales of molecular transport.[54]

The actual soot formation time scales for each step in acetylene flames are currently unknown. **Error! Reference source not found.** shows measured time scales from diesel engines; it provides fundamental time scales for most important soot formation processes, and can be used as a reference for soot formation study.

Table 2-1 Time scales of soot formation steps in diesel engines (from Ref. 55).

Processes	**Time range/stage**
Formation of precursors/Nucleation	~few μs
Coalescent coagulation (~10-fold)	~0.05ms after local nucleation
Spherule identity fixed	coalescence ceases
Chain-forming coagulation	~few ms after coalescent
Depletion of precursors	~0.2ms after nucleation
Non-sticking collisions	~few ms after nucleation
Oxidation of particles	~4ms
Combustion cycle complete	~3-4ms
Deposition of hydrocarbons	During expansion and exhaust

2.1.4. Soot Oxidation

Soot is removed in flames through an oxidation process, in which soot mass (i.e., carbon) forms CO and CO_2. In premixed flames, soot oxidation and formation can occur simultaneously; in diffusion flames, soot oxidation typically occurs after most of the soot is formed and enters the oxidizing region near the flame front. OH is normally considered the main oxidizer in fuel rich conditions, while O_2 is the primary oxidizer for fuel lean gases.[6] Thus in diffusion flames, soot is initially oxidized by OH as the soot approaches the heat release region.

2.2. PULSED LASER INTERACTIONS WITH SOOT

If a laser beam of wavelength λ intersects soot particles of diameter a_p, the soot particles can absorb energy from the laser beam. According to the Rayleigh theory, if the particle size is much smaller than the incident wavelength ($a_p << \lambda$), more energy will be absorbed and stored inside particle than scattered, and the particle absorbs light energy volumetrically instead of surface refraction.[40]

When the soot particle is exposed to the laser beam, especially a high intensity, pulsed laser, the small soot particle can volumetrically absorb great amounts of laser energy. For a high power laser, the heating rate greatly exceeds the heat loss rate, which includes heat conduction to the surrounding gas and radiation, the soot temperature is increased rapidly, and the soot particle can reach very high temperatures. At elevated temperatures, the soot particle begins glowing, emitting broadband radiation. This broadband emission, caused by laser heating, is called Laser Induced Incandescence (LII). If the laser intensity is high enough, the soot particle can approach (or even exceed) its vaporization temperature (nominally 3915 K for carbon black). When this happens, the soot vaporization grows rapidly and most of the additional laser energy absorbed by the soot particle is lost via vaporization. After the laser pulse ends, cooling mechanisms dominate, and the soot temperature decays over a relatively short period before reaching equilibrium with the ambient gas temperature.

For high enough laser energy, the soot particles can be significantly vaporized before the laser pulse ends. The decrease in soot particle size or mass due to vaporization will lead to less radiative emissions. So, there are two offsetting influences on the LII signal: laser energy increase will increase the particle temperature, which increases the radiation, but soot particles vaporization reduces the amount of radiating material and thus decrease the LII signal.

2.3. BASIC EQUATIONS OF LII MODELING

The original modeling of the LII process was developed by Eckbreth[56] while Melton,[57] Hofeldt,[58] and Mewes and Seitzman[59] modified it later for simulating the

detected LII signal. All the numerical simulation results in this chapter are modification from Mewes' simulation code.

The physical assumptions for the models are: 1) the primary particle is spherical; 2) its chemical composition and physical properties are homogeneous, i.e. composition, mass density, temperature, refractive index are uniform during the process of simulation; and 3) the ambient air is homogeneous. During onset and after the laser pulse, the heat balance is dominated by heat gain and heat loss mechanisms of the soot particles. Heat gain is energy absorption from laser beam, and the heat loss includes heat conduction between soot and ambient air, soot vaporization with latent energy consumption and radiation. The mass balance includes soot mass loss due to vaporization.

The energy balance equation is given by:

(Eq.2-1)
$$m_p c_s \frac{dT_p}{dt} = \alpha_{\lambda,p} q \pi \frac{a_p^2}{4}$$ (Energy stored inside particle)

$$-\frac{\Delta H_v(T_v)}{W_v}\frac{\pi}{2}\rho_s a_p^2\left[-\frac{1}{\rho_s}\left(\frac{2W_v}{\Re T_v}\right)^{\frac{1}{2}} p^* e^{\frac{(\Delta H_v(T_v))(T_v - T^*)}{\Re T_v T^*}}\right]$$ (vaporization)

$$-\frac{\pi a_p^2}{4} h \frac{(T_p - T_\infty)}{a_p/2}$$ (heat conduction)

$$-\frac{\pi a_p^2}{4}\int_0^\infty \alpha_{\lambda,p}\left[e_{b,\lambda}(T_p) - \varepsilon_{\lambda,e} e_{b,\lambda}(T_e)\right] d\lambda$$ (radiation)

The heat conduction term of (Eq.2-1) can be rewritten as:

(Eq.2-2)
$$-\frac{\pi a_p^2}{4} h \frac{(T_p - T_\infty)}{a_p/2} = -\frac{\pi a_p^2}{4}\frac{1}{(1+GKn)} k_\infty(T_\infty)\frac{(T_p - T_\infty)}{a_p/2}$$

$$= -\frac{\pi a_p^2}{4} \frac{1}{(1+\frac{2(9\gamma-5)}{\alpha(\gamma+1)}\frac{\lambda_{mfp}(T_\infty, p_\infty)}{2a_p})} k_0 (\frac{T}{T_{k0}})^{\frac{3}{2}} \frac{T_{k0}+S_k}{T+S_k} \frac{(T_p - T_\infty)}{a_p/2}$$

where G is the geometry factor for spherical particles and was provided by McCoy,[60] where α is thermal accommodation factor and γ is the specific heat ratio. In (Eq.2-1), the black body spectral emissive power for radiation term can be calculated from Plank's formula[61]

(Eq.2-3) $$e_{b,\lambda}(T_p) = \frac{2\pi hcn_\infty^2}{\lambda^5} \frac{1}{e^{\frac{hC}{\lambda k T_p}} - 1}$$

The mass balance, first developed by Eckbreth,[56] has the particles mass decrease rate equal to the mass flow rate of vaporized material away from the surface of the soot particles. The mass balance equation is:

(Eq.2-4) $$-\rho_s \frac{\pi a_p^2}{4} \frac{da_p}{dt} = \frac{\pi a_p^2}{4} \sqrt{\frac{\Re T_v}{2W_v}} \frac{W_v p^* e^{\frac{\Delta H_v(T_v)(T_v - T^*)}{\Re T_v T^*}}}{\Re T_v}$$

Notice here, both the energy and mass equations are ordinary differential equations, and are functions of time. This means the radiation or LII signal can vary with time.

As mentioned before, the soot particle will be vaporized and its size will decrease if the laser intensity is high enough. Figure.2-3 shows simulations for a 30 and 50 nm particles illuminated by a 1 J/cm^2 laser beam. The applied laser corresponds to the infrared (IR) output of a Nd:YAG laser, with a 1064 nm wavelength. Its intensity is assumed uniform across the beam, and the pulse width (FWHM) is 7 ns. It shows that appreciable particle vaporization occurs at ~7 ns from the onset of the laser pulse, which is earlier than the peak intensity time (~14ns). The particle vaporization ends at 19 ns,

before the laser pulse ends (~28ns). These results show that only the high intensity portion of the laser pulse can heat soot particle hot enough to be vaporized. Moreover, at the same laser intensity of 1 J/cm^2, the larger particle size (50nm) is decreased to 34nm (a factor of 32% in size, or ~70% in mass), which is more than for the smaller (30nm) particle. The latter one changes from 30 to 22 nm (27% in diameter and 60% in mass). The reason for the soot particle size dependence is that for these small particles (in the Rayleigh limit where at $a_p << \lambda$), the particles absorb laser energy volumetrically but the mass loss depends in part on the soot area (see Eq. 2.4).

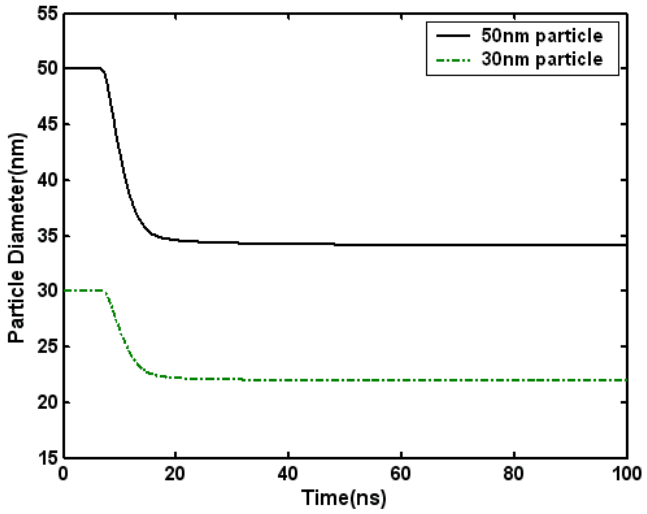

Figure.2-3. Numerical simulation of particle sizes change with time, initialized at the onset of laser pulse (laser intensity of 1 J/cm^2).

Figure 2-4 displays the numerical simulation results of soot particle size change for various laser intensities. Two different initial soot particle sizes are considered. Obviously, the particle size (and mass) decreases more for increasing laser power. Also, the larger particles (50nm) decrease faster than smaller particle (30nm), as shown above. In both cases, however, the highest energy shown (3 J/cm^2) is sufficient to reduce the soot mass by at least 90%.

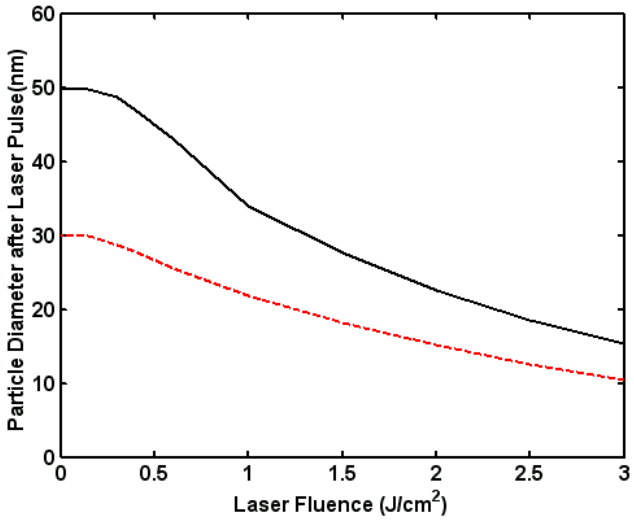

Figure 2-4. Numerical simulation results of soot particles diameter variation after illumination by pulsed laser at various intensities. Black line represents 50 nm particles and red dot line is 30nm particles (1064 nm laser).

Figure 2-5 displays particle temperature histories after onset of the laser pulse. The two curves show the same original particle size (50nm) heated by different laser intensities, 0.3 and 3 J/cm^2. First, these curves clearly show that the higher laser intensity can "overheat" the particles, to temperatures above the equilibrium vaporization point. This leads to rapid vaporization and loss of more particle mass or size, then particle temperature variation with time will follow smaller particles' trace and drop faster. Second, the higher power (3 J/cm^2) laser pulse produces the maximum soot particle temperature at ~7ns. After that, vaporization dominates; consumption of vaporization latent energy and a reduction the laser's heating slope decreases particle temperatures. For the lower power laser (0.3 J/cm^2), however, only a small amount of mass is vaporized. Thus, soot particle temperatures can keep increasing, and the peak temperature is reached about where the laser intensity peaks (~14ns).

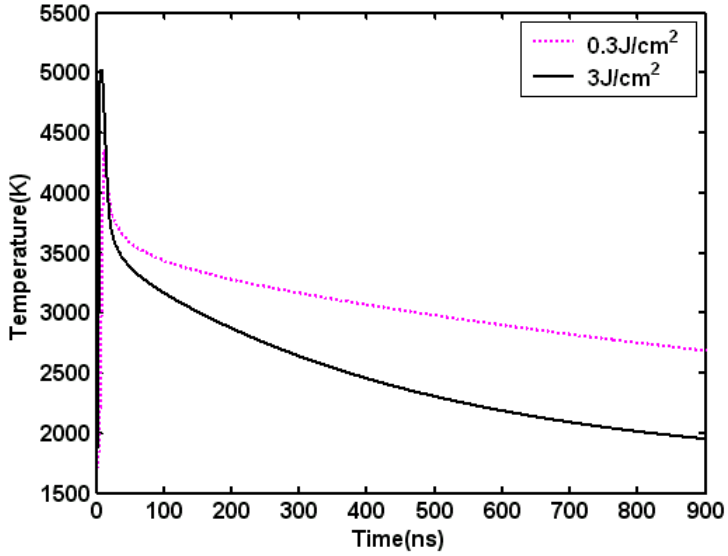

(a)

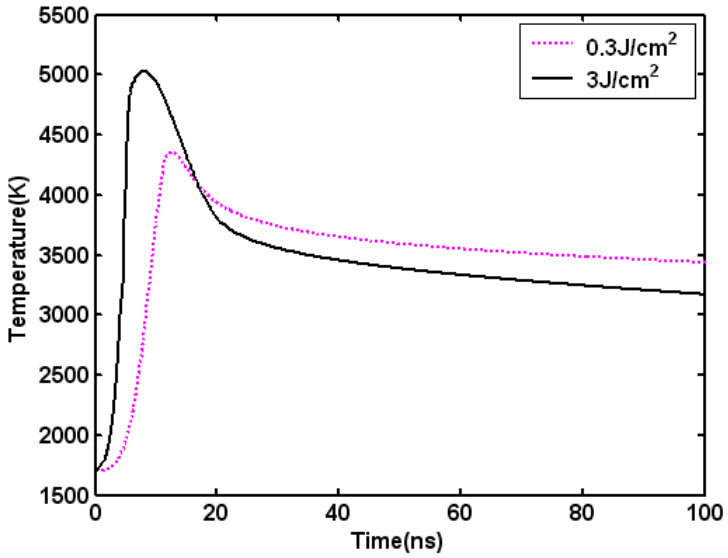

(b)

Figure 2-5. Numerical simulation results of particle temperature (for 50nm original particle) versus time at different laser intensities, initialized at the onset of the laser pulse; (b) shows 0-100 ns portion of (a).

In actual experiments, the LII signal (Eq. 2.5) is normally gated over some specific time interval, such as 50ns. This short interval usually begins at or close to the laser pulse onset, where laser heating is the strongest, so the LII signal is close to its peak.

(Eq.2-5)
$$S(t_1,t_{2,},T_{P,0},a_{p,0},\mathrm{I}_t,\lambda_{\mathrm{det}})=\frac{\Omega}{4\pi}\int_{t_1}^{t_2}\pi a_p^2\int_{\lambda_{\mathrm{det}1}}^{\lambda_{\mathrm{det}2}}G_\lambda\alpha_{\lambda,p}\varepsilon_{\lambda,p}e_{b,\lambda}(T_e)d\lambda dt$$

CHAPTER 3

EXPERIMENTAL METHODS

To measure soot emission rate (soot flux) in sooty flow, both soot concentration and velocity need to be measured. Comparable to soot concentration measurement, sooty flow velocity measurement technique needs to be developed. In this chapter, the experimental facilities and the velocity measurement techniques are introduced. Descriptions are given for the three flows facilities employed: a non-reacting soot generator, a laminar flame burner and an acoustically forced combustor. The nonintrusive measurements are mainly based on Laser Induced Incandescence (LII), and a related technique, Particle Vaporization Velocimetry (PVV). The optical setups and experimental details are presented for both.

3.1 FLOWFIELDS

In order to develop and characterize the PVV technique, two flowfields were employed. The first is a nonreacting, carbonaceous aerosol containing flow, which has been applied for simulating combustion exhausted; the second is a commonly utilized, well-documented, steady laminar diffusion flame. Since the laminar flame burner has been studied in detail in the literature, it is also useful as a calibration standard for quantitative soot concentration measurements, and it is also used for this purpose in the current study. Finally to test the PVV technique for multidimensional measurements and to study soot in an unsteady combustor, an acoustically driven, nonpremixed burner was developed. The burner is capable of producing both laminar and turbulent jet flames.

Together with an acoustic forcing system, the combustor can simulate the unsteady combustion processes inside practical combustion systems.

3.1.1 Soot Generator

In order to develop and characterize the PVV process initially, it was advantageous to use a flowfield that was laminar and nonreacting, and where the soot concentration and particles size can be controlled. To this end, a soot aerosol generator was used to create a controllable soot field (Figure 3-1).[68] The soot generator provides a nonreacting flow with an aerosol of carbon black particles, which are sufficiently diluted to avoid signal trapping. It is also designed to be nearly uniform in temperature, concentration, and particle size. The aerosol is obtained from the following process: 5.6 grams of carbon black are mixed into one liter of distilled water, together with one mL gum arabic (Winson & Newton) added as an emulsifier. The carbon black (Cabot 800) is composed of approximately 17 nm particles.

This solution is atomized with the use of an aspirator/impingement type nebulizer (Inspiron), providing a carbon/water fog, which is then diluted by a secondary airflow. The solution is aspirated with air at a constant flow rate of 9.2 L/min, yielding a solution flow rate of 0.34 mL/min. Each flow is separately directed into an aluminum drying cylinder (76 mm diameter, 600 mm long) held vertically, with a 2.6 cm wide and 2.4 meter long heavy insulated heating tape (Omega Engineering model FGH101-080) wrapped around it. The cylinder and heating tape together are surrounded by thermal insulation materials. To evaporate the water droplets, the cylinder is heated by the heating tape to a nominal temperature of 110ºC. Finally, the dried carbon particles follow the airflow, exiting the top of the drying cylinder via a 300mm long aluminum tube, with a

17 mm inner diameter. Measurements are made above the end of the tube in the resulting sooty jet.

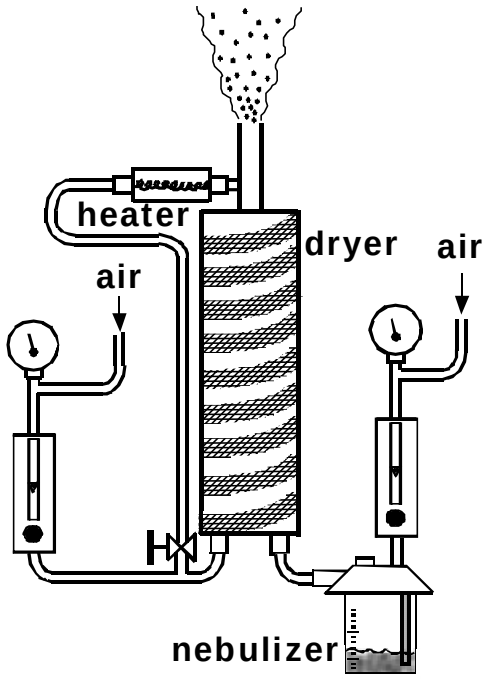

Figure 3-1 Soot generator schematic: dryer tube is wrapped with heating tape; separate air flowrates are monitored with rotameters and pressure gauges.

Dilutions in soot concentration can be achieved by either increasing a second airflow (see figure), or by diluting the carbon/water dispersion. The second method, however, also changes the size of the carbon particles produced. As a carbon laden water droplet evaporates, surface tension and electrostatic forces cause all the small carbon black particles to form a single, nominally spherical particle by the time the water is evaporated. Thus the particle size at the generator exit should vary with the cube root of the concentration of the carbon solution. Notice here, because of the limitation of the size of the nebulizer, it will be clogged by overly concentrated carbon black solutions. This and the air flow required to properly nebulize the water limits the maximum soot concentration achieved by the soot generator to 4 ppb.

Even though the soot generator flow was designed to produce a laminar jet, the lack of a surrounding coflow makes the jet quite susceptible to disturbances generated in the ambient air, especially somewhat downstream of the jet exit. This limits the useful flowfield length of the soot generator, and most of the measurements with the soot generator were made close to the jet exit.

3.1.2 Laminar Diffusion Flame

A simple, axisymmetric diffusion flame was chosen to develop and test the PVV technique in a reacting environment. The specific burner design has been applied extensively in many soot studies,[62 - 65] and there are numerous experimental results available for calibration of this small combustion environment. The flame is produced above a concentric laminar burner. Ethylene (C_2H_4) was chosen as the fuel because of its high sooting tendency. At the center of the burner is an 11.1 mm i.d. stainless tube (fuel tube), surrounded by a 101.6 mm i.d. concentric honeycombed outer pipe (air tube). Matching the parameters from previous research, the flowrate for fuel and air, respectively, were 3.85 cm^3/s and 713.3 cm^3/s, as measured by calibrated rotameters.

For this flame at the position just above the fuel tube (Figure 3-2), the soot particle formation is in an early stage: the inception rate is high, the primary soot particle size is small and the soot concentration is low. Above that position, the soot inception rate decreases, the primary soot particle size grows, and the soot concentration increases along the flame height. At 40 mm above the exit of the fuel tube (denoted height above burner, HAB) along the flamefront, both the primary soot particle size and soot concentration reach their peak values (34 nm and nearly 10 ppm). Above that height, the primary soot particle size and the soot concentration decay because the soot oxidation

rate exceeds the soot production rate. The heat release rate and flow velocity also vary with height. LDV results are available for a number of conditions.[66] Thus, this flame supplies a valuable source for comparison of velocity data in PVV development, as well as a calibration standard for LII soot concentration measurement.

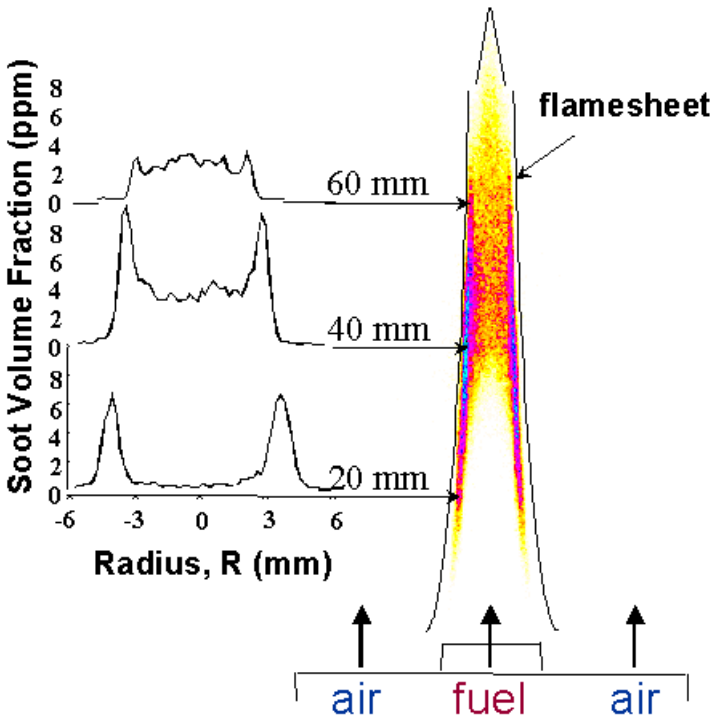

Figure 3-2. Schematic of and soot field produced in laminar, ethylene diffusion flame; LII image[68](right) and soot volume fraction profiles at various heights.[68]

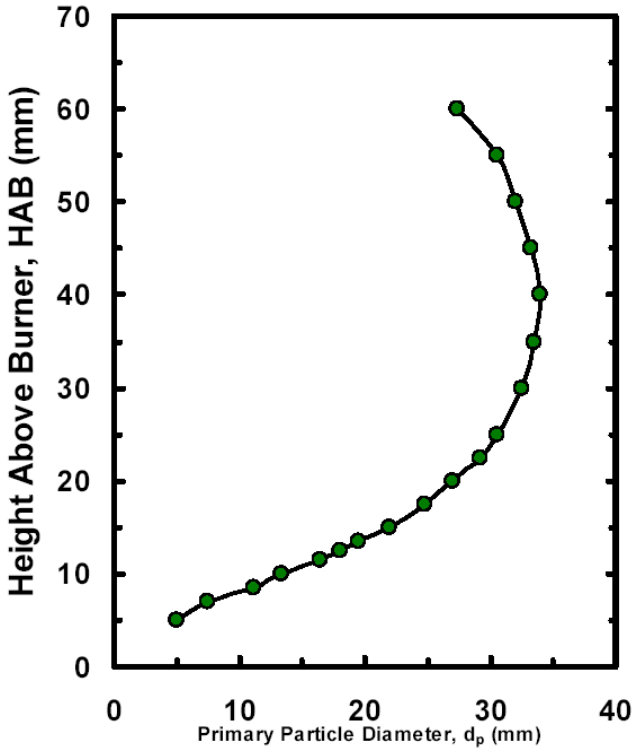

Figure 3-3. Primary soot sizes at different height above burner (HAB) for the laminar diffusion ethylene flame in Figure 3-2.[67]

3.1.3 Acoustically Excited Burner

An unsteady, controllable flowfield can be produced by acoustic excitation of an enclosed burner. The burner employed here (Figure 3-4) consists of a vertical, square steel resonance tube, with a 14×14 cm^2 cross-section and 140 cm length. Its top end is open and the bottom end is nearly a closed boundary. As an open/closed tube, the chamber's first resonance occurs at a 5/4 wavelength, which is ~320 Hz for this system (at room temperature). The tube has 8 quartz windows, consisting of two groups of four, each group at a different height. Each window is 15 cm tall and 5 cm wide. The bottom edges of the lower group windows are 34 cm above the bottom plate of the burner; the upper group of windows has bottom edges 58 cm above the bottom plate. In each window group, two windows are used for the passage of laser beams. The other windows are for

imaging the flame. The complete system's height can be adjusted by a large threaded rod assembly. In additional, an exhaust pipe is mounted at least 40 cm high above the combustor to capture the flame exhaust efficiently without disturbing the burner flow field. The fuel flow exits from a 1 mm i.d. stainless steel fuel tube, which is located in the center of the resonance chamber. The height of the fuel tube can be adjusted such that the flame can be viewed through the imaging windows.

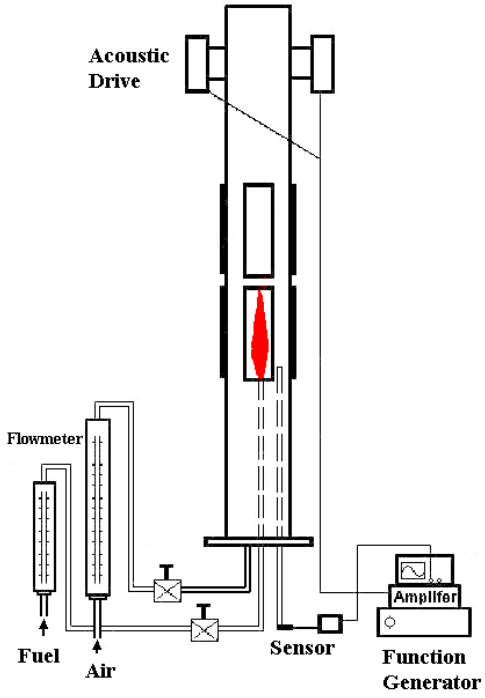

Figure 3-4. Acoustic burner schematic, with flow monitoring and acoustic forcing system.

On the bottom plate, there are four evenly distributed holes with 15 mm i.d., and each of them is connected to a 15mm o.d. copper tube. These form the air supply. Small white stone beads (roughly 3 mm diameter and 4 mm long) are filled to a height of approximately 50 mm at the bottom of the resonance chamber to smooth the airflow field. A screen with a grid size much smaller than that of the beads is placed on the bottom

plate of the chamber to prevent the beads falling into the air tubes. All fuel and air flowrates are monitored by calibrated flowmeters and pressure gauges.

The acoustic forcing signal is created with a function generator (BK Precision, 4010), and its frequency is monitored by a digital counter (Fluke 1900A Multi-Count). Then, the forcing signal is fed to a 100 W amplifier (Radio Shack, MPA101), whose output is connected to two acoustic drivers (University Sound speaker, 10-75-8), which are mounted on opposite sides the top of the resonance tube. In additional, a TTL output from the signal generator is sent to a pulse generator (Stanford DG 535), which is applied to synchronize the laser pulse and ICCD camera to the acoustic driving. A quartz pressure transducer (Kistler Instrument Corp. Model 21185) is placed on one end of a small stainless steel tube, with another end inside the resonance chamber. By changing the location of the pressure tube inside the resonance chamber, the local acoustic pressure can be measured. In additional, the measurement of this pressure transducer was calibrated by placing another pressure sensor inside the chamber, next to exit of the pressure tube.

While applying the acoustic driving force, the flowfield inside the chamber oscillates. The combustion chamber has a high length to diameter ratio, which should result in a nearly one-dimensional, standing-wave acoustic field. Figure 3-5 shows the measured and calculated pressure along the height inside the resonance chamber at room temperature, this plot demonstrates the variation of measured acoustic pressures is very close to the calculated results, i.e. sinusoid wave, except near pressure node. Due to the limited length of the pressure tube, only a partial pressure distribution was obtained. Notice that the measured pressure curve does not form a whole sinusoidal wave at the

bottom of the chamber, this is due to, there are beads on the bottom plate of the chamber instead of a simple closed plate.

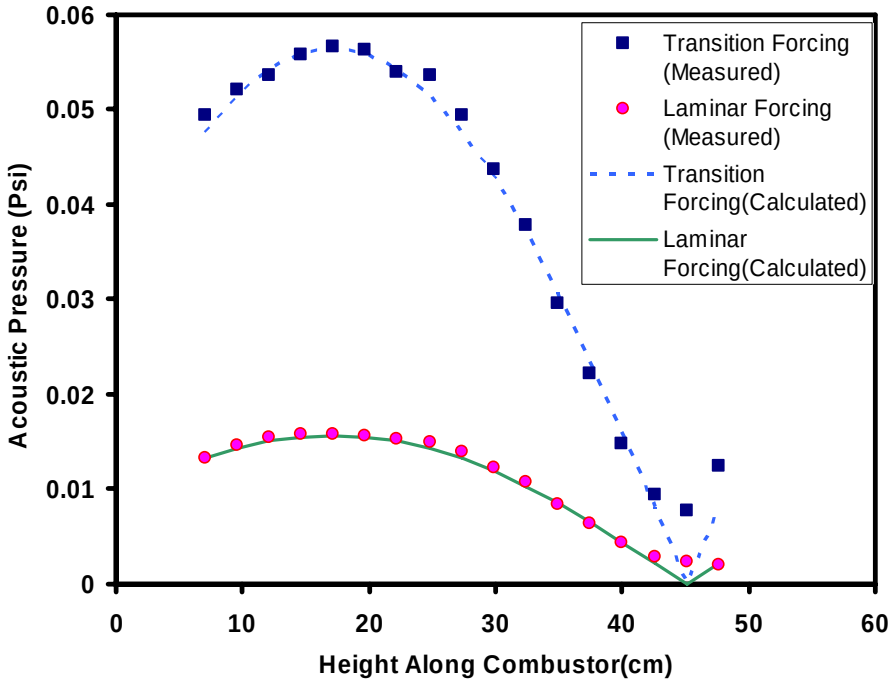

Figure 3-5. Acoustic pressure variation within the burner versus height (a) acoustic pressure variation for laminar flame (b) acoustic pressure variation for transitional flame. During experiments, pressure measurement was fixed at 40cm height.

During the experiments, the flame bottom was located at ~42 cm high in the chamber, and it passed through the pressure minimum (nominally zero at 45 cm), where the acoustic velocity reached its maximum (anti-node). This configuration allowed the highest efficiency of the acoustic driving force, i.e., it consumed the least input driving power to achieve high acoustic pressure/velocity fluctuations.

Based on acoustic theory, there is a 90° phase shift between acoustic pressure and acoustic velocity, and the maximum acoustic velocity (u_{max}) and maximum acoustic pressure (p_{max}) are related by:

(Eq.3-1) $$u_{max} = p_{max} / (\rho * c)$$

where ρ and c are the gas density and speed of sound.

Theoretically, a standing acoustic wave can be generated inside a tube with one end closed, as shown in Figure 3-6. Figure 3-7 shows the pressure variation for a certain location (+), which is close to the pressure node P_{node1} (the first pressure node and velocity anti-node).

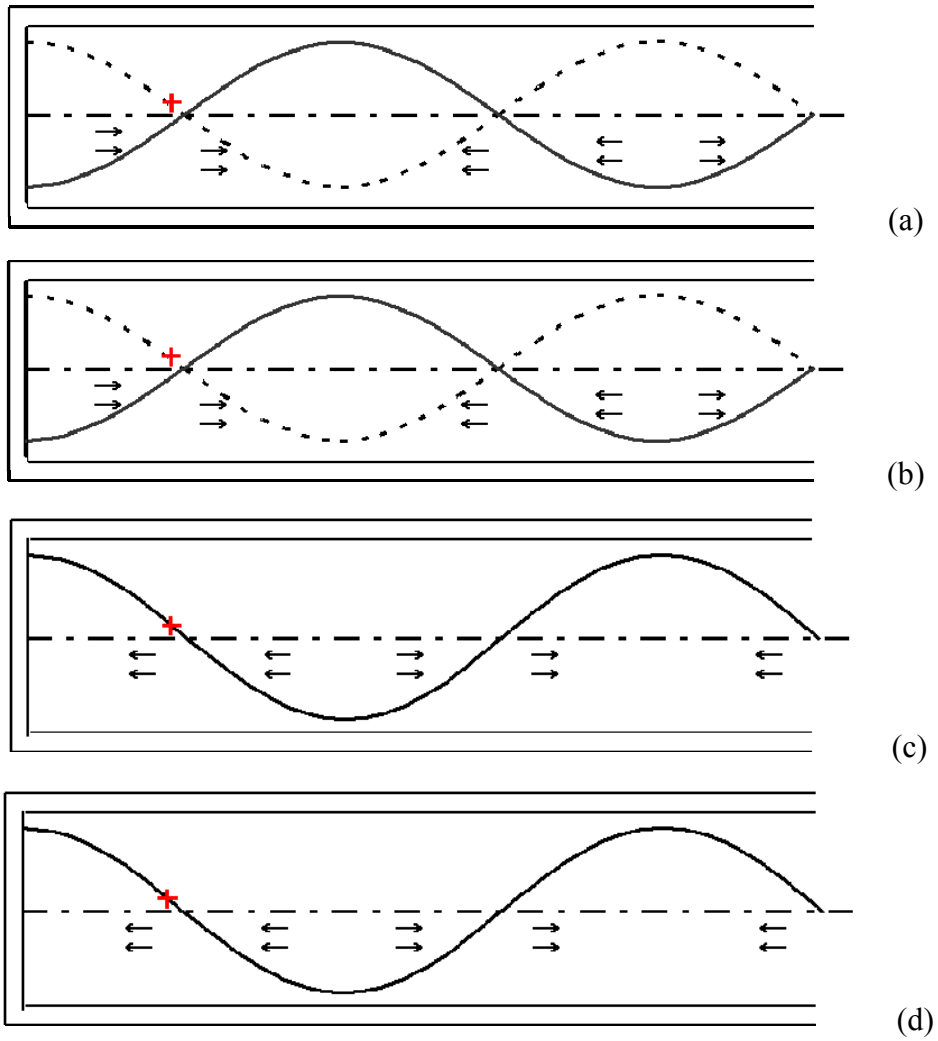

Figure 3-6. Flow pressure distribution and local velocity direction inside 5/4 wavelength acoustic burner (a) from 0^o to 90^o, dotted line is pressure from 90^o to 270^o (b)from 90^o to 180^o (c) from 180^o to 270^o (d) from 270^o to 360^o.

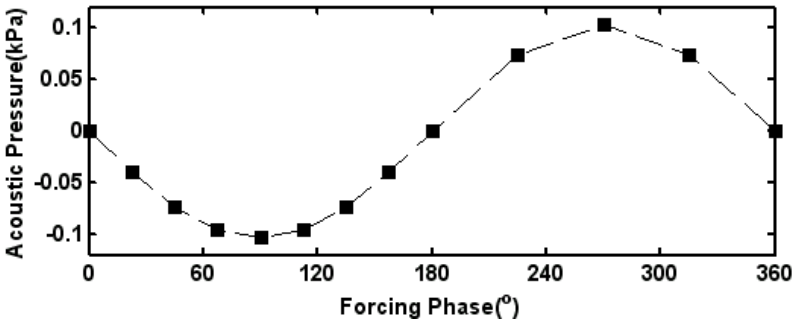

Figure 3-7. Measured pressure variation with acoustic phase at position marked in Figure 3-6.

At the marked (+) location in Figure 3-6, at a phase angle of 0^o, the local acoustic pressure is zero and the local velocity is at its maximum value, moving from left to right, with increasing phase, the acoustic pressure and velocity decrease; until 90^o, the local pressure decreases to its minimum. From 90° to 180°, the acoustic pressure increases with the same direction as main flow pressure, at meant time, local acoustic velocity decrease to its minimum (negative) and turns its direction at 180°, while acoustic pressure keeps increasing; Until 270^o acoustic pressure reaches its maximum (so does local pressure). Local acoustic velocity is accelerated by the pressure gradient and increases at 180°-270° period, until reaches maximum at 360^o, and turns its direction again. The acoustic pressure behaviors is different from velocity, it decreases from maximum to 0 at 270^o to 360^o period, then the cycle repeats

3.2 LASER SYSTEM

A dual head, high power Nd:YAG laser was used for the PVV and LII measurements. Both heads of this laser system (Continuum 45 Surelite I-10) have the same nominal properties: 10 Hz repetition rate, maximum pulse energies of 450 mJ and 200 mJ for the infrared (IR, 1064 nm) and green (532 nm) wavelengths, respectively; an IR pulse width of 8 ns FWHM (Full Width Half Maximum); 8 mm beam diameter

(measured by a burn mark method and Rayleigh scattering). The pulse-to-pulse repeatability of the energy is better than ± 5% for both lasers.

The spatial distribution of the laser energy is measured by the edge-cutting method.[68] The beam is blocked partially by a sharp blade, and the transmitted energy is measured with a power meter. By translating the blade, the blocked area is varied and the energy profile is acquired. Based on this application, the FWHM for IR and green laser beams are 3.0 mm and 2.45 mm, respectively. The energy is measured in a time-averaged manner, by a pyroelectric joulemeter (energy/shot = average power/frequency).

The laser energy can be varied three ways: by varying the Q-switch delay (relative to the flashlamp charging cycle), changing the laser flashlamp power (charging voltage) setup, or, employing a variable polarization beam splitter. A reduction in energy down to ~50mJ (IR) can be achieved by increasing the Q-switch delay or varying the flashlamp discharge voltage. For such variations, the beam size changes only slightly, however the laser beam profile can also change. So, a more reliable procedure is to use a polarizing beam splitter and a half-wave plate, with the beam splitter preceded by the half-wave plate. By rotating the half wave plate, with the prism remaining fixed, the fraction of transmitted and reflected energies is varied. The desired laser energy can be decreased to as low as 9 mJ, without changing laser beam size and profile. Furthermore, if fine spatial resolution is required, cylindrical lenses with short focal length can be applied to spread the laser beam horizontally or vertically (depends on experimental requirement), and this can decrease the laser intensity greatly.

The higher power and improved coherence of the YAG laser were estimated to be more than sufficient to attain fluence values well above threshold, even for a significantly

expanded beam. The improved focus of the YAG laser also increases the spatial resolution of the measurements. The YAG laser also provides a more Gaussian spatial profile and a more temporally stable (shot-to-shot repeatable) output intensity. The fast decay of the nanosecond scale laser supplies the relative long life LII signal, upon to 1μs. The YAG laser output is in the infrared (IR) at 1064 nm, but can easily be frequency-doubled into the visible region i.e. green (532 nm) laser. Employing the infrared pulse of the Nd:YAG may be preferable for the total rejection of elastic scattering; in additional, the longer waver length (compare to second harmonic, i.e. 532nm) of IR are less sensitive to particle size, thereby it supposes better accuracy of LII measurement; while the green laser (532nm) can be applied for both scattering and LII measurement.

When a Gaussian profiled laser beam is incident on a soot field, there is a decrease in LII signal from the high intensity center of beam (due to vaporization) as the laser energy is increased. This is compensated, however, by the increase in LII signal from the lower power edge of the laser beam. This balance results in an overall LII signal that initially rises with increasing laser fluence, but then plateaus at some laser fluence. This phenomenon is called the LII "threshold" effect. Of course, the threshold intensities for infrared and green lasers wavelengths are different, because the absorption rate of soot particles is different at the two wavelengths.

Figure 3-8 shows the plot of previous experimental results[68] for the threshold effect in our laboratory with the 1064 nm beam. The LII signal is very small at very low laser energy, with the increasing of laser intensity, the LII signal increases very fast (0.1~ 0.5 J/cm^2); after that laser intensity region, LII signal is almost remain flat with the

increasing of laser energy. Therefore, it is can be seen the threshold laser fluence this IR laser is 0.5-0.6 J/cm.

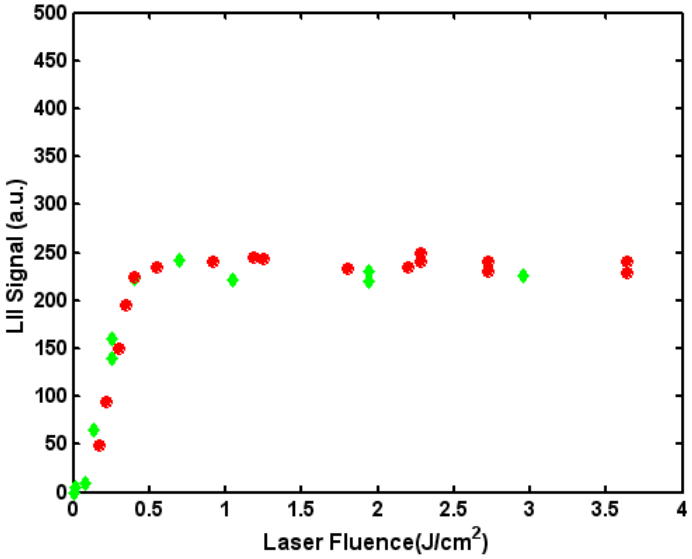

Figure 3-8.Variation of LII signal with laser fluence for measurements acquired in a laminar, ethylene-air laminar diffusion flame, laser excitation from a Nd:YAG pulse.

Most soot concentration results reported here are for average energy fluence somewhat above the LII threshold, or greater than 0.1 J/cm^2. The same is true for the imaging laser sheet in PVV measurements. The laser intensity is well above the threshold for the marking beam in the PVV measurements, in order to achieve good contrast of the marking area. The repeatability of pulse-to-pulse laser energy and temporal profile were generally good, with a worse case variation of ± 7%.

3.3 ICCD CAMERA SYSTEMS

Two Princeton Instruments intensified, CCD (ICCD) cameras were employed in this research work. One is a 12 bit, 576×384 pixel device (model 576-S/RR-E); the other is a 16 bit PI-MAX (512×512 pixels) system. In addition to the camera, the first system includes a detector controller and a PG-200 pulse generator. The second system includes

an integrated controller with pulse-timing-generator (PTG) and signal acquisition board. The function of the PTG board is similar to the PG-200; they control the gate time and gate width of the ICCD camera. A standard 35 mm Nikon camera lens is mounted for imaging purpose.

For low-light-level imaging, the ICCD cameras depend on a Microchannel Plate (MCP) device to amplify the incident photons. The MCP has thousands of independent channels, and each channel works as independent electron multiplier. An MCP consists of a two-dimensional periodic array of very-small diameter glass channels fused together and sliced in a thin plate. A single incident photon strikes a photocathode located in front of the MCP and causes an electron to be emitted from the channel wall. These electrons can be accelerated by an electric field developed by a voltage applied between both ends of the MCP. They travel along their parabolic trajectories until they strike the channel surface, producing secondary electrons. This process can be repeated many times before the numerous electrons finally reach the back of the MCP and strike a phosphor plate located behind the MCP. The combined result is a photon output that can be hundreds of thousands of times larger than the number of original input photons.

In an ICCD camera, the phosphor at the back end of the MCP is imaged onto a CCD camera. Typically, a number of MCP microchannels are imaged onto each CCD pixel. A CCD is made of p-type and n-type silicon semiconductor material; it coverts photons to an electronic signal based on the photoelectric principle. A small voltage is applied across the CCD to form a potential well. When a photon with certain energy strikes the CCD surface, a electron-hole pair is produced. The hole can be diffused and absorbed by the p-type substrate, while the electron moves towards the potential well and

accumulates there. Electrons are stored inside the well throughout the period of exposure time, in a (quite nearly) linear proportion to the total amount of photons received. Each CCD lattice is also called a pixel; a CCD chips generally consist of millions of CCD pixels that are grouped as an array structure, or “waffle” pattern in a silicon chip.

In order to generate an image, the electron charge accumulated in each CCD needs to be measured and read out in certain sequence. A Charge Transfer Device (CTD) is coupled with a CCD; it shifts the charge stored in the corresponding CCD and passes it to a charge-to-voltage converter, where the output voltage generated is proportion to the charge. Each CTD works individually without interference between the other charged packets. A serial register circuit is built inside CCD chips to locate each pixel location in the CCD array. Finally, the charge packets are transferred from the detector in a pixel-by-pixel, row-by-row sequence, the whole array represents the image falling on the CCD.

It should be noted that excess input light levels can damage the intensifier of ICCD. Thus, the best data collection should be below the saturation point of the CCD chips. To prevent the incoming light from overloading the intensifier, one can either decrease the f-stop size of the camera lenses, decrease the gain of ICCD, or place filters (e.g., Neutral Density (ND) filters) proceeding the camera lens.

3.4 OPTICAL AND SYNCHRONIZATION SYSTEMS

Two main setups systems are documented below, one for PVV and the other for LII soot concentration and flame radiation measurements. Furthermore, two PVV setups are detailed: a 1-d velocity measurement system and a 2-d velocity setup.

3.4.1 PVV: One-Dimensional

The optical scheme for the initial PVV experiments is shown in Figure 3-9. The marking (first) beam comes from the IR laser, and the readout or image (second) laser pulse is from green output of the second head. Both beams are converted into laser sheets, which are aligned normal to one another in the flow. The two laser beams propagate at a small relative angle, crossing near the center of the imaged region. The 8 mm IR beam is focused by a 250 mm focal length cylindrical lens (L1) to a horizontal laser sheet. The focus of the 8 mm wide sheet is typically located past the flow, such that the sheet thickness decreases slightly from the point where it first encounters the flow. The nominal thickness (FWHM) in the laminar diffusion flame measurements is 0.45 mm, and changes to 0.6 mm for the nonreacting (soot generator) flow. In addition, the sheet width can be reduced from 8 mm to 2 mm using a metallic aperture placed behind the focusing lens (see Figure 3-9). The thin dimension (thickness) of the sheet is parallel to the primary flow direction. The marking laser energy is varied with a half-wave plate and polarizing beam splitter.

The image (readout) beam is focused by a 500 mm focal length, cylindrical lens in the vertical direction and spread in the horizontal direction by a 25 mm cylindrical lens. This yields an imaging sheet that is ~0.4 mm thick and 100 mm high. The fluence of the imaging beam is fixed for all measurements at ~0.4 J/cm^2, which is sufficient to allow either LII or scattering measurements of the nonvaporized particles. The LII and elastic scattering images are recorded at roughly 45° to the propagation direction of the visible laser sheet (rather than the preferred 90° due to limited optical access) by the ICCD camera equipped with a standard 35mm camera lens.

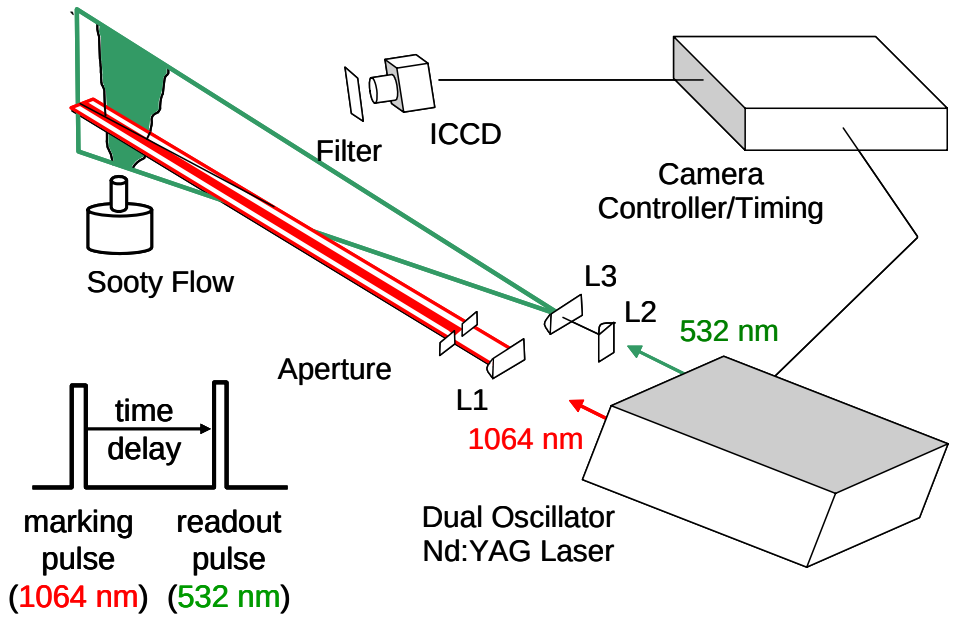

Figure 3-9. Optical set up for PVV measurement. L1: cylindrical lens with focal length 500mm. L2: cylindrical lens with focal length 250mm, L3: cylindrical lens with focal length 50mm.

For the soot generator, with its low particle concentrations, the lens f-number is set to its minimum value for the LII measurements (f/2.8), but degraded for the brighter scattering measurements. In the flame, with its higher levels of soot, the lens aperture is increased to f/32 for both interrogation methods. In some cases, neutral density filters or a 532 nm holographic notch filter are placed in front of the lens to prevent intensifier saturation. The neutral density filters can reduce the input light intensity almost evenly throughout the entire visible wavelength. The 532nm notch filter can only totally reject the 532 nm light (5nm FWHM), without effecting light at other wavelengths. The intensifier gate duration is 50 ns.

For the scattering data, the intensifier gate begins just after the onset of the interrogation laser pulse for the LII measurements; the bright elastic scattering signal can be rejected either by placing a 532 nm holographic notch filter in front of the lens or delaying the intensifier gate by 32 ns. Since the total duration of the laser pulse is about

25 ns, the delayed gating rejects the prompt scattering signal, but is sufficient to detect the long lived LII.

The velocity measurement in PVV is based on the calculation of the measured displacement of the marking area for a "known" delay time. Determination of the delay is based on the system synchronization. That is to say, each individual apparatus in the detection system runs at some fixed time relative to the other instruments. Examples include the timing of each laser firing and the time when the camera's intensifier is gated on. Correct timing between each instrument is necessary to obtain accurate PVV measurements.

Synchronization of the detection system requires both laser heads (marking laser and imaging laser) and the camera to be synchronized. To this end, two digital and delay pulse generators (both Stanford SRS DG535) were utilized. The T_O output of the first pulse generator is input to the external trigger of the second pulse generator, this synchronizes the two signal generators. The first pulse generator triggers the IR(marking) laser head; channel A and B together supply the negative TTL signal with 10 microsecond width for firing the flashlamp; while channel C and D together supply another 10 microsecond width negative TTL signal for the Q-switch control. A similar approach was employed for using the second pulse generator to control the imaging laser. Channel C of second pulse generator also supplied a TTL signal to synchronize the pulse generator (PG-200) of the ICCD system. Also, the PG-200 gate delay is adjusted to that the camera captures the image produced by the second laser. So, once the system is properly timed, the delay between the marking laser pulse and the image laser/camera is easily set by adjusting the delay between the two pulse generators. The setting required to

produce no delay is determined by observing the output of both lasers on a photodiode connected to an oscilloscope.

3.4.2 PVV: Two-Dimensional

In flows with more complicated velocity fields, such as that expected in the acoustic burner, the one dimensional PVV technique is not appropriate for velocity measurements. A more involved, 2-dimensional velocity measurement technique can be achieved by applying a cross-beam method, i.e., the marking line is replaced by intersecting laser beams. Then the calculation of displacement is based on the movement of the intersection points of the beams instead of the displacement of the marking line. The details of this modified setup are now described.

Similar to the one-dimensional PVV approach, the fundamental (1064 nm) output of one laser head is used as the marking beam. However, the 8 mm diameter beam is now separated into four beams. Figure 3-10 shows the combination of 50/50 beam splitters (CVI BS1-1064-50-1025-45UNP**)** and mirrors (CVI Y1-1025-0-1064nm). The final result is four similar beams, each ~110 mJ/pulse. The optics are arranged such that the four beams travel inside a single plane and form a "grid" after being focused by a 50×60mm, 150 mm focal length cylindrical lens. Each marking beam thus forms a small sheet, each 8 mm wide and 0.5 mm (FWHM) thick. These sheets mark a thin region that extends across a wide path normal to the flow. The average energy fluences of the marking sheets are 2 J/cm^2 each; more than 3 times the IR vaporization threshold (~0.6 J/cm^2).

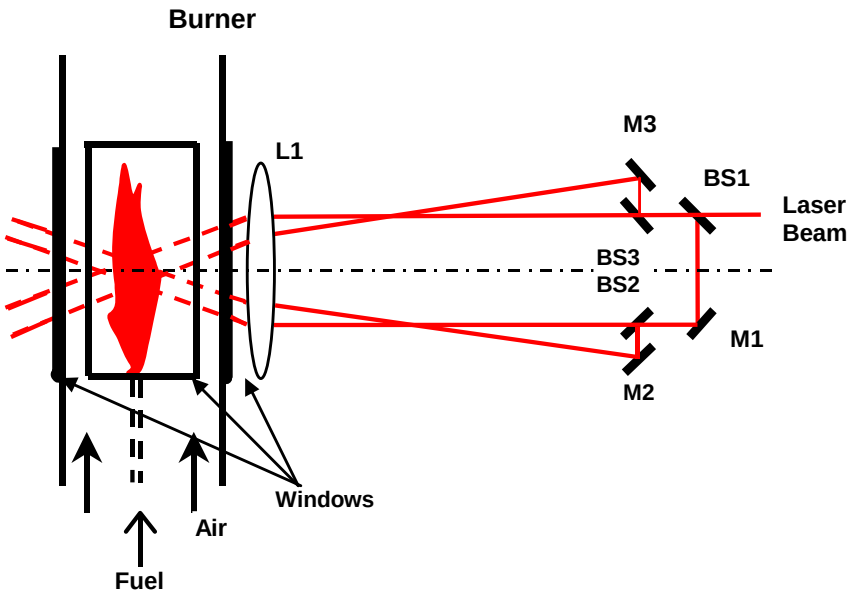

Figure 3-10. PVV optical setup(marking beam): L1 f=150mm cylindrical lens; mirrors M1, M2, M3; e 50/50 beam splitters BS1, BS2 BS3.

The visible readout (imaging) beam arrangement is similar to the one-dimensional PVV case. It is produced by frequency-doubled (532 nm) output of the second Nd:YAG laser head. The image beam is focused by a 90 mm diameter, 500 mm focal length fused-silica cylindrical lens in the vertical direction and is spread in the horizontal direction by another cylindrical lens with 25 mm focal length. This yields an imaging sheet that is 0.8 mm thick and 75 mm high. The fluence of the imaging beam is fixed (~0.1 J/cm^2) and just below the vaporization threshold intensity. Thus, it can be used for LII measurements of the soot.

The readout sheet is carefully position to coincide with the plane defined by the four intersection points of the marking beams. The readout sheet is also carefully aligned to be normal to each of the marking sheets. The image is recorded at a right angle to the laser beam by the ICCD camera. In most experiments, the ICCD camera gate starts with the onset of the green laser, and has a 50 ns width.

For the two-dimensional velocity measurements inside the acoustic burner, the acoustic driving signal (sinusoidal waveform) must also be synchronized to the laser as well as imaging system. For this purpose, the timing arrangement used in the 1-d PVV measurements was modified. The first pulse generator was triggered by the TTL output of the function generator (whose sine wave output drives the acoustic forcing). However, the lasers are limited to 10 Hz operation and can not "keep up" with the acoustic forcing frequencies. To lower the triggering frequency to the lasers' rate, the T_o delay of the first pulse generator was set to just over 99 milliseconds. During this time, the pulse generator is idle. The next TTL trigger from the function generator then fires the pulse generator. Since no more triggers come from the frequency generator in the next 1 ms, the lasers and camera system are driven at ~10Hz, but phase locked to the acoustic drivers. The exact phase of the measurement is adjusted by changing the delay of the first pulse generator.

3.4.3 LII Soot Measurement and Soot Radiation

Soot concentration measurements are also acquired in the acoustic burner with the LII technique. The IR YAG beam is focused by a 500 mm focal length, cylindrical lens in the horizontal direction and spread vertically by a 250 mm focal length cylindrical lens. This yields a laser sheet that is ~0.8 mm in thickness and 45 mm in height, with the thickness parallel to the flow direction. The fluence of the imaging beam is fixed for all measurements at ~0.75 J/cm^2, which is sufficient to produce quantitative LII signals of soot generated by the flame. All images are recorded at roughly 90° to the propagation direction of the IR laser sheet by the ICCD camera (Figure 3-11). The LII signals are recorded with a 50 ns intensifier gate width, camera lens aperture of f/32, and a 0.5 ND

filter placed in front of the lens because of the strong LII signal of the flame. The LII laser and camera are synchronized to the acoustic driving as described in the 2-d PVV section.

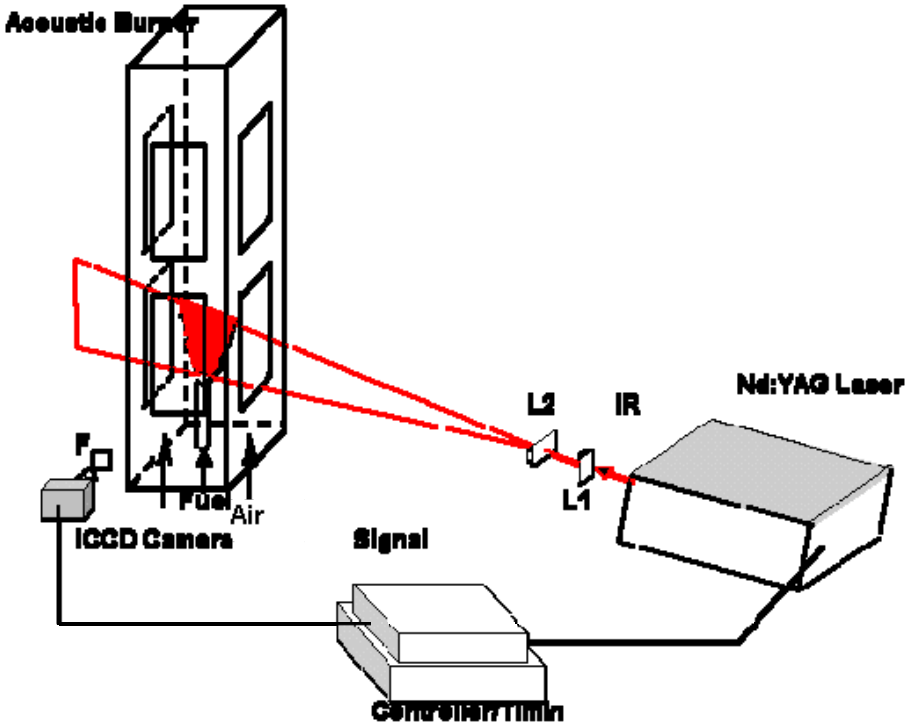

Figure 3-11. LII soot measurement system: acoustically burner, signal generator, laser system and ICCD camera.

To image the natural radiation of the flame soot, broadband, as well as 430 nm and 650 nm narrow band, detection arrangements were employed. For broadband radiation measurements, the ICCD gate width is 500 ns, the lens aperture setting is f/32, and no filtering is applied. The 430 nm radiation measurement is achieved by putting a 50×50 mm, 2 mm thick bandpass filter (CVI) in front of the ICCD camera. This filter is centered at 430 nm, with a 10 nm FWHM, and a peak transmissivity of ~50%. Similarly, the 650 nm wavelength radiation is acquired by using a 50×50 mm, 3 mm thick bandpass filter (CVI), which is centered at 650 nm, with a 10 nm FWHM and a peak transmissivity around 77%. In both 430 nm and 650 nm measurements, the lens aperture is f/32, and the

intensifier gate duration is increased to 5 μsec to compensate for the weaker narrow band signal. While no laser synchronization is required, the ICCD camera can be phase-locked to the acoustic driving as described previously.

3.5 CALIBRATION OF SOOT CONCENTRATION MEASUREMENT

For quantitatively measuring soot concentrations in the flame, a system calibration process is required. This calibration is based on the well-characterized ethylene laminar flame. The detailed process of calibration is described below.

3.5.1. Calibration of LII Signal and Soot Concentration

To calibrate the measured acetylene flame soot concentration, it is assumed that the soot particles for both ethylene and acetylene laminar flames have similar optical properties, such as refractive index. In addition, similar laser intensities and identical setups were applied in both flames for the LII measurement. The measured average peak LII signal at 40 mm HAB is 16000 counts from the 16 bit ICCD, while the camera dark background ~220 counts. From previous work,[69] it is known that the soot concentration at 40 mm HAB with ethylene is ~10ppm. Under the assumption that the acetylene flame soot particles are very similar to those of ethylene flame, the raw image LII data can be converted to soot concentration data. The LII-soot concentration conversion equation can be stated as:

(Eq.3-2) $$m_{soot} = C_m * (S_{LII} - S_{bak})$$

where C_m is the calibration coefficient, and its value is 9.5×10^{-4} ppm/count for the 16 bit ICCD camera, and 1.6×10^{-2} ppm/counts for 12 bit camera.

3.5.2. Cross Calibration between the 12 Bit and 16 Bit ICCD Cameras

Only the 16-bit camera was calibrated in the ethylene flame. The 12 bit ICCD was cross calibrated with the 16 bit device (since the former one was not available at the time of calibration) by acquiring LII images of the same laminar flame with the same optical setup. The cross calibration was computed by comparing the averaged peak (in space) intensity data for the two different cameras. This method was chosen because the peak soot value for the laminar flame was relative stable after time averaging, while the spatially averaged signal may vary very much due to signal in the large background area. In the above measurements after dark background correction, the 12 bit camera peak LII signal was 2622 counts, while the 16 bit camera signal was 45168 counts, and the standard deviations were 255 and 8718, respectively. Since these two different LII signal levels should represent the same soot concentration level, the cross calibration coefficient between these two cameras is 45168/2622=17.2.

Overall, the cross calibrate coefficient is depended on the optical system setup, such as camera focus length, aperture size number, etc, it need to be re-calibrated whenever the optical system is modified.

3.6 UNCERTAINTY

The uncertainties and errors for PVV and soot concentration measurements are generated from detection and data reducing processes

3.6.1 Laser System uncertain

A double head Nd:YAG Laser system was applied in all experiments. This system shot to shot uncertain was tested as 5%.[68]

3.6.2 PVV measurement uncertainties

Particle Vaporization Velocimetry (PVV) is based on tracking the pixels with lowest LII signals. To find the displacement of these pixels, their initial and final locations have to be read out from first and delayed images. Since the minimum unit on the experiment images is one pixel, thus the uncertainty of these and the error is generated when locating the sub-pixel evaluation, maximum half pixel. Besides, unsteady effect could cause the local lowest soot pixel move away from the original direction. This side effect is negligible in laminar flame measurement, where the radial velocity is very small, and second image was acquired after short delay (~ms). But, in forced flame velocity measurements, the marking region (cross of two marking laser).could be fast refilled by strong unsteady ambient flow, this decreases the accuracy of read out results from second images.

3.6.1 Quantitative soot measurements

In calibration process, it is assumed that the soot index of acetylene soot particle is the same as soot inside ethylene flame.

CHAPTER 4
PARTICLE VAPORIZATION VELOCIMETRY

To measure soot emission rate (soot flux) in sooty flow, velocity measurement is necessary. This chapter presents the development of the Particle Vaporization Velocimetry (PVV) technique, a new laser based velocity measurement approach. First, details of the method are laid out. Then, the technique's characteristics are studied in simple axisymmetric jet flows, both non-reacting and reacting flow. Finally, it is demonstrated in the (more complex) acoustically excited combustor.

4.1. PVV SCHEME

The basis of this technique is relatively straightforward. A high intensity laser beam is applied to a soot laden flowfield. This laser vaporizes the particles within its beam path, thereby creating a relatively low soot concentration region, denoted the *marked region.* This (first) laser pulse is named the *marking beam* and its actual size and position can be adjusted according to the experiment setup. If a second (lower fluence) pulsed laser beam fires sometime after the marking beam, it will generate both Mie scattering and LII of the soot field. Thus, the convective movement of the marked region can be highlighted, as it stands out as a region of lower signal caused by the reduced (vaporized) soot concentrations. Consequently, the second laser beam is donated the *image beam* (or readout beam). Typically, the image beam would be formed into a sheet large than the marking beam. Of course, in order to get accurate experiment results, the two laser pulses and image detection system (gated to overlap the image beam pulse) need to be well synchronized during this process. The timing uncertainty can be as low as

a few nanoseconds (when one external pulse generator controls both Q-switch delay and flashlamp delay of the lasers).

If the marking and image lasers are pulsed simultaneously, the initial location of the marked region can be easily located on the image data. As longer delay times are chosen for the image beam, the new location of the marked region can be ascertained. By comparing the two images (no delay and delayed), the displacement of the marked region can be determined. The ratio of the displacement to the delay time provides the velocity of the flow. Therefore, from a single (instantaneous) image, one can determine the local velocities in the flow field. Alternatively, by taking accumulated images (averaged over a number of laser shots), the average flow velocity can be measured.

Before employing PVV for velocity measurements, it is important to determine which setup of experimental parameters will lead to an optimized PVV measurement, and whether there are any significant limitations for the application of the proposed technique.

4.2. CHARACTERIZATION OF PVV

Primarily, the PVV signal is based on the readout image. Thus, optimization of the image beam leads to the initial step of the PVV development, i.e., determination of the best detection method for the readout image. The two most likely candidates are elastic scattering from the (unvaporized) soot particles and LII. Elastic scattering detection is easily implemented, and generally produces strong, easily detected signals, from particles with the size of soot. It is likely to suffer, however, from background problems associated with scattering from other particles in the room, e.g. dust, and from any surfaces that the laser sheet contacts. Furthermore, multiple scattering also can supply unwanted signal. Detection of the marked region using LII (again from the

surrounding soot) has the advantage that only the appropriate absorbing/emitting particles (e.g. soot) within the line of the laser beam are able to achieve a high enough temperature to produce a signal, and the signal wavelength can be isolated from the laser wavelength. Thus LII detection is likely to have less background problems than elastic scattering. It may, however, have other disadvantages compared to elastic scattering detection. Therefore, the following studies include measurements utilizing both detection approaches, allowing the optimum method to be determined. As an example comparison, Figure 4-1 shows LII and scattering images acquired in the nonreacting, soot generator flow. The marking beam is a horizontal sheet, while the image beam is a vertical sheet aligned with the image plane. The LII image (a) shows little signal outside the soot flow, while the scattering images (b and c) have backgrounds due to scattering from ambient particles.

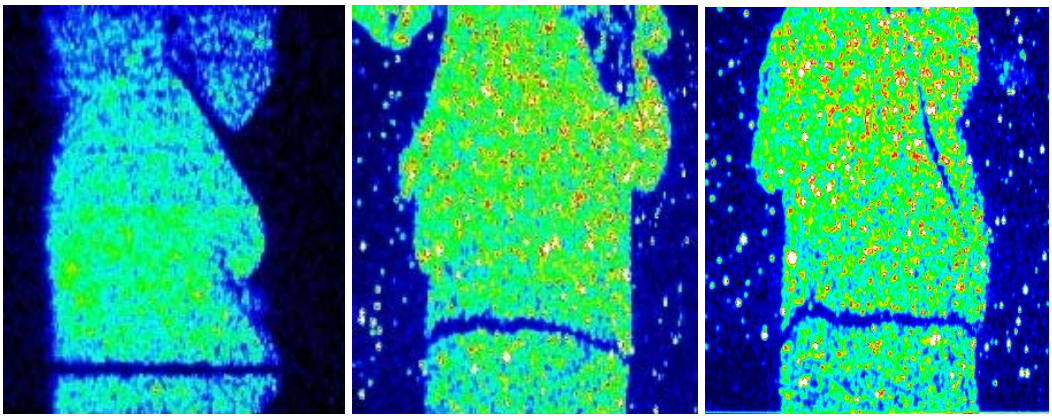

(a) (b) (c)

Figure 4-1. Instantaneous images of the vaporized stripe acquired in the soot generator for different delays after the 2 mm wide marking laser sheet pulse: (a) 1μs delayed LII image; (b and c) 1 ms delayed scattering images . Image sizes are 28×24mm.

In the following sections, results are reported on measurements of various parameters that determine the requirements and limitations of the PVV method. Specifically, these are the required (vaporization) laser energy and the lifetime of the

marked/tagged region. The first will impact the laser requirements to perform PVV, the latter effects the range of velocities that can be detected with PVV. In addition, velocity results in the three different flows are presented and compared to expected values.

4.2.1. Marking Laser Energy

In flow tagging techniques like PVV, the ability to determine the location of the marked region can often limit the accuracy of the measurement. Quantitative measurement of the detectability of the flow tagging is the contrast between the signals from the marked (S_{mark}) and unmarked (S_{unmark}) regions. The contrast can be defined as follows:

(Eq. 4-1) $$Contrast = \frac{S_{unmark} - S_{mark}}{S_{unmark}}$$

with the optimal contrast being unity. With high enough intensity, a laser ought to be able to vaporize the soot particles in its path thoroughly, which would potentially allow unit contrast to be obtained. Total vaporization of soot in the marked region could need a very powerful laser source, which might limit the practicality of PVV. Thus is important to find out the optimum laser intensity that can create a sufficiently high contrast for detection of the marked region.

4.2.2. Delay Time for Initial Contrast Measurement

A short or zero delay between the marking laser and imaging laser was preferred to investigating the optimum marking laser energy, for there are less ambient effects during that period, such as diffusion and convection. Initially, a 100ns delay was chosen to measure the original contrast of the marked region. However, during LII measurements, especially in the laminar flame, an interesting phenomenon was noticed. A high-level signal region close to the marked area appears, as shown in Figure 4-2. Figure 4-3 shows

corresponding LII signal varies along the flame sooty area in Figure 4-2 (with 5 pixels binning horizontally along flame soot formation area (see chapter 3)), after background correction (all flame images in this chapter are background corrected).

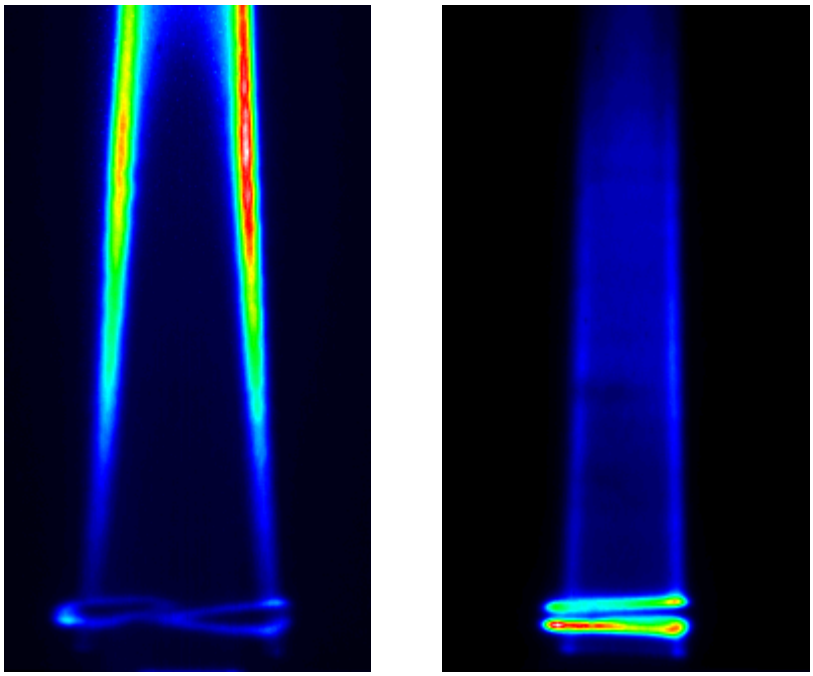

(a) (b)

Figure 4-2. Flame LII signal from green readout laser for 100ns delay (a) 10mm HAB (b) 40mm HAB in the laminar diffusion flame.

Actually, for the high intensity (>2 J/cm^2) Gaussian profile laser beam, such as the IR marking laser beam, due to sharply decreasing of intensity along two side of the laser beam, soot exposed in the very center of laser beam can be vaporized, while the edge of laser beam can only partially vaporize or even simply overheat soot particles. Even though, the soot particles in these areas can still gain strong enough laser energy to produce LII signal. From previous research, it is known that the lifetime of LII signal is around 1μs. If the imaging laser fires within 1μs, the "extra" LII signal from IR pulse will overlap the imaging beam LII signal, and creates a high level signal area thereafter. This suggests the contrast based on highlighted region data does not truly represent the portion

of vaporization of soot mass. Sometimes, it seems this region can highlight the edge of marking area, thus increases the detectability of the marking area (Figure 4-2(b)). But at other flow conditions, it may highlight unexpected signal region (Figure 4-2(a)), and leads to incorrect results. This negative affect might be potential drawback for the LII detection. For example, in unsteady flow, it could be hard to discriminate the real marked area in the region of detection. However, this problem can be solved by simply extending the delay time of imaging laser over the marking laser LII signal lifetime, 1μs.

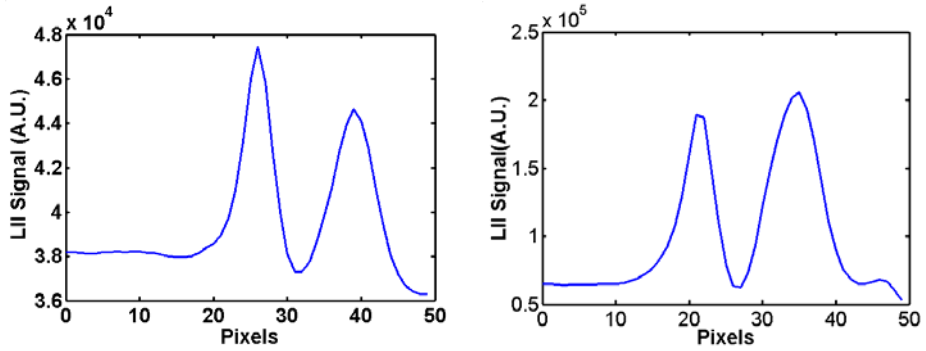

(a) (b)

Figure 4-3. LII signal at 50 pixels height around the marking region, with 5 pixels binning horizontally. (a) 10mm HAB, (b) 40mm HAB.

In the soot generator measurement, above problem is minor, the reasons are listed below: First, the flame soot concentration is not uniform; the flame has higher soot concentration around its edges and less soot in the jet center. The marking laser has a sheet size of 8 mm, which is comparable to the flame diameter (10 mm). Thus, the edge of IR laser can heat the high soot concentration (~ppm) region at the flame edge and produce higher level LII signals. The larger soot generator jet size (18 mm diameter.) is bigger than the 8 mm marking laser sheet, and the jet has a nominally uniform soot concentration (~ppb) crosswise. Second, the soot generator particle size is much bigger (>400 nm on average) than that in the flame (~30 nm). As presented in Chapter 2, the

small flame soot particles have much higher laser energy absorption rate (volumetric absorption) than big particles of soot generator. If same mass of soot are exposed to the same laser beam, the smaller particles will have higher heating temperature and correspondingly greater detectable LII signal. Thus, even at short delay time, ~100ns, low soot concentration and big size particles from soot generator produce much less detectable LII signal from marking beam, which may interference with the imaging beam LII signal.

In addition, all the flowfield tested in the current work have velocities below 50 m/s; in 1μs, the displacement of a moving particle inside these flows would be less than 50 μm, which is beyond the imaging resolution of our ICCD (at best magnification of our lens, the minimum measurement region is ~81 μm/pixel). Therefore, the 1μs delay of second laser beam (readout beam) is chosen to investigate the original marking region and to represent the original marking region in all the experimental results reported below.

4.2.3. Marking Laser Energy

The marking "stripe" in the instantaneous images shown in Figure 4-1 was obtained with a laser fluence of ~6-8 J/cm^2. This intensity is very high and more than 10 times the LII threshold for the IR laser. Lower fluences are also sufficient to produce a soot "hole". For example, Figure 4-4 and Figure 4-5 show averaged LII and instantaneous scattering images for the marked region in the soot generator flow produced by different laser fluences: 0.84, 1.0 and 4.7 J/cm^2. The soot generator was operated at its highest concentration, 4 ppb. **Error! Reference source not found.** show the marked region in LII images for the laminar diffusion flame at 40 mm HAB for a similar range of laser

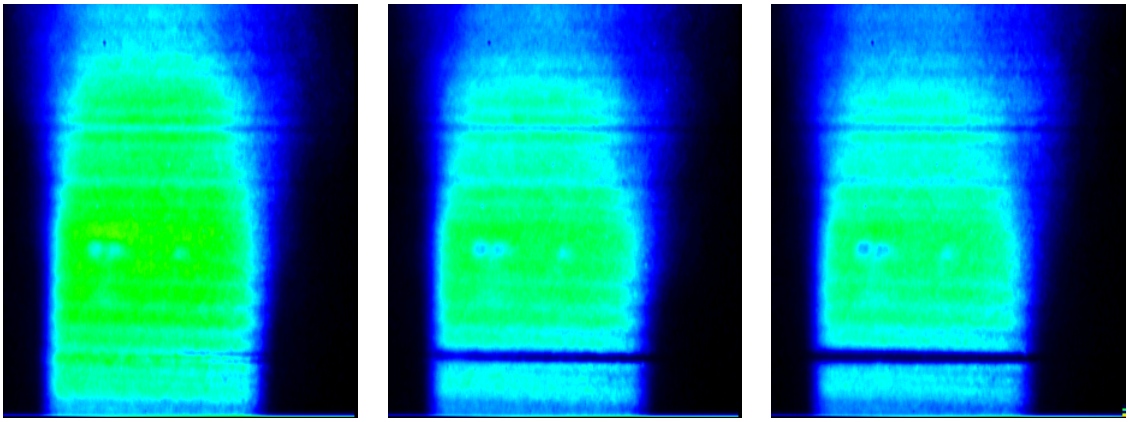

a) b) c)

Figure 4-4. 4 ppb soot generator data: 100 shot averaged LII images at 1 μs delay and for three laser fluences: a) 0.84 , b) 1.4 and c) 4.7 J/cm^2. The marking laser sheet is 2 mm wide, and image size 28×24mm.

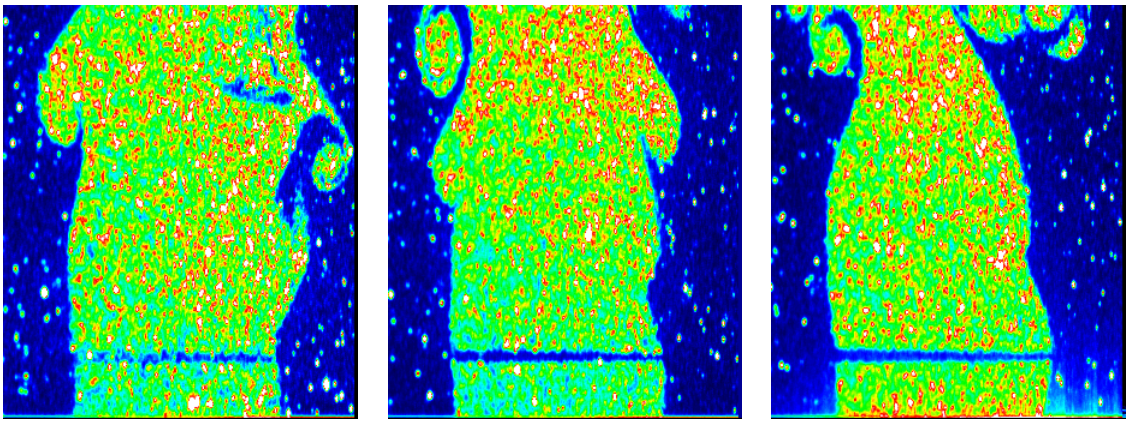

a) b) c)

Figure 4-5. 4 ppb soot generator data: instantaneous scattering images for the same conditions listed in Figure 4-4: a) 0.84, b) 1.4 and c) 4.7 J/cm^2.

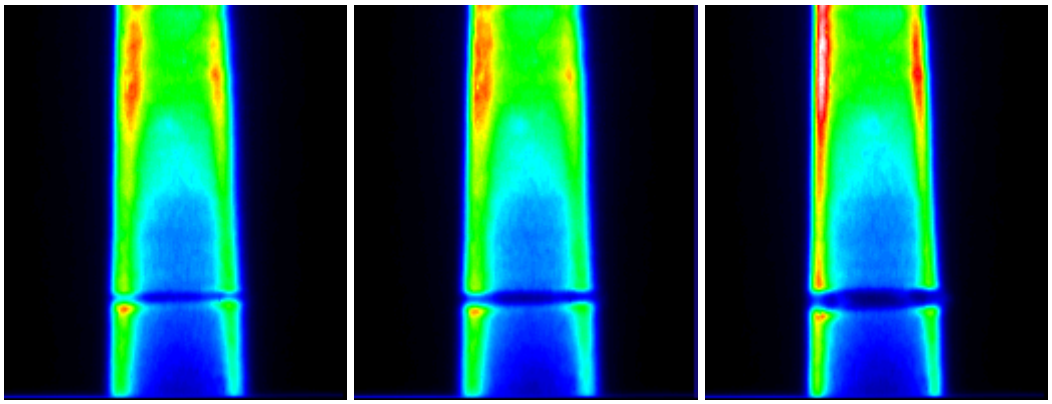

Figure 4-6. Flame data: 100 shot averaged LII images at 40 mm HAB with 1μs delay and three laser fluences: a) 0.84J/cm^2 b) 1.4J/cm^2 and c)4.7J/cm^2. The marking laser sheet is 2 mm wide, and image size 28×24mm.

The 40mm HAB location was chosen since this is where the flame soot concentration reaches its maximum value (oxidation dominates above that height, see Chapter III)

Qualitatively, the marked regions in the averaged soot generator image produced at 0.84 J/cm^2 have the worst observability; it is barely visible in the average soot generator LII images. The marked region is more noticeable in the *instantaneous* soot generator scattering images. On the other hand, the 1.4 and 4.7 J/cm^2 marking laser fluences produce much "clearer" marked regions in the soot generator and the laminar flame.

Figure 4-7 shows the variation in contrast (Eq. 4-1) with marking laser fluence in the laminar flame and soot generator flow, for both LII and scattering detection. The measured contrast increases with laser fluence in all cases, and all have a similar trend: 1) essentially zero contrast for fluences below ~0.4 J/cm^2, which is below the LII signal threshold of 0.6 J/cm^2 (Figure 2-1); 2) contrast can be noticeable at >0.6 J/cm^2, 3) contrast increasing sharply with fluence up to ~2-3 J/ cm^2, and 4) little change in contrast at higher fluences. The noticeable contrast would therefore permit soot concentration measurements based on the LII signal from the imaging laser pulse. Notice that the soot generator contrast data have lower contrasts than the results obtained in the flame. It can be attributed to the much smaller soot particle sizes in the flame, which are less than 50 nm[70] for the primary soot particles, compared to the soot generator, which contains particle above 400nm[68] on average. Generally, for the same laser pulse, the smaller soot particles in the flame will have a higher absorption rate (page 21) than the larger particles produced by the soot generator. Therefore, more mass of soot will be vaporized in the flame for the same laser intensity (providing the laser energy is above the vaporization

threshold), compared to the soot generator. Thus, both LII and scattering contrasts in flame measurement are higher than in the soot generator.

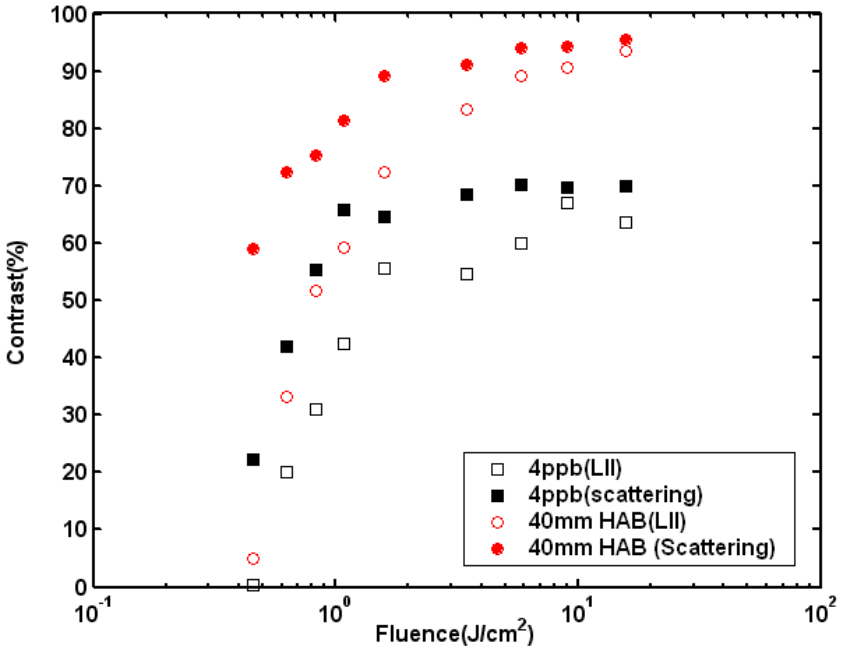

Figure 4-7. Contrast of marked region (see Eq. 2) for various laser fluences at 1μs after the marking pulse, for soot generator (4 ppb soot concentration) and flame at 40 mm HAB; contrasts measured with both LII and scattering detection are shown.

Next, it is useful to note that this near optimum fluence is only 3-4 times the value normally employed in LII measurements. Comparing the result to the LII "threshold" (Figure 3-8), this laser fluence value (for our Gaussian laser profile) is still in the "flat" region, i.e., from 0.6 to 3 J/cm^2, the measured LII signal is almost constant with laser fluence. Furthermore, the fact that near unity contrasts for both LII and scattering detection can be achieved for fluences of 2-3 J/cm^2 suggests that the energy in the center of the roughly Gaussian beam profile is sufficient to nearly completely vaporize the soot particles. While similar contrasts are achieved at high fluence values, there is a

significant difference between scattering and LII detection at lower fluences (<2 J/cm^2), where scattering detection has a higher contrast, and therefore is more detectable.

The difference in contrast between scattering and LII detection can be explained using some simple models. For example in the flame, the soot particles (< 50 nm diameter) are much smaller than the LII detection wavelengths (~400-600 nm). Thus as shown in Chapter 2, the LII signal I_{LII} scales with volume of the radiator, i.e.,

(Eq.4-2) $$I_{LII} \propto a^3 \propto V$$

where a is the radius of the soot particle and V is soot particle volume. From classical scattering theory,[40] small spherical particles ($a<<\lambda$) have an average volumetric polarizability α that is given by:

(Eq.4-3) $$\alpha = \frac{m^2 - 1}{m^2 + 2} a^3 \propto \frac{m^2 - 1}{m^2 + 2} V$$

where m is the refraction index, and the scattering intensity I_{scatt} from the particles is proportional to α^2. Therefore we find,

(Eq.4-4) $$I_{scatt} \propto \left|\alpha^2\right| \propto V^2 .$$

Thus, one can calculate the detection contrast as a function of laser fluence, as the laser changes the particle volume V. A simulation was performed for two uniform pulsed laser beams delayed in time: the initial marking beam followed by the readout beam. Both laser pulses are assumed to have Gaussian temporal shapes with a full-width-half-maximum of 7 ns. A single initial particle size is used (30 nm diameter). The fluence of the 1064 nm marking beam is varied up to 10 J/cm^2 (approximately the maximum fluence used in the experiments) and the model described in Chapter 2 is used to simulate the change in particle size induced by the first laser. In the simulation, the 532 nm readout laser begins 1 μs later and has a fluence of 0.5 J/cm^2. The LII and scattering signals

induced from the readout laser pulse S_{mark} are then calculated from the new particle size with Eq. 4-2 and Eq. 4-4. S_{unmark} is calculated in an identical fashion, but with the original particle size (e.g., zero fluence marking beam). The contrast is calculated from equation (Eq. 4-1). Figure 4-8 shows the results for the simulation.

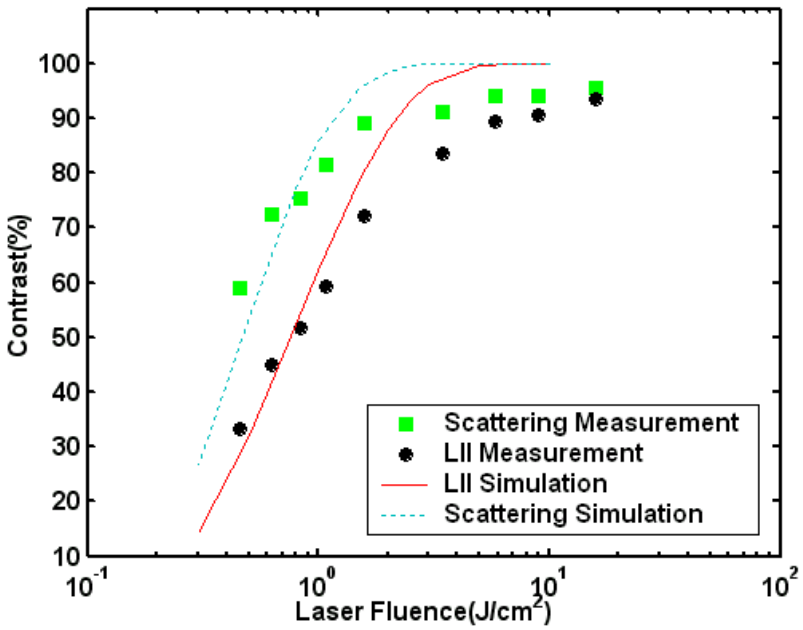

Figure 4-8. Comparison of experimental results and numerical results for both LII and scattering detection techniques.

Note, **the simulation results have not been normalized or matched in anyway to the data**, as the expression for contrast is self-normalized. First, it can be seen that there is quite good agreement between the simulated and measured contrasts for both LII and scattering at low laser fluence (<1.5 J/cm^2, which is three times the LII threshold fluence). In fact, the deviations between simulation and experimental results are less than 7%. At high laser fluences (>1.5 J/cm^2), however, the simulation predicts higher contrasts than those observed in the flame. This is most likely caused by the simplifications used in the modeling of the laser heating process. At high laser intensities, one very important process not captured in the current modeling is thermal annealing.[71]

Extremely high laser heating rates can cause carbon morphological changes, which result in rearrangement of the carbon crystallites and alter soot density, instead of simply vaporizing soot. Thus the particle sizes predicted after high fluence heating are probably not accurate from the current model. Still, the fact that both the experiments and simulations show that LII and scattering detection have vary similar contrasts at high fluence levels indicates that the particle size is close to zero, i.e., the first laser pulse is truly vaporizing particles, and not simply shattering them.

The results show that the scattering signal contrast is higher because scattering is more sensitive to changes in particle size. For the soot generator measurements (not simulated here), there is less difference between the contrasts of the two detection methods at low fluences because for the larger particles (~400 nm in the soot generator) the scattering signal scales more like $V^{4/3}$ (compared to V^2 for small particles). In addition, part of the increased observability for scattering detection could be its improved signal-to-noise ratio, due to its higher photon yield in these shot-noise limited images. This is only a minor effect, since the scattering images are acquired with lower detection efficiencies.

4.2.4. Lifetime of Marked Area

The applicability of flow tagging approaches is often limited by the lifetime of the marked region. In other words, the time delay between the marking laser and the readout image has a maximum value. This is important since longer delay times allow low velocities (with their associated smaller displacements for a fixed delay time) to be detected more easily. Furthermore, by tracing the evolution of a marked area over a longer time, one can study vortex development and how flowfield interactions influence

the reaction zones in a flame. However, the lifetime of the marked area can be limited by mixing processes, such as the diffusion of particles from higher particle concentration areas into the soot free zone. This mixing is enhanced in unsteady flows due to convection. In addition, the tagged region in PVV can be "nullified" by the production of new soot particles inside the marked area. So the marking area lifetime is an important characteristic for particle vaporization velocity measurement.

As indicated by Figure 4-9 (initial height 40 mm HAB) and Figure 4-10 (20 mm HAB), the lifetime of the marking region in the diffusion flame exceeds 10 ms. However for the lower initial position in the flame, the marking region becomes more difficult to see for long delays; the soot either refills or reforms in the marking region (see images c and d in Figure 4-10). The contrasts (determined at the edge of the flame) for three initial locations (10, 20 and 40 mm HAB) are shown in Figure 4-11. For the lower regions, 10 and 20 mm HAB, it can be seen that the contrast decays more quickly than at 40 mm HAB. The 10 mm HAB is the lowest region where noticeable soot formation occurs, and where the soot concentration is lowest. Conditions are favorable for soot formation above this height. In **Error! Reference source not found.**, it can be seen that soot formation typically occurs in about 1-2 ms at high temperatures. So, it is likely that the contrast decline with delays longer than ~1ms at low flame height is most likely due to formation of new soot particles or growth of the partially vaporized soot within the marked stripe. Also at low flame heights, there is much less soot in the central portion of the flame. Therefore the laser mostly vaporizes soot at the edge of the flame. As indicated in Figure 4-10 (c), the gas that travels to the flame edge as the marked region moves upward comes

from a location that did not have much soot to begin with. Therefore the laser is less likely to have influenced the evolution of soot in that fluid element.

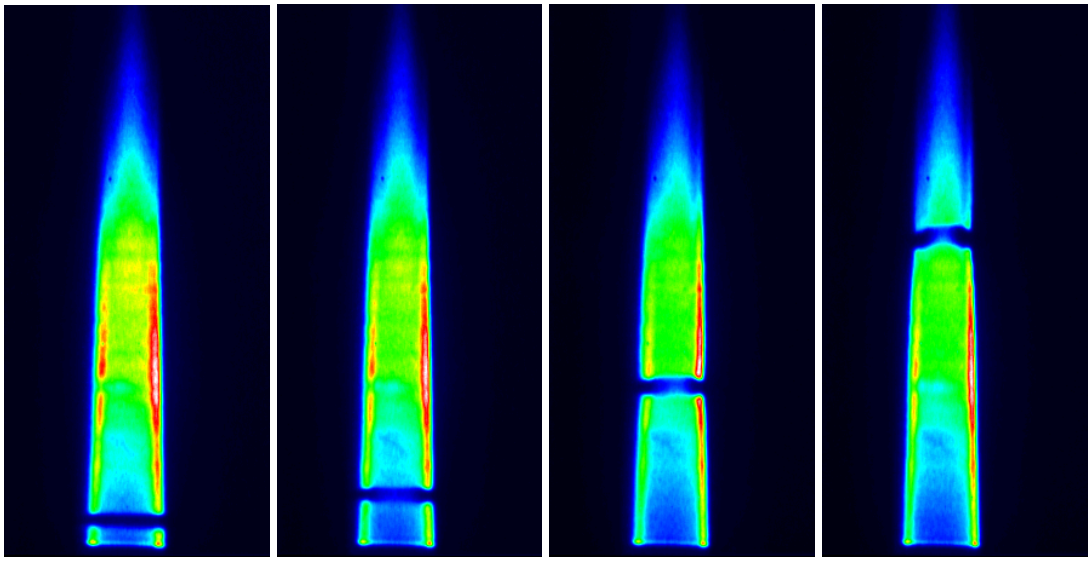

(a) (b) (c) (d)

Figure 4-9. Average (100 shot) LII images of the vaporized stripe acquired in the diffusion flame for four delays: a)10 μs, and b) 1ms c) 5ms d)10ms after the 3 mm wide marking laser sheet pulse; which passes 40 mm above the fuel tube exit, image size 31×18mm.

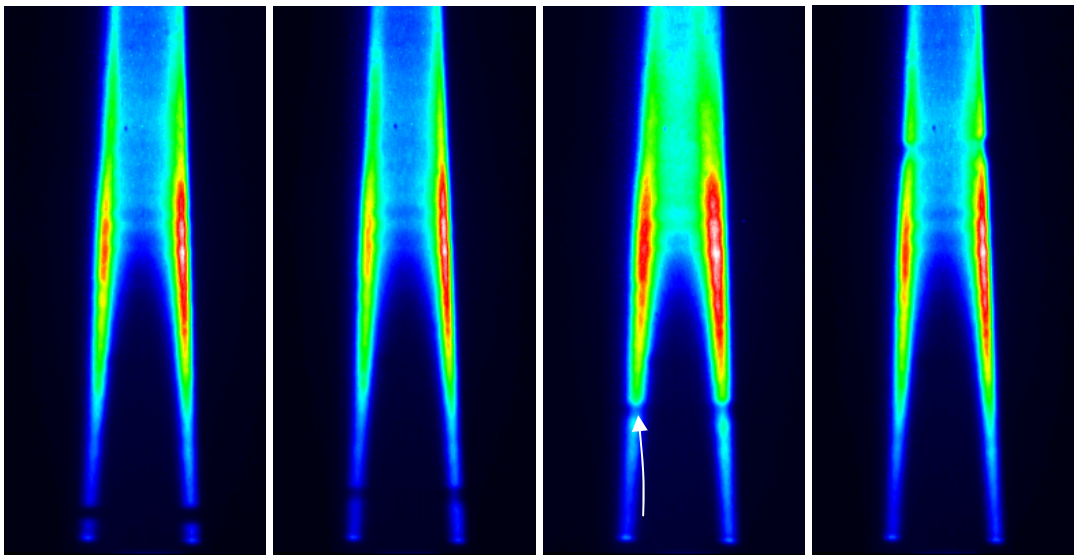

(a) (b) (c) (d)

Figure 4-10. Average (100 shot) LII images of the vaporized stripe acquired in the diffusion flame for four delays: a)10 μs, and b) 1ms c) 5ms d)15ms after the 3 mm wide marking laser sheet pulse; which passes 20 mm above the fuel tube exit, image size 31×18mm.

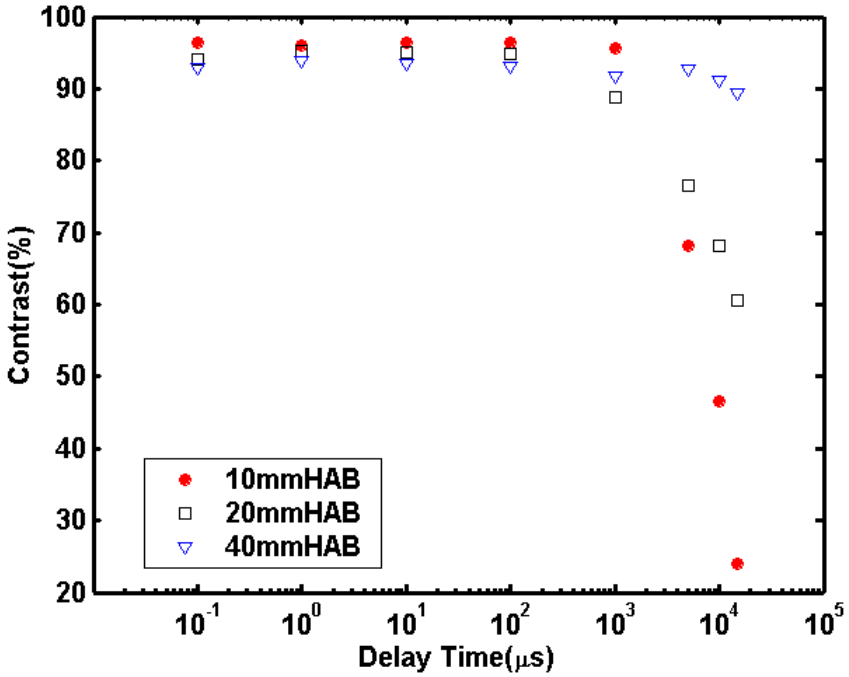

Figure 4-11. Lifetime of the vaporized soot "hole" in the laminar diffusion flame based on the contrast between the marking and readout lasers, for a marking laser fluence of 7.8 J/cm^2. Results are shown for three flame heights and for LII detection.

An interesting question is why the contrast remains so high for the data taken with an initial height of 40 mm. Returning to the LII images for this condition (Figure 4-9), one can see that there is almost no soot formation within the marked region for the different delays after the laser, except perhaps near the centerline. A major difference between the 40 mm HAB location and the lower heights examined is that there is a significant amount of soot initially present all the through the flame at 40 mm HAB. Therefore the marking laser changes the local conditions across the complete flame. Furthermore, above 40 mm HAB the soot volume fraction no longer increases with increasing height.[28] Thus, the natural soot formation has stopped at this point. So, there is no source of soot to refill the marked region with soot.

This still leaves the question, what happens to the vaporized soot material? When the laser vaporizes soot, it is believed that the vapor products consist of C, C_2, and C_3 radicals,[72] with C_2 radicals predominant[73 - 76] Also, the translational and internal temperatures of the gaseous C_2 are close to the surface temperature of the vaporizing soot (>3500K).[77] From the current results, it is clear that the C_2 radicals do not recondense to form soot particles. Rather, they are likely reacting with other species due to their high energy and high reactivity (C_2 has two unpaired electrons). For example, C_2 radicals are known to react with H_2 to form C_2H, through an abstraction reaction, i.e., $C_2 + H_2 \rightarrow C_2H + H$,[78] or through reactions with nitrogen.

It is even possible that the laser acts to inhibit soot formation. This could be due to the reactivity of the vaporized material inhibiting either soot nucleation or soot surface growth. On the other hand, rapid laser heating can cause thermal annealing of the soot particles, forming "carbon onion" structures with a hollow core.[77] Thus even if the soot particles are not completely vaporized, the surface of the annealed particle may have less active sites and thus be less conducive to surface growth than nascent soot particles.

Finally, it is possible that the reactive C_2 radicals act to increase the soot destruction rate, thereby inhibiting soot growth. For example, C_2 can abstract an H atom from water, which would be present due to diffusion from the flame zone, thereby forming an OH radical ($C_2 + H_2O = C_2H + OH$).[79] Since OH is the major oxidizer of soot in fuel rich conditions, it would act to destroy small soot particles before they have a chance to grow.

After all, similar lifetime measurements were carried out in the soot generator flow. Figure 4-12 shows instantaneous soot generator LII images at three delay times:

100 ns, 1 ms and 3 ms respectively. It is evident that the marked line distorts significantly for longer delay times.

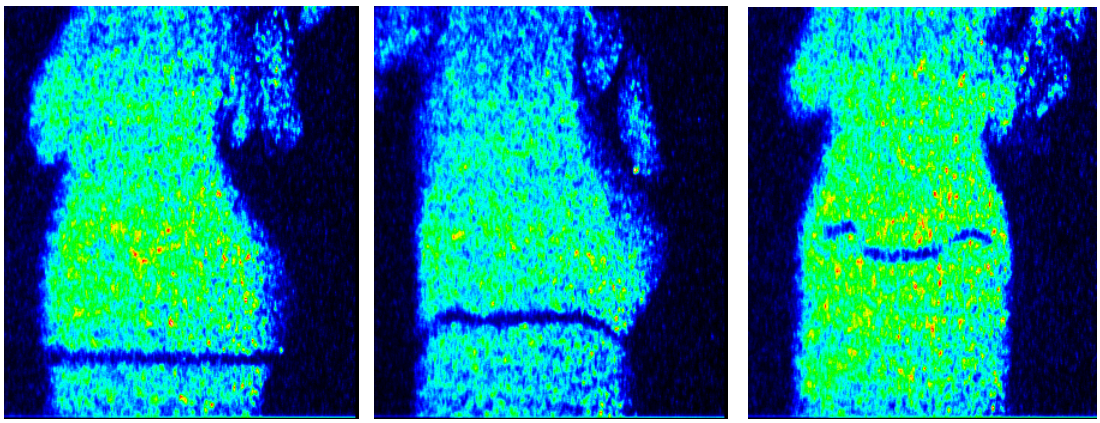

(a) (b) (c)

Figure 4-12. Soot generator instantaneous LII images at three delay times (a)100ns, (b)1ms (c) 3ms. Image size is 28×24mm.

From average soot generator images, the lifetime (Figure 4-13) of the marked region is shorter than in the upper portion of the flames; it is close to the 1 ms value observed lower in the flame. Even it is possible that the vaporized soot material is recondensing to form carbon particles, this is unlikely. The vaporized radicals are more likely to react with the oxygen present in the air. Rather the soot generator flow is more unsteady, because it does not have a low shear coflow like that employed in the diffusion flame burner. Thus convective mixing phenomena (i.e., related to the distortions displayed in Figure 4-12) probably limit the lifetime in the soot generator flow. Noticed at 100 ns delay, the marking region contrast is lower than of the 1 μs and even 1 ms delay. This low contrast is most likely due to the remainder of the LII signal from the marking laser pulse for this short delay.

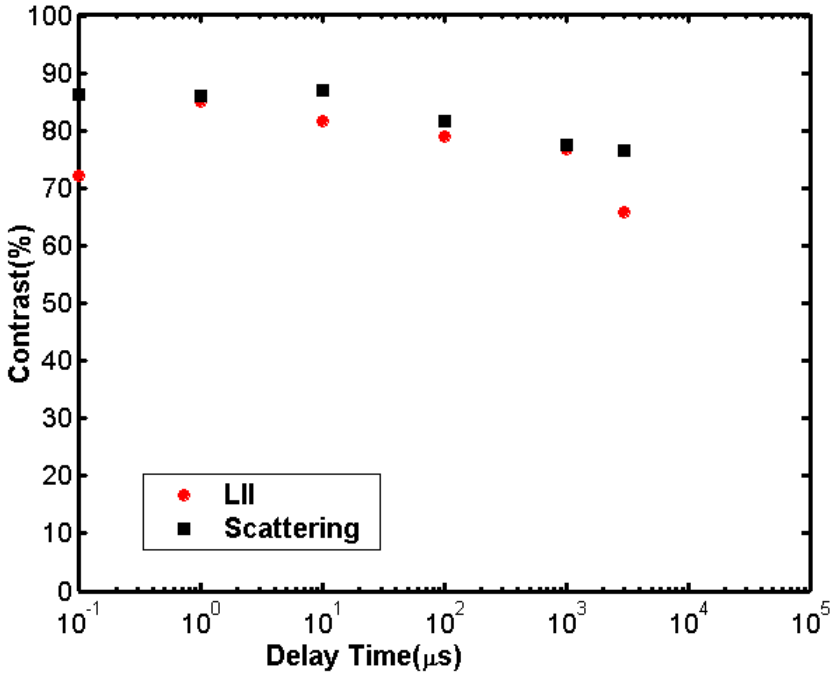

Figure 4-13. Lifetime of the vaporized soot "hole" in the soot generator flow based on the contrast between the marking and readout lasers, for a marking laser fluence of 7.8 J/cm^2. Results are shown for both LII and scattering detection.

4.2.5. Detection Methods

During the experiments, the scattering signal was acquired with a 30-50 ns intensifier gate, which began with the onset of the laser pulse. Because the green laser pulse width (FWHM) is about 8 ns, the prompt scattering signal includes both scattering and LII. Even scattering signal has much higher signal level, the LII signal alone can be acquired either by placing a 532 nm notch filter in front of the camera, or delaying the camera gate time a short time (e.g., 30 ns) after the readout laser pulse. The latter method would incur some loss of LII signal at the peak of the laser pulse, but the LII signal still should be high enough to be detected due to the long lifetime of LII. From the above results, the main advantage of scattering detection for PVV is its higher photon yield, and thus higher signal-to-noise ratio in these shot-noise limited measurements. In both the

soot generator and the flame cases, the scattering signal is much stronger than the LII signal. Correcting for the added ND filter in the case of the scattering images (ND = 2.6), the scattering to LII ratio in the flame is 100-200. In the soot generator, the ratio decreases to 30-60. A larger scattering to LII signal ratio is to be expected in the flame, since the soot generator produces larger, spherical agglomerates. For scattering from very small particles (compare to the laser wavelength), the cross-section, or signal per particle, increases rapidly with particle size (e.g., D^6). If particle size is comparable to the laser wavelength (soot particle size>400 nm, IR laser wavelength is 1064 nm), the scattering signal is almost proportional to D^4. On the other hand, the LII signal per particle scales like its volume (D^3). Therefore, the larger particles in the soot generator would produce relatively less scattering per unit mass of soot. In addition, other differences between the two kinds of soot (flame soot and carbon black particles) may play a role. For example, changes in the chemical composition would likely change the index of refraction of the soot, and thus its scattering and absorption.

An important fact to be noticed from Figure 4-1 is the scattering images (1[b] and 1[c]) have measurable signals outside the soot jet while the LII image (1a) does not. This is due to elastic scattering by dust particles in room air, and it is the biggest potential drawback of scattering detection, ejection of other scattering particles or bodies. In a confined combustor, scattering from walls and windows can be sources of significant background for scattering detection. For the flame case, however, with its much high soot levels ($\times 10^3$) and its clean coflow, dust scattering signal is negligible. Overall, the signal-to-background ratio for LII is better than that for scattering in both the soot generator and

flame. For example, in the soot generator, the signal-to-background ratio of the LII detection is 6.7, while that of scattering detection is only nearly half of that value.

4.3. ONE-DIMENSIONAL VELOCITY MEASUREMENTS

In previous sections the excitation, detection and marked-region, lifetime characteristics of soot PVV are described. Based on these results, it is now possible to optimize the experimental parameters for a given flow. In following sections demonstrations of PVV for flowfield velocity measurement are depicted.

4.3.1. Basic Velocity Measurement and Uncertainty

For the initial demonstration, a simple flowfield is preferred. The soot generator produces such a flow. It is a relatively steady, nearly one-dimensional flow associated with a laminar jet. For example, the axial velocity decays slowly along the jet axis in the downstream direction. The diffusion flame also starts out as a jet-like flow, with an even lower shear produced by the coflow. In the flame, the local heat release alters the downstream velocity development. Since the velocities are changing with position in both these flows, accurate local velocity measurements are achieved with small displacements of the marked region (i.e. short delay times). In addition, if the second laser beam has a very short delay from the marking beam (compared to the mean flow time scale), it can be assumed the flowfields are stable, and the change in the velocity during the measurements is negligible. All the local velocity data reported here are based on the displacement of the marked area using ~1ms delay times.

We first consider comparisons of single point velocities measured in the flame and soot generator flow. At 40 mm above the burner in the flame, at the point of maximum soot concentration, the measured displacement is 1.8 mm, which results in a

PVV velocity of 1.8 m/s. This compares well to a previously measured LDV result of 1.7 m/s at this location.[80]

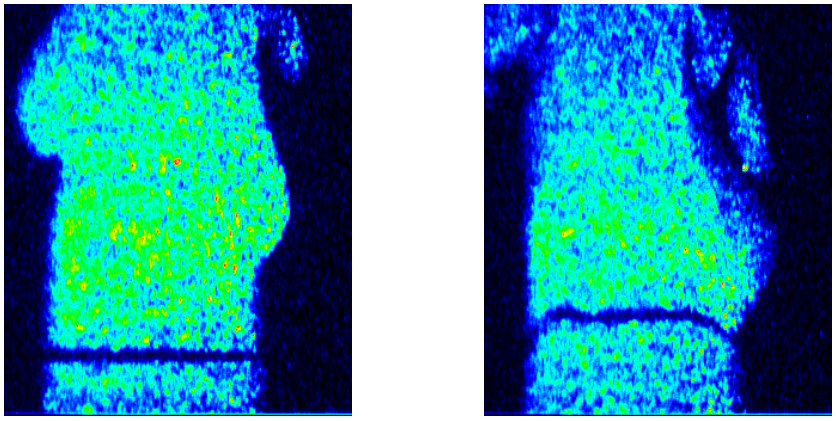

(a) (b)

Figure 4-14. Soot generator instantaneous LII images at 2 delay times (1) 1μs and (2)1ms Image size is 28×24mm.

In the more unsteady soot generator (see Figure 4-14), we first compare the average displacement of the marked region, temporally averaged over 100 images (50 sec.) and spatially averaged across the jet width. The result at the measurement height (2 mm= 0.1 *x/D* above the jet exit) determined from the LII detection image is 2.7 m/s. This compares well with the averaged jet exit velocity of 2.8 m/s calculated from the volumetric flowrate of 713 cm^3/s (with the cold flowrate measured by rotameters and this value calculated based on the measured jet exit temperature of 120^oC). In addition, one would expect the velocity above the jet to be slightly less than the exit velocity.

In PVV measurements, the velocity measurement error can be generated from both the time measurement and the displacement measurement. The delay timing for PVV here is controlled by a pulse generator with a jitter of <1ns. Since the delays used here are typically on the order of 1 ms, the error time measurement is less than 1 part per million. Therefore, delay time uncertainty is a negligible source of error. On the other

hand, the measured minimum displacement of the marking line is limited by the ICCD resolution, the uncertainty is around 1/2 pixel size. The effective resolution of the ICCD camera depends on the physical size of the ICCD pixels and the magnification of the lens. In the current measurements, the pixel resolution is ~0.1 mm, and delay time is ~1ms. Thus the velocity error due to system uncertainties is roughly $1/2 \times 0.1mm/1.0ms = 0.05$ *m/s*.

In PVV measurements, the vaporization process can also alter the local flowfield. The vaporized material represents an increase in local gas density and an increase in local enthalpy. For example in a flow at 1 *atm* and 1500 K with 1 ppm of soot, and if the laser **completely vaporizes** the soot to form gaseous C_2 at 4000 K (~the vaporization temperature), the C_2 mole fraction would be 0.7%. If the vaporization process was nearly instantaneous, the local gas pressure would increase by ~0.7%. Thus the vaporization can produce a fairly small expansion, and, this would not change the flow velocity significantly in most reasonable flow conditions. Similarly, the gas temperature would be increased by ~20 K if all the vaporized gas thermalized without reacting. Since soot is normally found only for temperatures above 1000 K, this relatively small change in temperature (<2%) could cause a similar change in velocity.

4.3.2. Velocity Profile

In addition to measuring the average velocity of the flow field, the one dimensional local velocity can be measured by tracing the movement of different "points" on the tagged line (see Figure 4-15). By comparing the images with and without delay of the same flow, the displacement of each point on the tagged stripes along the

tube diameter can be calculated, and then the axial velocity profile of the flow can be plotted.

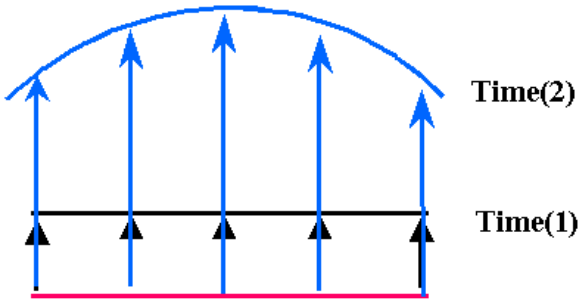

Figure 4-15. Scheme for 1-d velocity profile measurement by tracing marking line.

Figure 4-16 shows the measured velocity profiles at 1.0ms delay (from image in Figure 4-1(b)) and at 3ms delay after the marking beam. Both fall between a calculated fully developed, laminar jet profile (parabolic) and a plug flow profile (flat). For plug flow, the velocity is calculated from the following (where $\dot{m}$ stands for mass flowrate, and A for jet area):

(Eq. 4-5) $$V = \dot{m} / A$$

The fully developed profile has the same volumetric flowrate (after axisymmetric integration), but with a parabolic velocity distribution.

The results suggest the flow in the pipe that produces the jet is not fully developed. The required minimum tube length for laminar, fully developed flow for a tube of diameter D, is $L_{min} = 0.06\ Re \times D$.[81] In the soot generator, Re~2000 and D = 18mm, so the required L_{min} is roughly 2 m, which is much longer than the actual tube length (~0.3m). So near the center of the jet, the flow is closer to a plug flow, but near the boundaries, the developing boundary layers in the pipe produce a profile more like that of the fully developed flow.

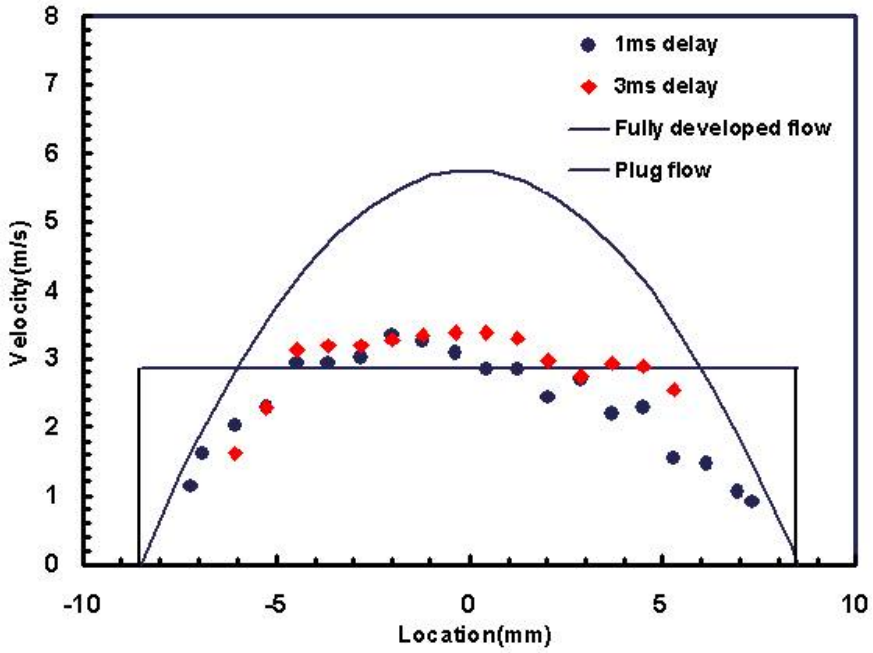

Figure 4-16. The instantaneous velocity profile of soot generator at 1ms and 3ms delay time, 15 mm above the jet exit, and calculated the fully developed and plug flow profile at the exit of the heating tube.

4.4. PVV IN AN UNSTEADY COMBUSTION FLOWFIELD

The above results show the successful development of PVV in two simple, laminar jet flows. Practical flowfields, on the contrary, are typically unsteady and turbulent. This demands a more complicated optical arrangement to acquire more than one velocity component. In the following section, the PVV velocity measurement technique is extended to a 2-d approach and demonstrated in an acoustically forced combustor. The combustor was chosen for its ability to simulate a more practical, unsteady environment.

Inside the acoustic burner, due to the unsteady forcing of the acoustic velocity field, the flame fronts are highly irregular. This makes the single marking stripe method inappropriate. The marked line, which travels steadily in laminar flows, is quickly distorted in a highly 3-Dimensional, unsteady flow. Therefore, tracking the movement of

the marked region requires a more sophisticated method to uniquely determine the mapping between the initial measurement location and the delayed location of the marked region. Thus, the PVV measurement has been modified to a two-dimensional approach using a crossed beam excitation method, as illustrated in Figure 4-17. At the crossing point of two laser beams, one can uniquely identify a fluid element in the flow, which can then be tracked over time.

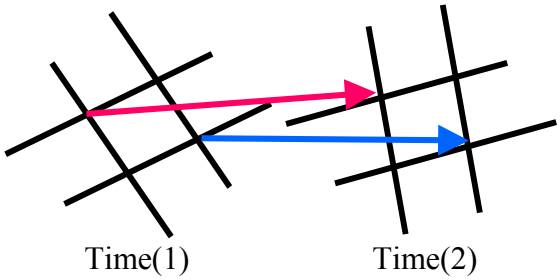

Figure 4-17. Scheme for 2-D velocity measurement by tracing of marked grid produced by crossed laser beams.

Due to the unsteady mixing, in the acoustically forced flame, the marked region will also have a much shorter lifetime (depending on the laser intensity and forcing intensity) than in the laminar flame and soot generator flowfields. Thus, a shorter delay time is preferred in the unsteady flow, so the displacement of the marking area can be determined clearly.

Figure 4-18 consists of two LII images from the readout beam at different delay times relative to the marking beam. The first image (a) was taken at a 1μs time delay, while the second (b) is for a 200 μs delay. Both images are for a fuel flowrate of 10.5cm^3/s. In Figure 4-18(a), the four crossing marking lines are very clear. Based on the initial design, the four beams form a “diamond-shape” like grid (4 mm high × 12 mm wide). Due to the size of the flame, part of the “grid” is out of the soot field in this image. However, most of the "diamond" is still visible. For example the two vertical intersection

points (vertices) can be seen, but the left and right vertices are not. The downstream vertex is denoted the "top" point, and the upstream crossing is the "bottom" point

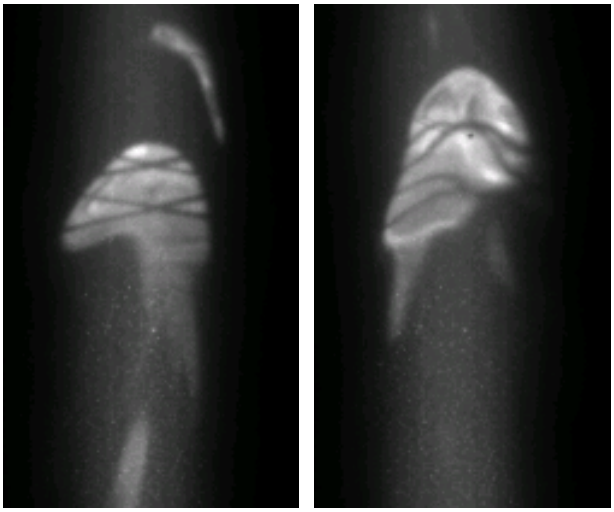

(a) (b)

Figure 4-18. Crossbeam images for acoustic forced flame, image size: 20mm(W)× 33mm(H); (a) LII image of crossbeam at 1μs delay after the IR (marking) laser; (b) the LII image at 200μs delay.

In the delayed image (b), there is clearly a significant distortion of the marking lines due to the three dimensional character of the acoustically forced flame. The top and bottom points generally move towards the top right. If we trace the displacement of the physical center for the crossing lines, together with the known delay, the two-dimensional velocity of the "local" flow can be measured.

4.4.1 Averaged Velocity Measurement

For each flame condition, an accumulated image of at least 100 individual laser pulses is collected to calculate the average flow velocity, while 50 instantaneous images are acquired to measure the instantaneous velocities Because of the unsteadiness in the flow field, the soot field does not always overlap the marking laser's grid region, some of the images miss marking lines. Therefore, the contrast of the marked lines in the average images decreases much faster compared to that of the laminar flame. There is also a

tradeoff on the time delay for instantaneous flow velocity measurements. The shorter the delay time, the better local accuracy of velocity (which is changing with time and space) can be acquired. However, short delay also produces a smaller displacement of the marking line, therefore, the relative displacement error could be big due to the limitation of the ICCD resolution. Thus, it is hard to accurately measure velocity data at too short a delay time.

In this experiment, a 100 μs delay was chosen for the average velocity measurement, because it is not a long delay time relative to the fuel flow velocity (the fuel jet velocity is less than 20 m/s), and the displacement of the marked grid can be read (more than 6 pixels generally) in our experiment. The "original" location of the crossed beams is determined from an LII image with a 1 μs delay after the IR laser. This delay removes the interference from the residual LII produced by the IR marking laser pulse (see previous laminar flame results), without altering the location of the marked region. The physical center of the marked vertices is selected as the marked region.

As an example of the capabilities of the technique, Figure 4-19 displays the average velocity measurements as a function of phase in the acoustic forcing cycle. Results are shown for the top and bottom grid crossing points, as well as the average of these two values. In addition, the acoustic velocity calculated from the measured acoustic pressure is also plotted. The measured flow velocities vary as expected with the acoustic phase. The peaks (maxima and minima) in the velocity occur at phase angles of 0°, 180° and 360°. Phase drift between the signal and trigger outputs of the signal generator result in a phase uncertainty of as much as 18°.

The measured velocity at the top intersection varies between 8 and 16 m/s (12±4 m/s), while the bottom point velocity is between 4.3 and 14 m/s (9.1±4.8 m/s). For comparison, the average velocity of the flame is around 11 m/s without acoustic excitation. From these results, the acoustic velocity is roughly the same at both points (4-5m/s), but the average velocity is 2-3 m/s higher for the top point at most phases. This is likely due to heat release. The top intersection is located further from the fuel jet exit. By this point, the flowfield has experienced more fuel-air mixing and heat release, which generates (through expansion) higher velocities.

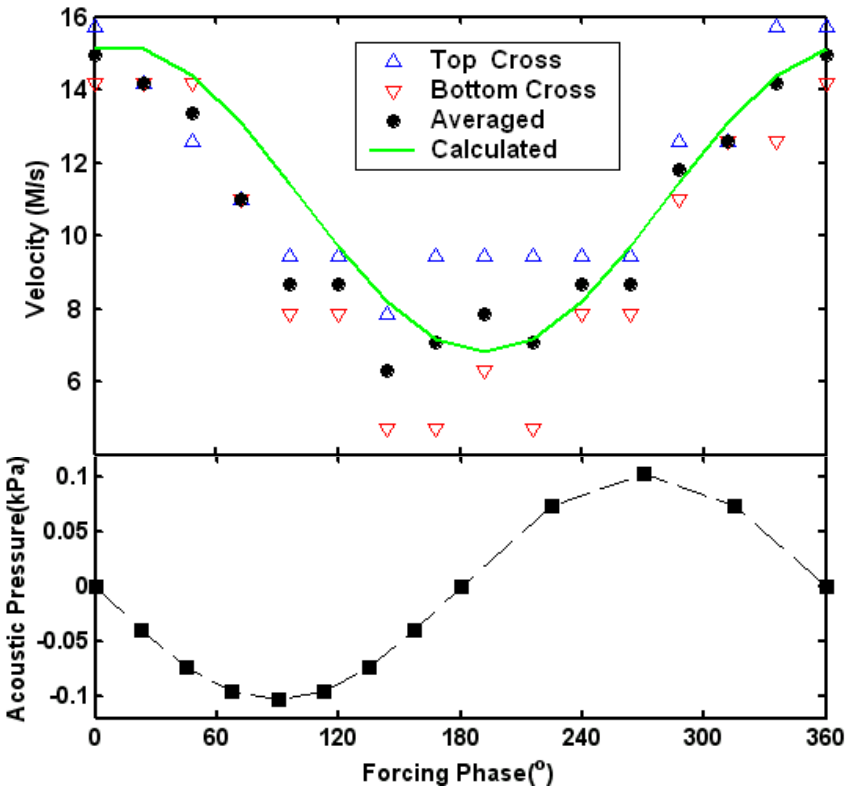

Figure 4-19. Measured average axial flow field velocities are phased-locked, at various phases in the cycle of acoustic driving pressure. Each data point is an average of 200 laser pulses. Numerical flowfield velocities are calculated at 1700K.

The time accumulation process of images can average out a lot of local flow information. Thus, the study of instantaneous images is significant to understand local flow velocity field.

4.4.2 Instantaneous Velocity Measurement

From the individual images, instantaneous, two dimensional velocities at the beam crossings can be calculated. Furthermore by tracing multiple points along each marking stripe (providing each of their corresponding locations can be determined after certain delays), a more complete two dimensional velocity field can be resolved. This could be useful for tracing the evolution of a flowfield, and the structure of vortices in the unsteady flame.

Apparently, in order to achieve accurate local 2 dimension velocity measurements, it is optimum to acquire images with all 4 beam crosses displayed at same time, thus local velocity at these 4 points can be measurement; furthermore, it is possible to calculate more velocity points by interpolating measurements between adjacent crossing points. But, in practical process, due to limitation of the optical setup, small flame size and unsteadiness of flow field, it is hard to acquire one image with 4 crossing points. Thus, images with 3 crossing point are selected to examine the testing flow field.

Figure 4-20.shows forced flame images with crossing grid. Image(a) is taken at 1μs delay time after marking laser, the entire grid is hold in original shape, i.e. each marking line is straight. Obviously, during acoustic forcing, these straight lines will be curved as they follow the movement of unsteady flowfield. Images (b), (c), (d) and (e) are acquired at 200μs delay after marking laser and 4 different forcing phases. These phases chosen is mainly based on the averaged velocity measurement results, and selected from

phases with different averaged velocities.

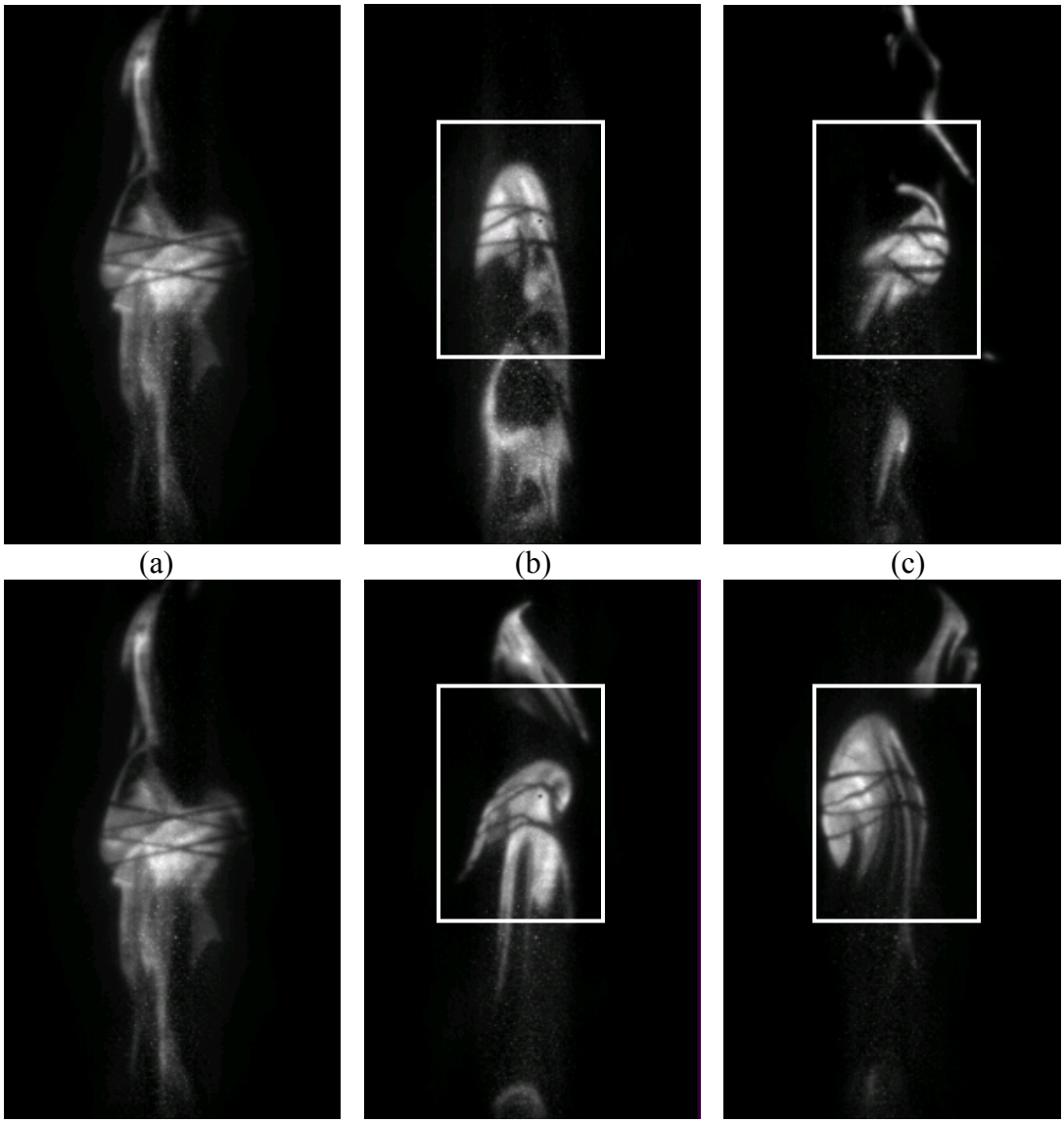

Figure 4-20. acoustic forced flame images (a) at 1μs (2 images combination) (b)200μs delay at 48° (c) 200μs at 168°(d) 200μs at 264° (e) 200μs delay at 336° (image size is 46.5×28.7mm).

Despite the big original image size in Figure 4-20, only part of the regions with marking lines will be processed to calculate local velocity, as marked area in Figure 4-20 (b),(c),(d) and (e). Noticed in Figure 4-20, all images displayed have at least 3 cross

points. Thus, linear interpolation point velocity between two adjacent cross points can be measured. Because the grid horizontal (X-axis) size is longer (12mm) than vertical (4mm) size, so, it is easy to linearly interpolate 2 X-axis locations between two adjacent cross points, and then find their corresponding Y-axis locations on the marking line. By measuring the X-axis and Y-axis changing of corresponding points between 1μs to 200μs images, the local velocities can be calculated.

In Figure 4-21, it displayed the measured 2-dimensional velocity vectors from Figure 4-20 image (b), (c), (d) and (e). Velocity vectors on these 4 images clearly show the velocity variations at different locations, and the pattern of velocity vectors is different at each forcing phases. Especially, at some phases, a few (c) or some (b) of the velocity vector directions are opposite to the main flow velocities, these suggest larger shear stress and rotation exist in these flow regions, which can form vortices structures and entrain ambient area inside flame flowfield. In addition, from these vectors, the averaged mean velocity can be calculated. These mean velocity are (a)9.7m/s at 48° (b)1.2 m/s at 168° (c)12.1m/s 264° and (d) 15.8 m/s 336°, compare to the measured averaged velocity results, which are 11.0m/s, 6.3m/s, 8.6m/s and 14.2m/s at corresponding phases. Even the instantaneous velocity data are exactly same as the averaged data due to the unsteadiness of flowfield, but they have the similar trend.

Since all velocity vectors in forced flame field are consist of mean velocity and local acoustic velocity, the local acoustic velocity can be calculated by subtracting mean velocity from total local velocity. Figure 4-22 (a), (b), (c) and (d) show mean velocity modified velocity vectors at Figure 4-21(a), (b), (c) and (d), respectively. The velocity vector pattern in each image clearly shows the rotation of the flow, with centerline

velocity vectors pointing upwards, and edged vectors pointing downwards, no matter the flow rotation is clockwise(b) or anticlockwise((a) (c) (d)). A important notice in Figure 4-22 is: the maximum rotation velocity vectors are similar magnitude, despite the averaged mean velocity is. This suggests the rotational flow with lower mean velocity transports less distance. Thereby it has longer residence time for local mixing.

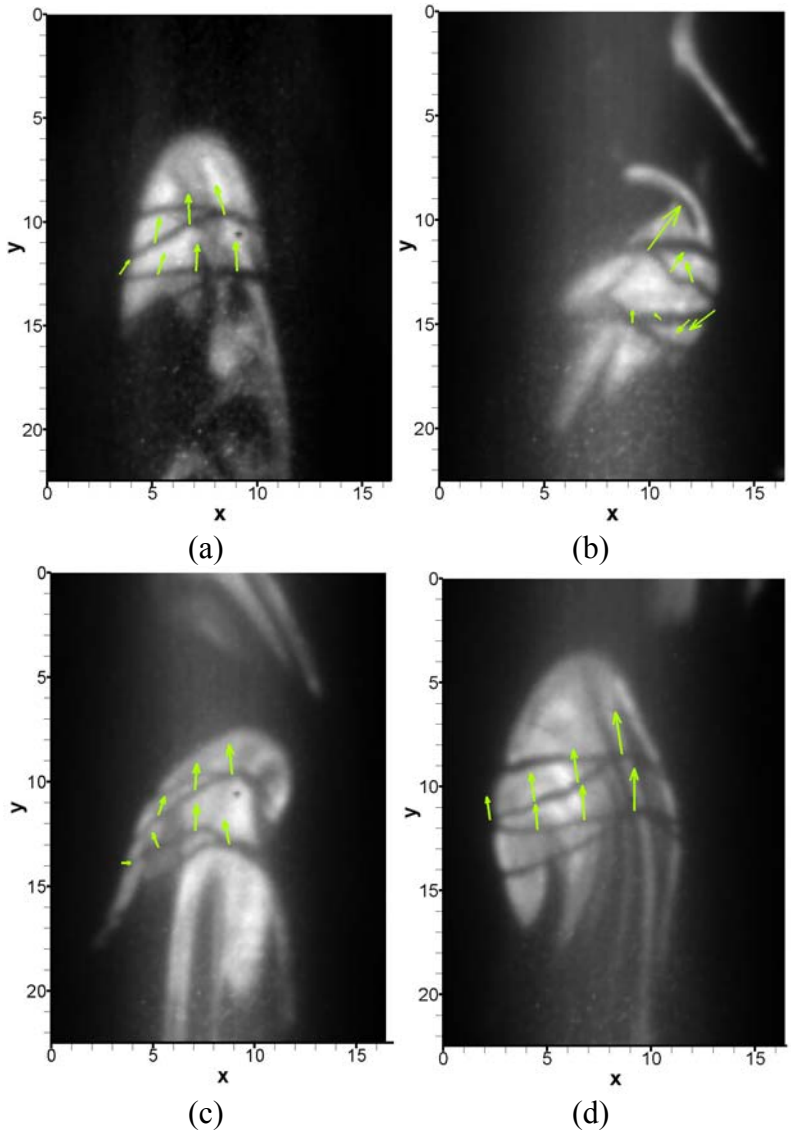

Figure 4-21. Calculated velocity vectors from Figure 4-20.at marked regions (a) (b) (c) (d) correspond to Figure 4-20 (b) (c) (d) (e), the scale unit is millimeter. Size of velocity vectors in (b) are multiplied by factor of 2.

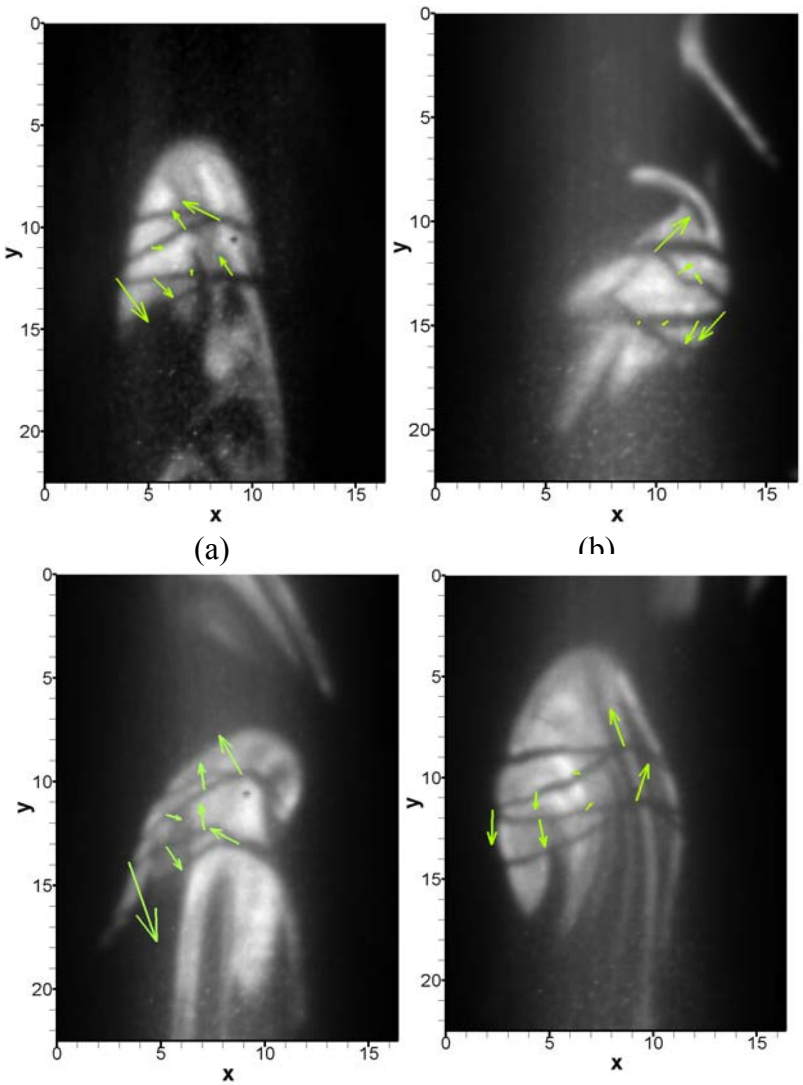

Figure 4-22. Calculated velocity vectors in Figure 4-21 after mean flow velocity subtraction. (a) (b) (c) (d) correspond to Figure 4-21 (a) (b) (c) (d), the scale unit is millimeter. Size of velocity vectors are multiplied by factor of 4 on the bases of Figure 4-21 (a), (c) and (d).

4.5 SUMMARY

Particle Vaporization Velocimetry (PVV) appears to be a viable method for velocity field measurements in sooting combustion flows. Results show that it can be used in both flames (reacting gases) and in exhaust flows. The optimum laser fluence for creating the tagged region is approximately 2-3 times the LII threshold fluence. LII

detection would typically be preferred over scattering detection as it has less background problems. Lifetime studies show that the tag lifetime is quite long. In flames, the major lifetime limitation are oxidation of the soot surrounding the tagged region and turbulent mixing. In exhaust flows, only mixing will likely limit the tag lifetime. The major sources of uncertainty for PVV result from minimum detectable displacement, which can be improved by increasing the detector resolution, and the presence of soot, since the measurement only works where soot is present. Laser perturbations to the flowfield (e.g., temperature, velocity, and pressure) are estimated to be small in typical conditions, though vaporization of the soot in flames clearly seems to inhibit production of new soot, possibly due to the C, C_2 and C_3 radicals produced. Thus some chemical perturbation of the soot vaporized region is likely.

CHAPTER 5

UNSTEADY SOOT CONCENTRATION MEASUREMENTS

In this chapter, an examination of the effect acoustic forcing has upon soot concentration and soot radiation is presented. The goal is to understand the specific observations of Ref. 36 and to study unsteady soot formation and destruction processes in an environment more controllable than a turbulent flame. Results are presented for a steady, acetylene laminar jet diffusion flame and a transitional flame. Both flames are over ventilated. The LII technique is applied to measure two-dimensional flame soot concentrations (the calibration process for determining absolute soot concentration from LII is described in Chapter 3). The data include average and instantaneous soot concentrations. In addition, soot luminosity results corresponding to each flame condition are presented. Various analysis techniques are used to explore unsteady soot formation/destruction inside the flames.

5.1 ACOUSTIC FORCING CONDITIONS

Generally, the effectiveness of acoustic forcing depends both on forcing frequency and forcing power (i.e., power supplied to the sound drivers). The flame size and shape can be greatly varied corresponding to the forcing power (see Figure 5-1). At a given forcing frequency, increasing the forcing power changes the flame surface from smooth (at low forcing power) to corrugated; the flame can even be broken up and torn such that multiple flame sheets exist. Qualitatively, this is similar to the structures seen in a turbulent flame. During acoustic forcing, the flame also shrinks (vertically). At high

forcing power, part of flame can even be “pulled” below the height of jet exit (rightmost image in Figure 5-1).

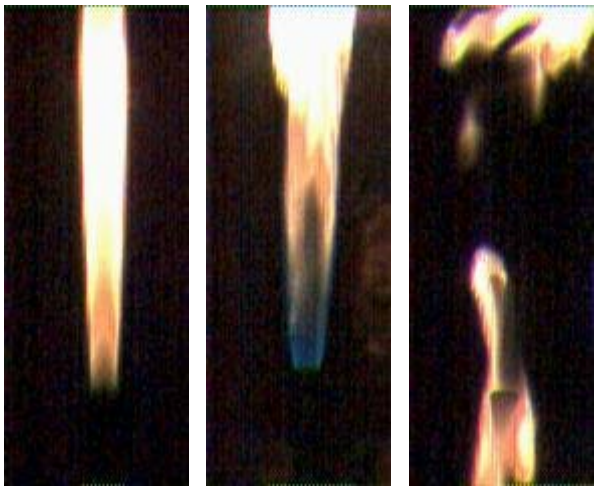

Figure 5-1.High speed color camera images of acetylene diffusion flame at three (increasing) forcing powers for 320Hz forcing (28×13 mm).

In contrast at fixed input power, the forcing effect varies with forcing frequency. A major issue is the frequency relative to the resonant frequencies. The local forcing amplitude (inside the burner) will reach its maximum at the burner’s harmonic modes. The second harmonic mode of the burner was found to be the most effective one; thus, it was chosen as the forcing frequency in all experiments.

5.2 AVERAGED SOOT CONCENTRATION AND FLAME LUMINOSITY MEASUREMENTS

Time-averaged LII data for both laminar and transitional flames have been acquired in these experiments, as well as time-averaged broadband luminosity data for both flames. For the forced cases, phase-locked time-averages were acquired. These images retain structural information about the soot distribution. The overall effects on the flame fields can be ascertained from spatially averaging or integrating the time-averaged image data.

The average images (averaged over 100-200 laser pulses) were taken with the camera accumulation mode (i.e., just the final accumulated image is saved) with an intensifier gate time of 50ns for each laser pulse. All averaged images for the forced flames were acquired phase-locked to the acoustic pressure, as measured by the piezo-electric pressure transducer; the uncertainty in the phase was less than 5°, which was caused by electronic drift and system unsteadiness. In each forcing cycle, image data were obtained at 13 phases for laminar flame case: from 0° to 180°, phase change is 22.5°, and from 180° to 360°, phase change is 45°. In transitional flame measurement, images are acquired at 16 discrete phases which were distributed evenly within a full forcing cycle.

5.2.1 Laminar Flame Images

When the burner was operated under laminar conditions, the corresponding jet Reynold number (based on fuel jet diameter) is 133. The surrounding (air) freestream velocity is 0.7 m/s. In this experiment, the driving frequency was 320 Hz. The acoustic forcing amplitude was chosen to achieve the strongest forcing effect that does not blow off the flame. At this forcing, the soot inside the burner exhaust appeared to be decreased noticeably.

Figure 5-2 shows three example LII images: the unforced flame, and the forced flame at two phases. It is not surprising to observe a significant difference of flame structures between forced and unforced flame. The forced flame images also show differences between different acoustic phases. In Figure 5-2, all of the images are displayed with the same color scale of soot concentration.

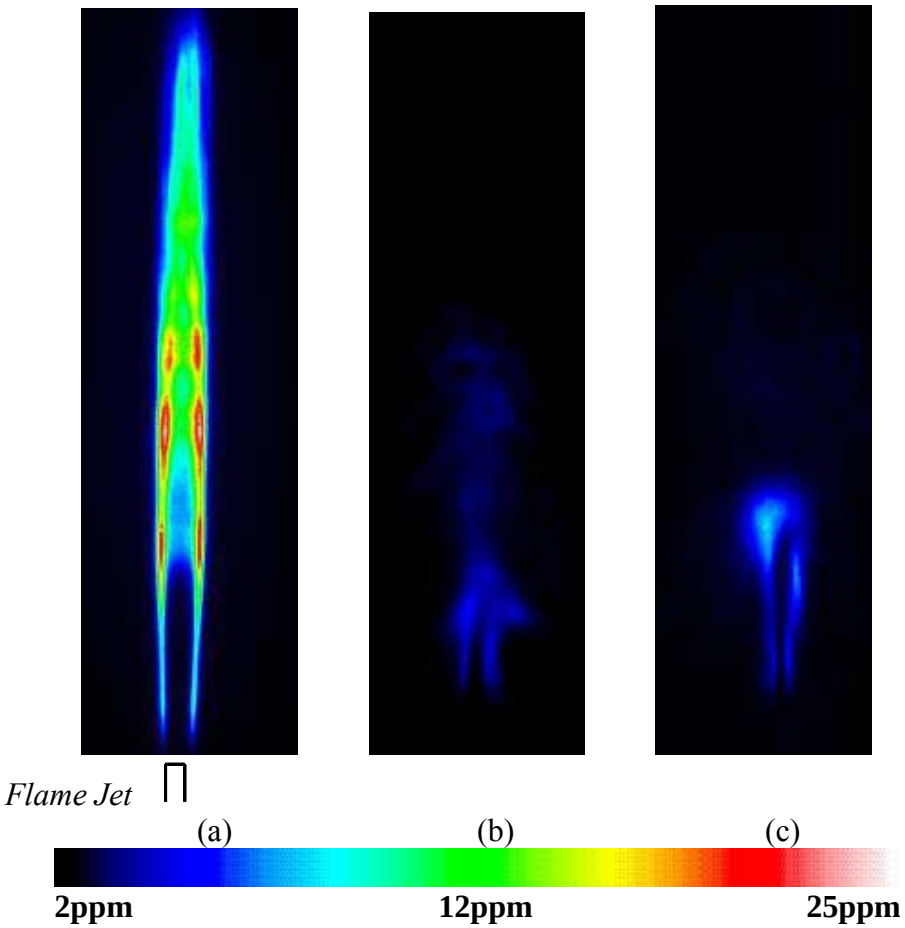

Figure 5-2. Averaged LII images (100 frames, 42×14.3mm) in a) unforced flame, and b) 225° and c) 270° relative to the acoustic pressure for the forced flame with 50ns gates, laser energy of 0.75 J/cm^2 and 0.5 ND filter in front of camera (the color mapping for soot volume fraction is also shown). Jet exit is 1mm below the image, as shown in (a).

As shown in Figure 5-2(a), the unforced flame has a gradual change in soot concentration along the flame height along the flame edges. The flame has the typical laminar flame structure: there is a visible sooty formation zone near the flame front, and less soot inside the flame surface from decreased pyrolysis. There is also low soot concentration zone close to the jet exit, where cold fuel has not had sufficient residence time or heating to produce much soot. With acoustic forcing, Figure 5-2 (b),(c), the overall height of the average sooty region decreases in length. In addition, the flame in the lower portion of the burner becomes broader (the sooty region diameter increases).

Furthermore, the peak (average) soot concentration is decreased with forcing. Finally, the region close to the jet exit is relatively "clean". The jet exit region has low temperature because of the cooling of cold fuel flow, and thereby less pyrolysis. Now, considering the forced and unforced flame situation, the acoustic forcing can generate flow fluctuation, in both azimuthal and radial direction, this flow unsteadiness can "bend" the smooth laminar flame surface (cone-like shape) and produce many curvatures, folders, thus volumetric chemical reaction can be intensified. Finally, the faster fuel consumption shortens flame height after acoustic forcing.

5.2.2 Transitional Flame Images

Upon increasing the fuel flowrate of the jet, the flame height increases and the flame flowfield gradually changes to an unsteady or turbulent-like condition. In this research, due to limitations of the experimental apparatus, the maximum measured fuel flowrate was fixed at 10.5 cm^3/s, with a corresponding jet Reynold number of 833. The surrounding air flowrate was the same as for the laminar flame case (0.7 m/s). In this condition, the flow field is not fully turbulent; though the unsteadiness of the flame is obvious. The flame length is much larger than the laminar flame, because of the much higher fuel flowrate (~6 times). Due to the large height of this flame and the smaller extent of the imaging laser sheet, the complete burner had to be shifted to three different heights in order to picture the complete soot flowfield. Each shift changed the burner height by 40mm and was achieved by adjusting the height of the acoustic burner, while the optical systems were untouched.

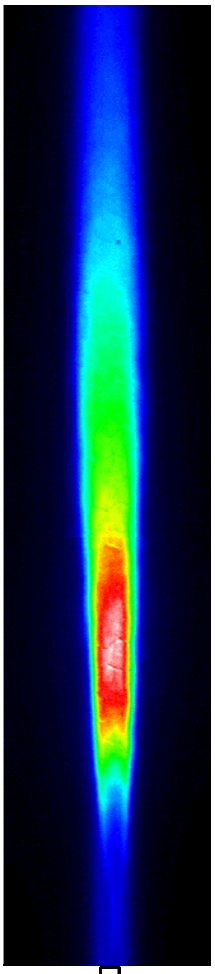

Figure.5-3. Unforced, averaged (200 frames) LII image (146x31 mm). Same color scaling as Figure 5-4.

Figure.5-3 shows a 200-shot averaged, unforced transitional flame soot image. The soot field is noticeably different from the unforced laminar flame. The highly concentrated soot region (on average) is no longer along the flame edges; instead, it is found in the central region of the flame. Similar to the laminar flame, the soot concentration is very low close to the jet exit and gradually increases to its peak downstream (at ~ 49 mm height above the burner, HAB), before decreasing for higher heights. This is similar to the soot growth and oxidation behavior of the laminar diffusion flame. The soot peak concentration varied with flame height and was very similar in both

laminar and unsteady flames Due to the limited optical access, this composite image does not include the region above the flame tip where the soot is further reduced by dilution and oxidation.

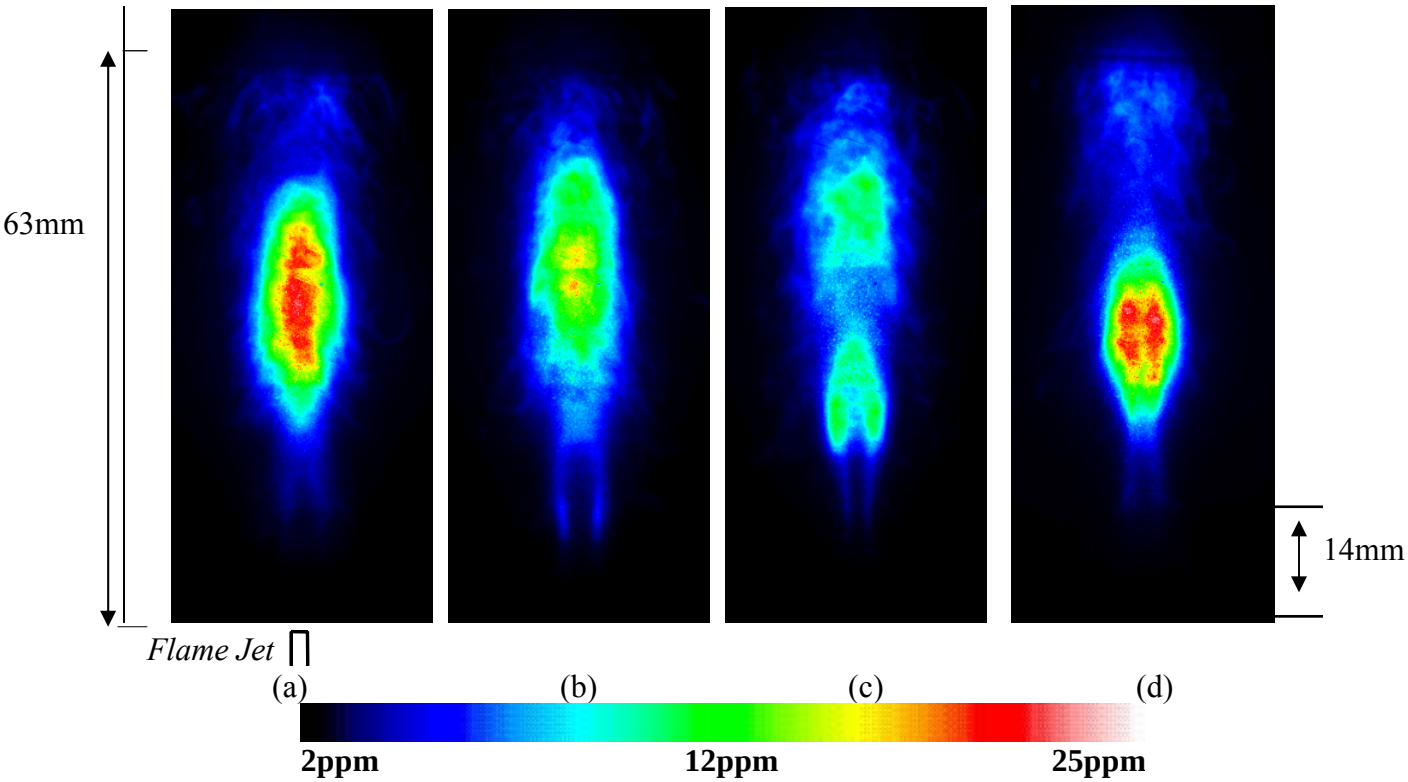

Figure 5-4. Time-average soot concentration images (100 frames, 77×33.2mm) at four phases: a) 0°, b) 96°, c) 168° and d) 262°, with signal gated for 50ns and laser energy 0.75J/cm^2 laser sheet 65mm height (no filter).

Similar to the forced laminar flame, acoustic forcing decreased the size of the transitional flame; the soot height reduces to around one-third of its original size, while the diameter is increased simultaneously. In other words, the forced flame shortens and widens; these effects can be seen in Figure 5-4 (note, the same color scale for soot concentration is used in the unforced and forced flames).

Close to the jet exit (located at the bottom of Figure 5-4), a diffusion flame-like region clearly shows up. There is some soot around what appears to be a flame edge close to the jet exit, while almost no soot is found in the "core". Also, very little soot is

apparent below 14 mm HAB. With increasing height, the soot concentration increases. However, compared to the unforced transitional flame, the size of soot region with relatively high concentration (red) decreases under acoustic forcing. The changes in the soot field between four driving phases are shown in Figure 5-4. At 0° (where acoustic pressure is 0, i.e. lowest absolute value), the peak soot region is a large oval shape and vertically centered in the image. At 96°, the peak averaged soot concentration has decreased from ~20 ppm (red) to ~15 ppm (green), and it moves vertically upward. At 196°, the peak concentration is broken into two regions, centered above and below the previous location and with a value (~12 ppm) slightly lower than at 96°. At 262°, the two peak soot regions appear to move downstream, with the upper region dropping in concentration, while the lower region grows in concentration and forms into the oval shape seen at 0° (though smaller). Based on the images of Figure 5.3 and Figure 5-4 for the transitional flame, acoustic forcing apparently does not reduce the peak (average) soot concentration in each phase as much it does in the laminar flame. Overall, the high soot concentration range in the forced flame is also closer to the jet exit compared to the unforced flame.

From the average soot concentration fields, it is clear that acoustic forcing can effectively reduce the total (two-dimensional) soot-containing area. In the following sections, quantitative global measures of soot in the flames are described.

5.2.3 Integrated (Total) Flame Soot

Because the time-averaging process also effectively produces some spatial averaging in an unsteady flame, it is most reasonable to use the average soot fields to find

spatially integrated information on the soot level. This global parameter can also be easily compared at different acoustic phases.

In order to integrate to find the total soot mass inside a flame based on the acquired data, some assumptions have to be made. The LII-based soot fields are only two-dimensional; they represent information from the thin planar region demarked by the pulsed laser sheet. Due to experimental limits, it is impractical to acquire soot information from the complete burner volume. In the previous figures, all the time-averaged, LII-based soot fields exhibit nearly symmetric structure, especially in the transitional flame images, with the laser passing through the axis. Therefore, it is reasonable to assume that, the averaged flame soot structure is axisymmetric. Thus, the total soot concentration can be calculated by cylindrical integration of the measured fields. In a data reduction process, background noises also need to be considered, which are based on background images. In experiments, the averaged background images were acquired in each corresponding phase, with exactly same setup as LII data acquisition but no laser beam.

Based on this assumption, the total soot inside the flame, M_{soot}, can be calculated from:

(Eq. 5-1) $$M_{soot} = \int_0^R \int_0^H 2\pi r \rho_{soot} \, dr dz$$

where ρ_{soot} is the mass density of soot at (r,z), r is the radial location and z is the axial location. ρ_{soot} can be calculated from below

(Eq. 5-2) $$\rho_{soot} = f_v * \rho_{carbon}$$

where ρ_{carbon} is carbon mass density and f_v is local soot volume fraction (~*ppm*).

The total soot mass in the forced laminar flame, as calculated from equation 5.1, is displayed on Figure 5-5 over one full acoustic cycle (*period=1/320Hz=3.125 ms*). Also shown for comparison, is the corresponding acoustic pressure variation. The total soot mass clearly varies over the cycle; however there is almost no change from 210° - 360°, but for 90-180° the total soot mass is considerably lower (~25% less) compared to the other phases. This reduced soot mass corresponds to the portion of the acoustic cycle when the acoustic pressure goes from its minimum to zero, i.e., when the acoustic velocity is approximately zero and changing direction from downward to upward (at 90°), then accelerates towards its maximum upward value at 180°. Overall, the forced laminar flames have total mass of soot between 8 and 12 μg. This is considerably less than the unforced flame, which has a soot mass of 54.5μg. So, the total mass of soot inside this flame is reduced by roughly five times due to acoustic forcing

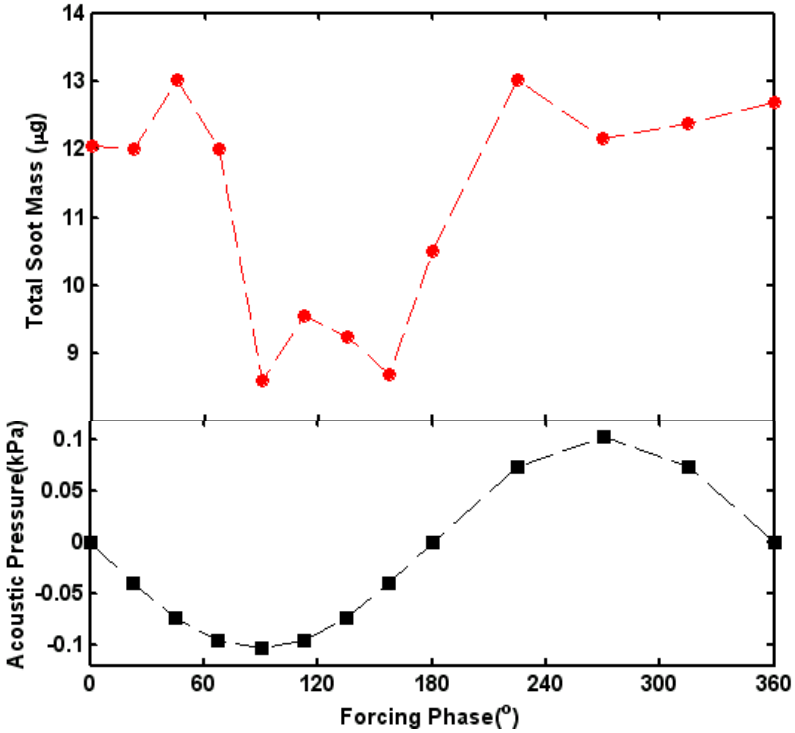

Figure 5-5. Total soot mass inside forced laminar flame over a forcing cycle (fuel flowrate 1.67 cm^3/s, middle of flame located 75mm above pressure minimum). Unforced flame soot mass is 54.5μg.

Inside the transitional flame, the total soot mass is calculated by the same method and is shown in Figure 5-6. Similar to the forced laminar flame, the forced transitional flame total soot also varies with acoustic phase. The total soot reaches its minimum slightly later, around 150-210°, where the acoustic velocity is approaching its maximum upwards value. This similarity with the laminar flame suggests some preference for the phases where the acoustic velocity is upwards (and large). Overall, the total soot mass inside the forced transitional flame is 15-21 μg, which is roughly twice the soot in the laminar forced case, even though the fuel flow rate is 6.5 times higher than in the laminar case. Also, the unforced transitional flame has 57 μg of soot; so forcing lowers the soot by a factor of ~2.9. Thus forcing is less effective for the transitional flame compared to the laminar flame. This reduced effectiveness can be caused by two reasons. First, the

unsteady nature of the transitional flame may already provide some of the impact of forcing, For example, it could cause the fuel and air to be partially premixed, whereas almost no premixing occurs in the unforced laminar flame. Second, the peak acoustic forcing velocity (estimated to be 0.74 m/s at 300 K) used for the transitional flame is only two times higher than for the laminar flame forcing (0.36m/s), while the fuel flow rate was increased by a factor of 6. Thus the ratio of the acoustic velocity to jet velocity is lower for the transitional case. While higher acoustic velocities were attempted, they extinguished the flame. If the acoustic forcing power was too high, the high velocity fluctuations entrained large amounts of cold air, which could dilute and cool down the fuel/air mixture, extinguishing the flame.

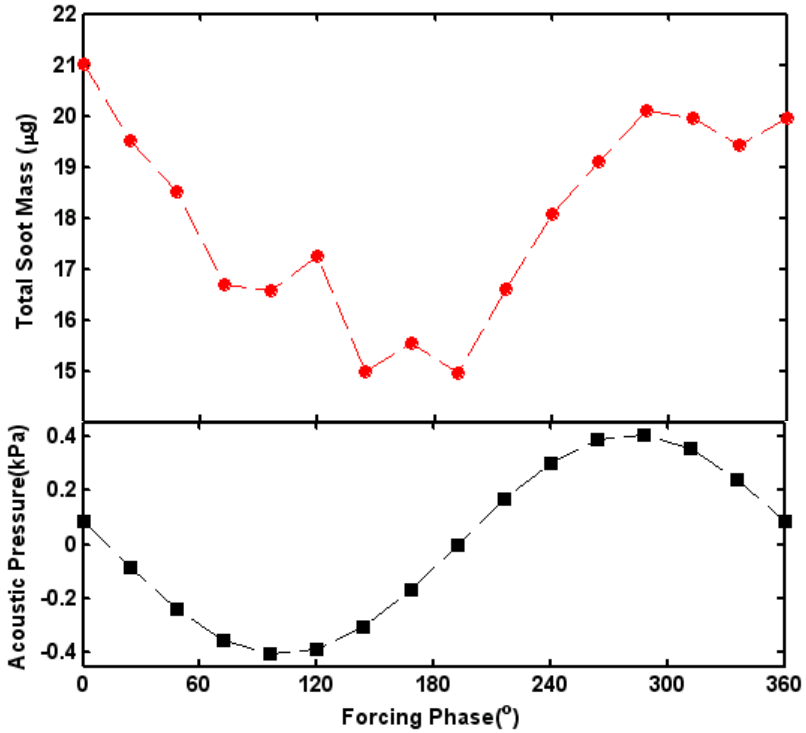

Figure 5-6. Total soot mass for transitional flame over an acoustic cycle (fuel flowrate 10.5 cm^3/s, middle of flame located 75 mm above pressure minimum). Unforced flame soot mass is 55 μg.

5.2.4 Averaged Luminosity Images

To better understand soot production and destruction in these flames, other information besides soot concentration would be helpful. Since soot radiation dominates the total flame luminosity in these highly sooting flames, the flame luminosity provides an added piece of information. Specifically, the amount of soot radiation depends on various properties, primarily varying with soot concentration (linearly) and soot temperature (to some high power, e.g., T^n with n>4). Therefore, the natural luminosity was also acquired with the same detection system used for LII but without the laser (as described in Chapter 3). Luminosity signals were recorded as broadband detection (primarily visible wavelengths). The blue and red signals were obtained using blue and red bandpass filters; the broadband measurements employed a neutral density.

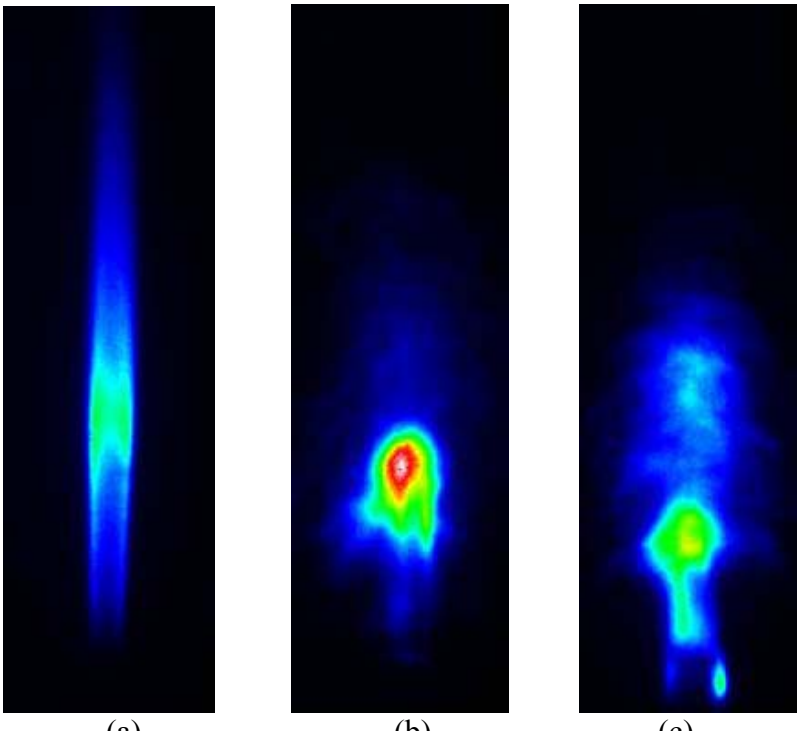

(a) (b) (c)

Figure.5-7. Time-averaged (100 frames, 45×14.3mm) broadband laminar flame luminosity images: a) unforced flame, and forced flames at b) 225^o and c) 270°. All signal gated at 500 ns with ND 0.5 filter and no laser.

Figure.5-7 displays averaged (over 100 laser shots) broadband luminosity images of the forced and unforced laminar flames. The radiation for the forced case shows the same flame shortening and broadening seen in the LII measurements, and the averaged flame structures are again vary with acoustic phase. This is also true for the transitional flame cases (Figure 5-8, (a) compiled from multiple images at different heights, (b) and (c) are standard images). From the images, the forced laminar flames achieve higher maximum soot radiation levels than the unforced flame. For the transitional flames, however, the behavior is different; the peak radiation values are similar (though slightly lower) with forcing, and the size of peak radiation region is decreased.

To further study these cases, the luminosity images data sets can be spatially integrated. Unlike the two-dimensional LII measurements, the luminosity images include radiation from the whole depth of the flame. Thus they already are integrated over one spatial dimension. Thus the total luminosity can be calculated by directly integrating (summarizing) all the pixel intensities in a luminosity image (after background correction).

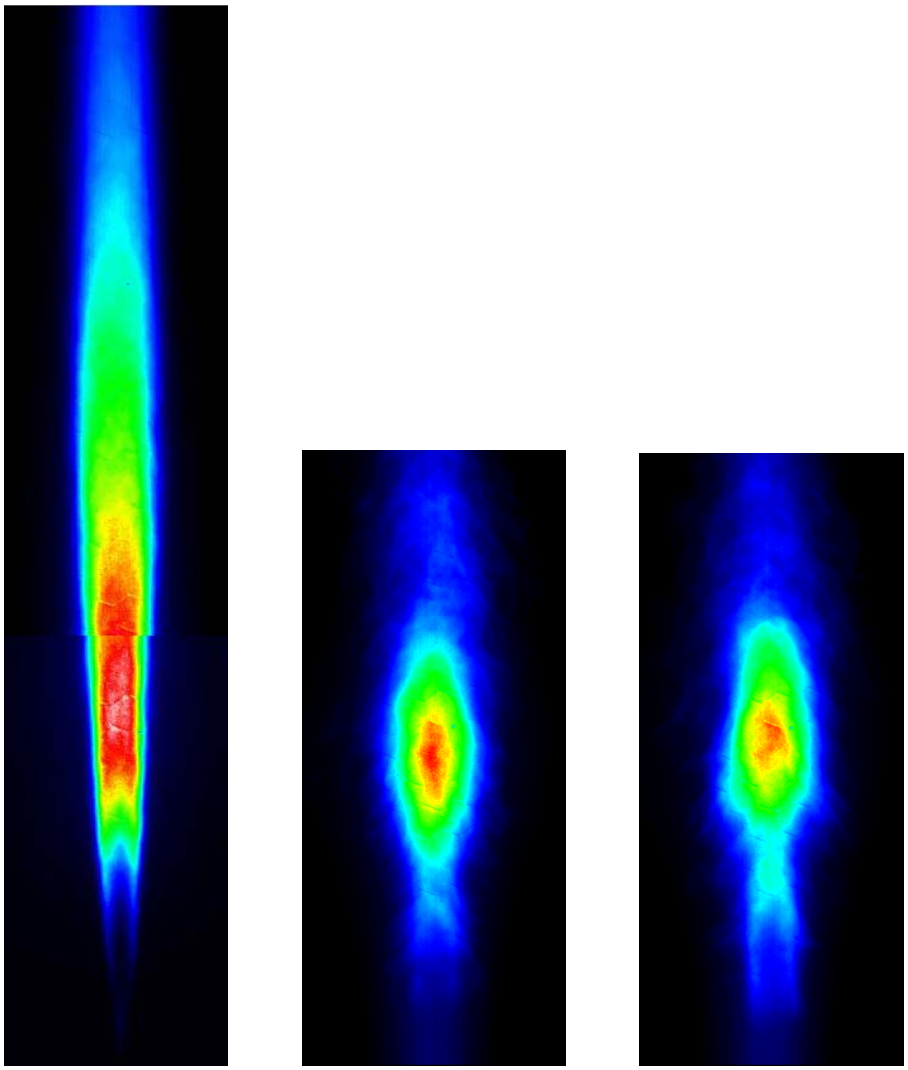

(a) (b) (c)

Figure 5-8. Time-averaged broadband luminosity for (a) unforced transitional flame. Stitched image.200 frames (127×27mm) and forced transitional flame at (b) 0^o (c) 72^o (0.5 ND filter). (200 frames, 77×32mm)

Figure.5-9 shows the spatially and temporally averaged broadband signal for both the laminar and transitional forced flames. Clearly the luminosity varies with phase in both flames, but they have very different trends across the forcing cycle. In the laminar flame case, the variation of broadband luminosity over phase is within 15% of the phase-averaged signal; thus it is not as sensitive as the total soot mass with respect to acoustic phase. Around 120-240º, the broadband signal is higher than at other phases. Since this

corresponds to the phases of lowest soot mass (Figure 5-5), it suggests the soot is getting hotter during these times (where the velocity is also reaching its maximum upwards speeds).

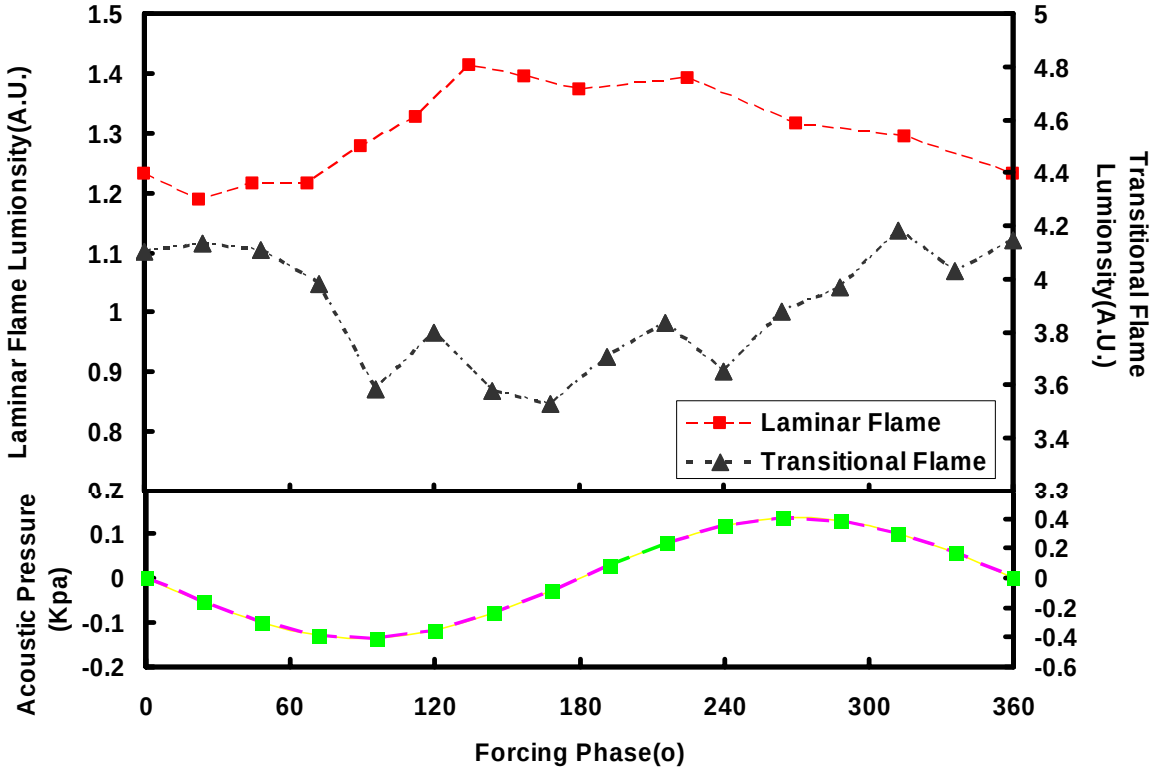

Figure.5-9 (Top) Volume-integrated luminosity for the forced laminar and transitional flames over a forcing cycle (these two data groups used two different cameras); (bottom) corresponding acoustic pressure. Unforced laminar and transitional luminosity signals are 0.55 and 9.23 respectively.

In the transitional flame, the broadband luminosity also varies with forcing phase, and the variation is within 13% of the phase-averaged signal. Unlike the laminar case, the total luminosity is lowest at the intermediate phases (90-240º). From the transitional soot mass plots (Figure 5-6), it was found that the soot mass was lowest at the center of these phases (160-190º). So for the transitional flame, phases with low total soot correspond to low total luminosity. However the minimum soot is 29% less than the peak value; while at the same phase, the total soot luminosity is only 15% less than its peak value. This

suggests a unit mass of soot still produces a higher luminosity for 160-190º. In this sense, the results are similar to the laminar flame case. Results for both flames suggest an increase in soot temperature at these phases.

Generally, the averaged LII measurements show acoustic forcing can decrease soot inside the flames, while the averaged luminosity data suggest averaged soot temperatures increase (in some phases) after acoustic forcing. However, all those averaged images can not show by what mechanism soot is decreased during acoustic forcing; i.e. how does the acoustically forced flow field help increase the oxidation rate or decrease the pyrolysis/formation rate. The soot structure variation, with time and space, is smoothed by the averaging process. So, it is necessary to examine instantaneous images, which contain information of what exactly happens inside the flame due to acoustic forcing.

5.3 INSTANTANEOUS FLAME IMAGES

In the following, instantaneous soot concentration (LII) and radiation (luminosity) results are presented for both laminar and transitional flames, and at unforced and forced conditions. The instantaneous flame images present the detailed topography of soot structure in the flames.

5.3.1 Laminar Flame

Figure 5-10 shows instantaneous laminar flame images. Similar to the time-averaged image (Figure 5-2 (a)), Figure 5-10(a) displays the unforced laminar soot field; it is smooth, showing the laminar flame is steady, and concentrated near the edge of the jet. Inside there is mostly fuel and the temperature is relatively low. Therefore, the

pyrolysis rate, and consequently the soot production rate, is low inside the fuel jet. Figure.5-11 shows the instantaneous soot concentration along a radial slice through the laminar acetylene flame at 20 and 30mm HAB. The lower peak value at 20mm HAB compared to 30mm suggests the soot is still growing along the flame edge, as expected for a laminar diffusion flame. Since it is hard to find a acetylene jet flame with exactly same properties (e.g. same fuel, coflow velocity and jet diameter), a low velocity (~0.1m/s at jet exit) jet flame data was used as reference, as shown in Figure.5-12. It displays a laminar flame soot volume fraction contour, the lowest HAB has readable soot volume fraction data is close to 8mm, where soot fraction peak is ~40ppm. Considering the 0.1m/s jet velocity, it takes ~ 80ms to reach 8mm after fuel leaving jet exit. In our laminar flame case, fuel jet exit velocity is ~12m/s, nearly 120 times faster than that reported in Figure.5-12, it will take much less time for our jet flow to reach 20mm and 30mm HAB. Thus, the peak soot fraction shown in Figure.5-11 (a) ~35ppm and (b) ~22 ppm are reasonable.

As shown in Figure 5-10(b) (c) for acoustic forcing, the original long laminar soot region disappears; instead, the sooty region is broken into multiple, smaller pieces. Similar to what was seen in the averaged soot images for the forced laminar flames, the instantaneous soot fields are located closer to the jet exit, with a broader area (larger diameter) than the unforced flame. These soot regions have more highly curved structure, which is hardly found in unforced laminar flame.

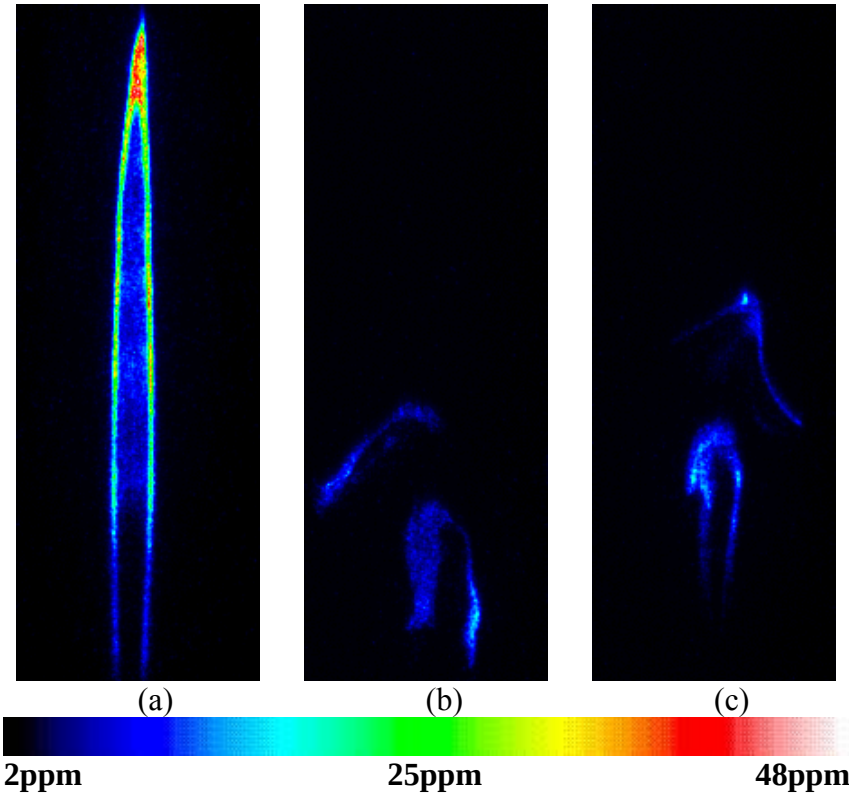

Figure 5-10. Instantaneous soot concentration fields (45×18.3mm) for the laminar a) unforced flame, and forced flame at phase angles of b) 225° and c) 270° (50ns gate, 0.75 J/cm^2, ND 0.5 filter). The unforced laminar flame is ~ 43mm tall.

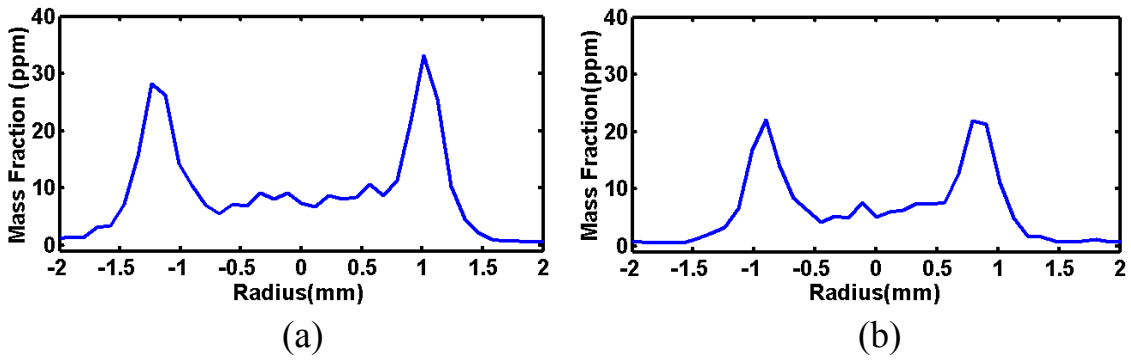

Figure.5-11. Radial soot fraction profile for the unforced laminar flame (Figure 5-10) at two heights: (a) 30mm and (b) 20mm HAB.

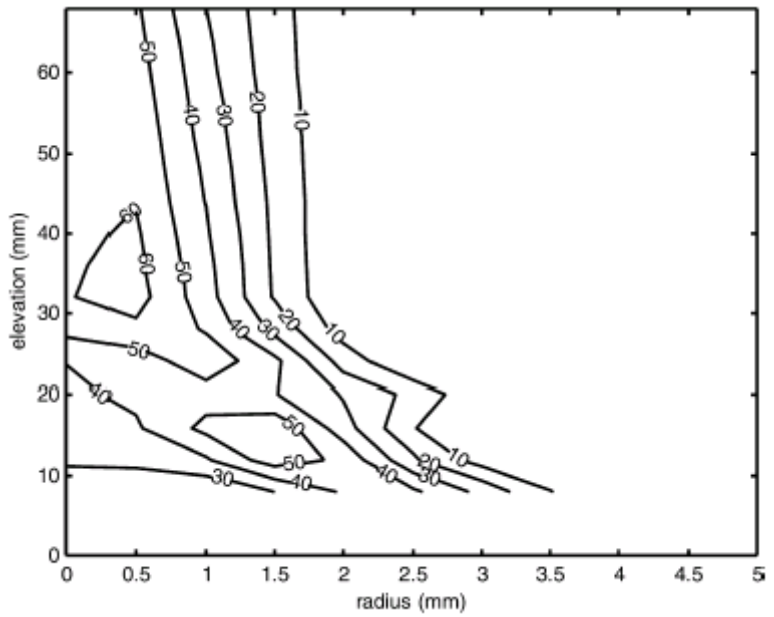

Figure.5-12. Soot volume fraction (ppm) contour plots for a steady acetylene diffusion flames.[82]

5.3.2 Transitional Flame

Since the unsteady transitional flame (unforced and forced) has a structure that is closer to that found in a number of basic industrial combustion systems, this section includes more detailed analysis of the instantaneous soot field than the previous section on the laminar flame.

Transitional Flame LII Soot Concentration Measurement

As shown in Figure 5-13, the soot field for the unforced transitional flame is much different than the laminar results. It has a much more complicated structure, even without acoustic forcing. The soot regions are more irregular; many roll up, vortex-like, structures are clearly evident. Unlike the laminar flame, where a soot-free fuel region can exist along the centerline of the flame for some distance, the transitional flame only exhibits this behavior very close to the jet exit. Throughout most of the height, it seems

that air or hot products can “penetrate” into the fuel jet, and soot can be produced almost anywhere along the jet. This irregular structure for the transitional flame is due to the larger shear force generated at the fuel jet boundary. At the higher Re of this flame, this induces vortices that can grow, entraining ambient air into the fuel.

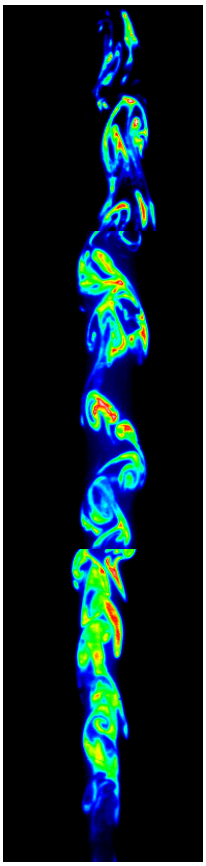

Figure 5-13. Unforced transitional flame instantaneous soot field. Stitched image from two raw images at different heights, the color scale is same as that in Figure 5-14 (141×26 mm).

With acoustic forcing, especially for the high amplitude forcing close to the flame extinction limit the vortex generation appears to get stronger and the sooty region is “squeezed” closer to the fuel jet. This can be seen by comparing Figure 5-14 (a) (unforced) and Figure 5-14 (c) (forced). Figure 5-14(b) and (d) repeat (a) and (c), but are clipped to show only soot concentrations higher than 18ppm. Obviously, the extent of the high concentration soot region is decreased sharply with acoustic forcing.

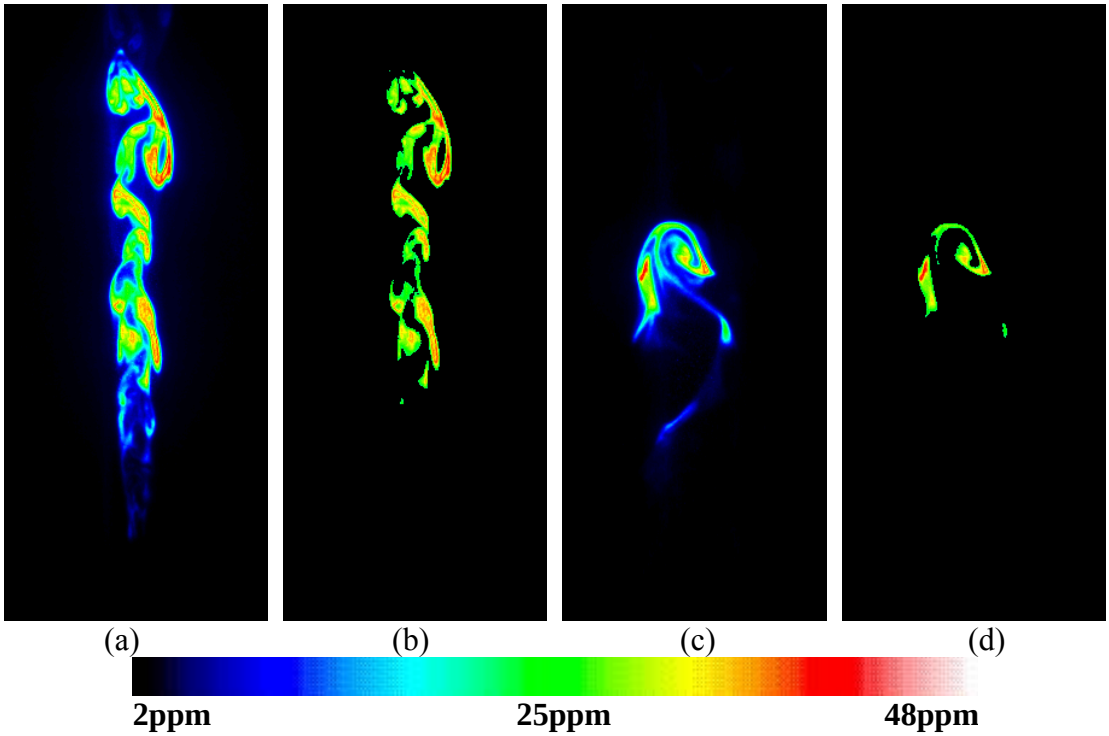

Figure 5-14 Instantaneous soot distributions (77×34 mm) for the transitional flame: (a) unforced with soot shown for the full range (2-48ppm), (b) unforced and clipped to show soot only for 18-48ppm, (c) forced at 72º (2-48ppm), and (d) forced at 72° (18-48ppm).

It is noticed, the peak soot concentrations in the instantaneous laminar flame images are about twice of the value found in the time-averaged images. The flame's soot field moves around sufficiently, even for the nominally laminar flame, that some spatial smoothing occurs.

Figure 5-15 and Figure.5-16 display the forced transitional flame images at 16 data acquisition phases; these images show how the soot structures vary with phase relative to the acoustic forcing. While there are shot-to-shot variations even for a fixed phase, the images shown were chosen as representative of what occurs at each phase. Similar to the forced laminar flames, the forced transitional flame soot field becomes smaller and more compact than the unforced case. Based on the shape and structure of the

soot region, these 16 images are separated to five groups, 0°(or 360 °), 24–120°, 144–216°, 240–288° and 312–360°.

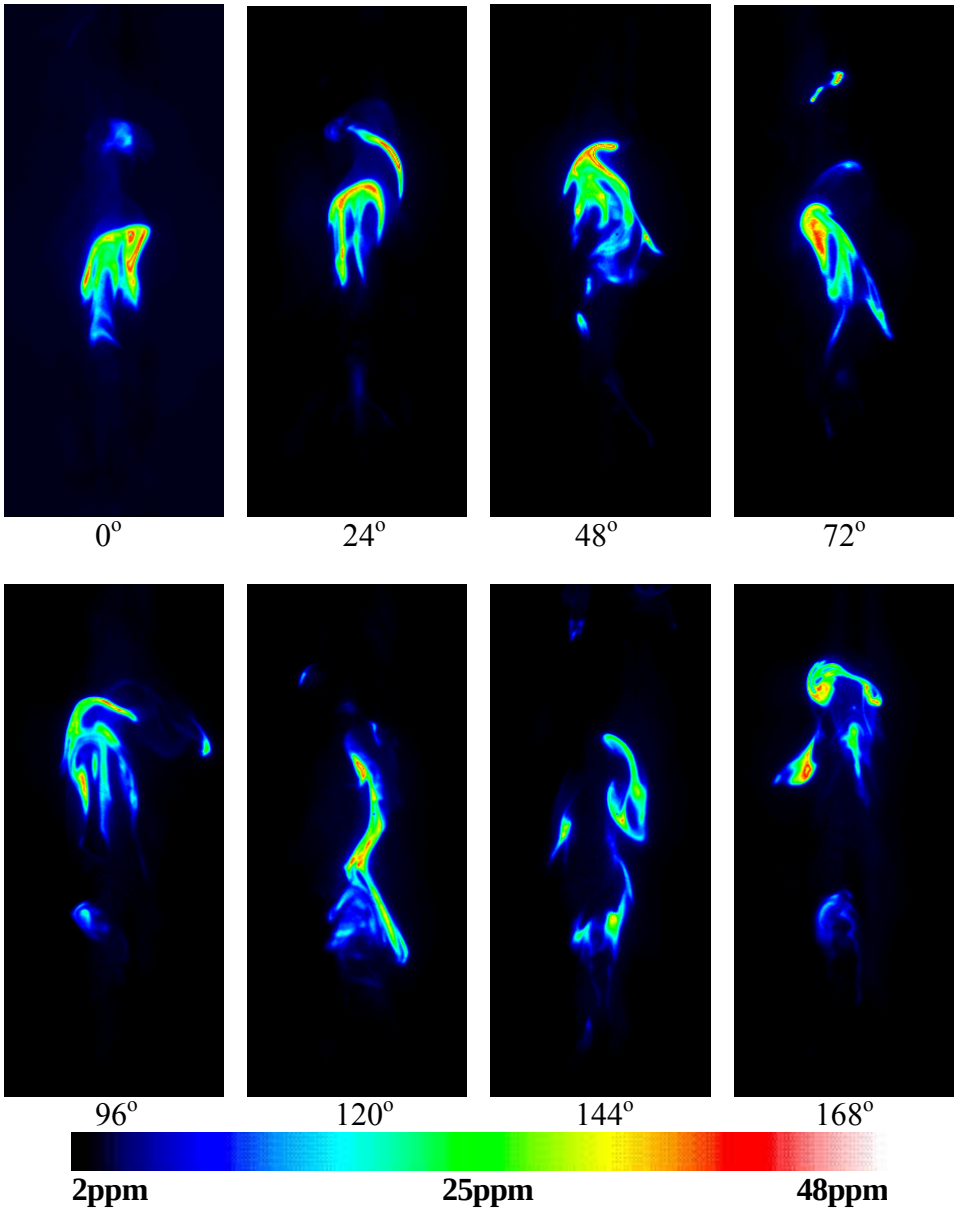

Figure 5-15. Instantaneous transitional flame soot concentration fields (77×34mm) at eight phases throughout the first-half of a forcing cycle.

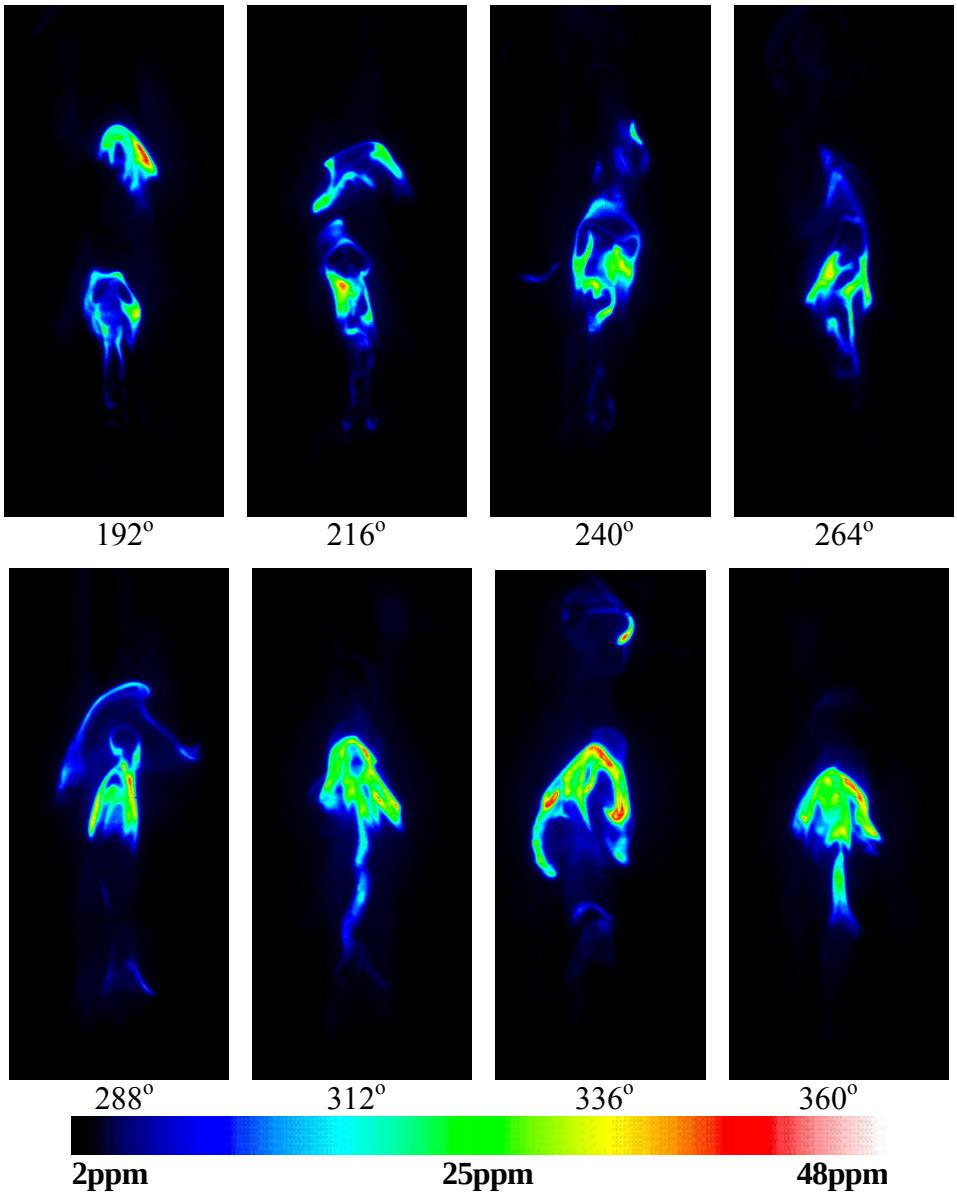

Figure.5-16. Instantaneous transitional flame soot concentration fields (77×34mm) at eight phases throughout the second-half of a forcing cycle.

At 0°, almost all the soot is contained in a single compact region, with a bulb-like shape, and concentration is high. From 24° to 120°, the soot is still primarily confined to one structure, which resembles by a roll-up and filament shape. The curved and branching structure exists in almost every image. In addition, the images for 24-120° show a soot region that is "stretched" in the axial direction compared to 0°. More importantly, images at 24°, 72° and 96° show a smaller soot structure than at 0°, and they

have a higher soot concentration that sits along the edge. Next at 144-216°, the soot region becomes "stretched out"; the soot also exists in more than one region, with each having a clear curvature or roll up structure. Around 168° and 192°, the stretching reaches its maximum; the average distance between the centers of the two separate soot regions is ~35mm. At 240-288°, the soot regions seem to distribute in a smaller area than previous phases, with some fine curvature and filaments. Now however, it seems that the two consecutive vortices are closer. This is similar to what is seen for 24-120°, where separated soot regions are not very further away. From 312° to 360°, the soot region seems "squeezed" to one region again, similar as 0º case.

To further examine the variation of the soot structure during forcing, additional images were selected at 0^o, 96^o, 168^o and 264^o, as displayed in Figure 5-17 and Figure 5-18. These phase angles were chosen based on the observations above, and the averaged findings (Figure 5-6), where the total soot is maximized at 0°/360°, has a medium value at 96^o and 264°, and has a minimum at 168°.

At 0^o, the flame soot again can be seen to exist mostly in one region with high concentration (dark regions in the images). Images a-d all show only one rollup vortex structure with a central filament/tail. In these images, the rolling direction can be deduced (as shown by the arrow), these direction is most likely anti-clockwise (a, b and c), depends on local flow property. Image b and c have big thick high soot region, much thicker than that in laminar unforced flame soot Figure 5-10. All four images show the highest soot concentration at the "head"/top of the vortex structure. Besides, all of these vortices structures are composed of multiple thin filament structure, especially in image a, c.

At 96^{o}, all images (e, f g, and h) show high soot concentration region becomes smaller and thinner, no big high soot concentration region appears as that in image b and c, the vortex structure become even finer, the vortex rolling direction can easily figure out, as depicted by arrows. Soot region with peak concentration (dark) are clearly show up at the "head" of vortex (image f, g and h). Most important, beside big main vortex soot region, there is second soot structure shown up upstream on each image (image f, g and h clearly shows two separated soot flow region, image e seems has two flow soot region, but they are very close), but all second soot regions have lower soot intensity than the big vortices. It may suggest the initial soot producing step inside the second flow structure.

As to168º, it is corresponding to the lowest total soot parts in the average image data Figure 5-6, The separation of two soot regions is clearly displayed on each image, and both have similar soot intensity The measured averaged distance between centers of two structure is ~35mm. Based on PVV measurement in Chapter 4, the averaged flow velocity is ~13m/s, and each acoustic cycle is 3.125ms, therefore, this separated soot region most likely belong to the products of two consecutive cycle. In addition, it is noticed that the upstream structure soot intensity is higher than that in 96^{o}, and it shows noticeable unsteady effects: the soot forms "handsaw teeth" (image I, J and L) structure, at meantime, some initial vortex structure also can be found (J, K and L). The downstream soot structures still very like a vortex or part of vortex structure, if take into account the 2-dimesional laser sheet can only catch one cross section of 3-dimensional vortex structure, so the LII image may only catch part of vortex where soot concentration is lower.

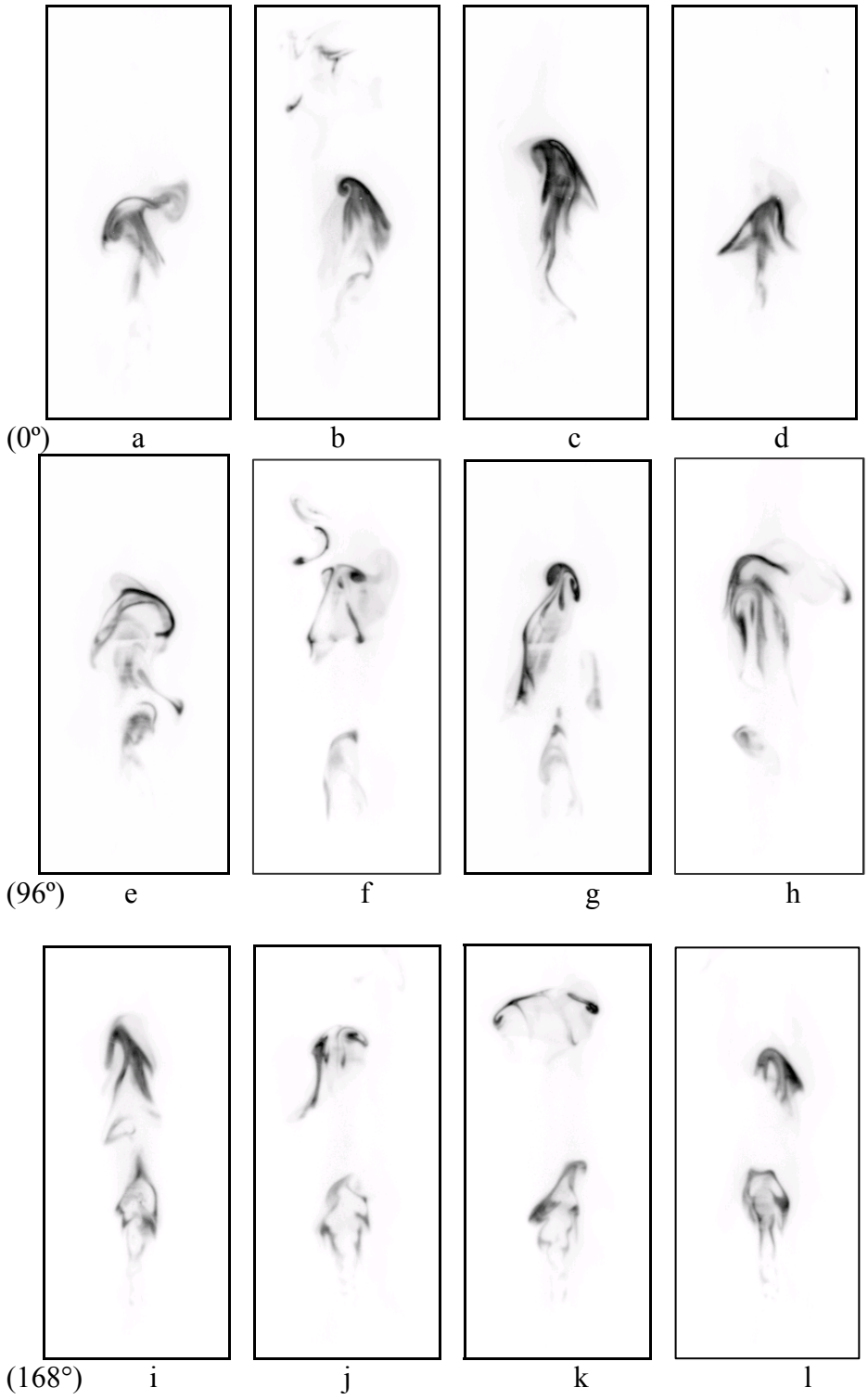

Figure 5-17. transitional flame during acoustic forcing at forcing phases 0^o, 96^o, 168^o(image size 77×34mm).

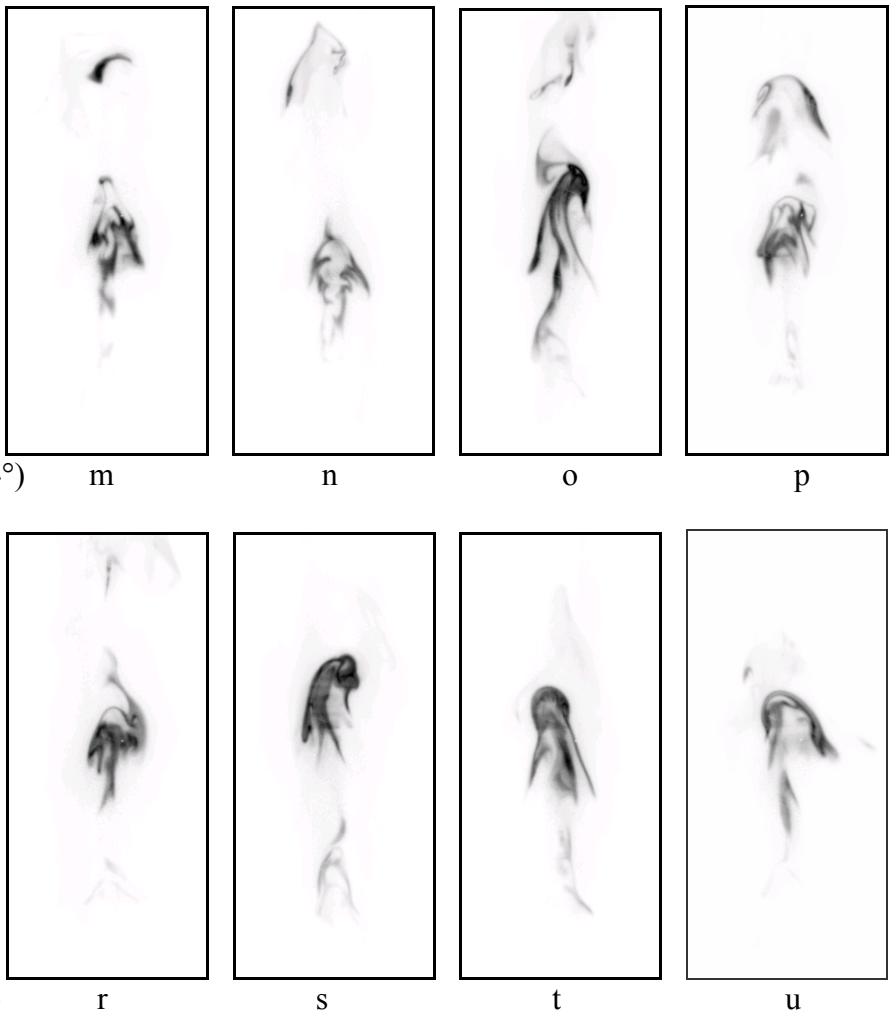

Figure 5-18. transitional flame during acoustic forcing at forcing phases 264°, 360°, (image size 77×34mm).

At 264º, no doubt to figure out 2 soot structures, the down stream soot structure is much less intense than 168º, some image (image p) can show the most part of vortex, but others (image m, n and o) show only small part of the vortex, this suggest the previous vortex either move away from the image sheet, or those soot structures were oxidized and dilute by ambient extra air and downstream products. Considering the low axial velocity (~1m/s from chapter 4), it is most unlikely for big vortex (~10mm) moving outside image laser sheet at 0.8ms (from 168º to 264º is close to ¼ of a forcing cycle), thus, the 2nd option is most reasonable explanation. Contrary to soot decreasing in downstream vortex,

the upstream soot structures increase their soot concentration noticeably, the previous unsteady effect in 196ºis getting stronger (image m and n), and those “handsaw teeth” can evolve to vortex structure (image m, o and p). Overall, soot inside upstream flow structure is dominated.

In the 360° images, the soot structure is almost same as 0° case, only one major soot vortex structure dominate the sooty region, with multiple filament structure. These multiple filament structure is most like formed from multiple layers of air and fuel flow. From above sections, it is easy to figure out, the acoustic generated rollup or vortices can wrap air and fuel, and form “sandwich structure”, high fuel and air gradient between these layers can drive fast mixing between them. This structure can generate multiple partial premixed flames. On the other hand, due to the turbulent flow property, the amount of air and fuel wrapped inside the multiple layer can be different at each layer and can be varied in different location of same layer, thus, the fuel/air ratio inside the “sandwich structure” can be varied correspondingly. Where fuel/air ratio is low can led to more complete oxidation of fuel and produces less soot. But at location where fuel is rich, the extra fuel can be pyrolyzed and produces more soot. Due to multiply-layer and thin flame effect, soot is closer to the flamefront and gain higher temperature.

At meantime, the high swirling velocity of the some vortices, especially at vortex head, can form a semi-insulator structure; therefore, the soot inside these structures can have a relative longer life time. In addition, it is also noticed there are some small parts of soot appear occasionally (image r and s), which most like belong to the previous downstream vortex (image r) or upstream soot structure (image s), but they are intensity is too low to effect the main soot structure.

Besides LII soot measurement, flame luminosity images have also acquired.

Transitional Flame Luminosity

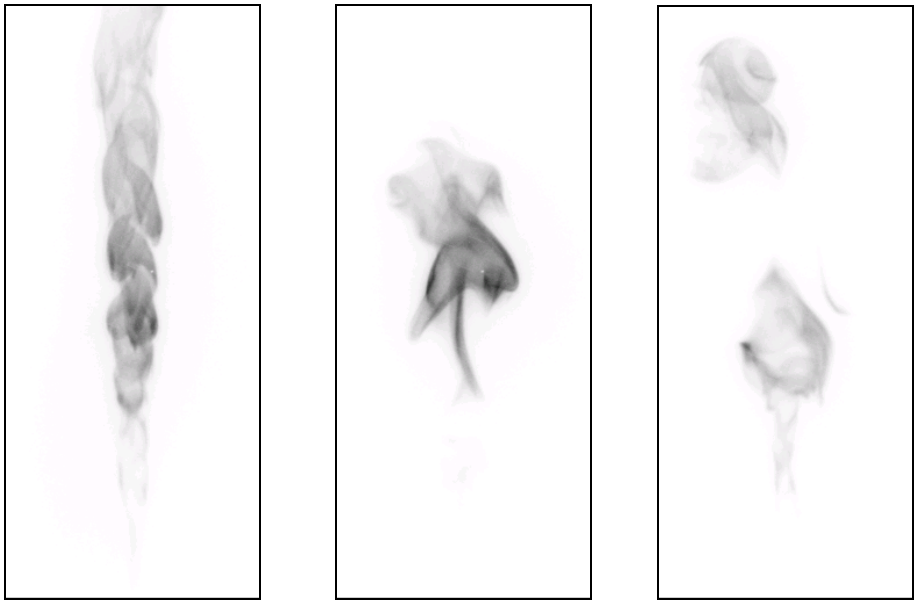

(a) (b) (c)

Figure 5-19. Luminosity transitional flame during acoustic forcing at 2 forcing phases (77×34mm) (a) Unforced flame (b)0^o (c)168^o. the color scale is uniform for all 3 images.

Flame luminosity is line-of-sight technique, which records the whole flame image at one direction. Strictly say, luminosity images can only provide 2 dimensional information of flow field. But, due to the transparence of air, these images also contain some information of overlapped flame structure at different depth of view, that is to say, these overlapped structures contain some 3-dimensional information of flowfield, at least, these luminosity images can be a reference for study 3-dimension flowfield, even they can not provide strictly 3-dimensional information. Figure 5-19.displays three luminosity images, unforced transitional flame (a), and forced transitional flame at two different phases in (b), (c). These luminosity images show general appearance of unsteady flame. The unforced flame (a) luminosity signal is almost continuously from some height above jet exit and extends outside the field of view, the signal intensity variation along the

flame is smooth. While the two forced flame luminosity images (b) (c) show the subtle rollup structure, which can be associated with turbulent flow structures, most likely, they are acoustically generated vortices. In Figure 5-19(b), it shows image at 0^o, it seems only one vortex which has high signal level. Part of it looks like mushroom or jelly fish shape with a long tail. This is constant with LII image in Figure.5-16. In Figure 5-19(c), the image was acquired at 196^o and clear shows that, there are two vortex structures which have been separated further apart, this is also constant with LII image in Figure.5-16. Generally, high luminosity signal is related to high radiate materials. Since soot particle sizes are much larger than that of ambient air molecule, they emit more visible light signals (luminosity) than ambient gas molecule, at same temperature, higher concentration soot can emit higher luminosity signal. In Figure 5-19 (b) (c) show most high signal region stays on the edge of vortices structure, and thinner than the unforced flame with similar signal level, which suggests high concentration soot is closer to the edge of vortices, where is closer to the high temperature flamefront.

The similarity of flame luminosity and flame LII images suggests LII images have caught most important flame soot structure information.

5.2.3 Interaction between vortex structure and soot formation

Based on previous LII and Luminosity studies in this chapter, the mechanism of flame soot production and acoustic forcing generated vortex interaction can be described as following: Around 0^o, fuel flow velocity reaches its maximum upwards during acoustic forcing, initial unsteady or vortex is generated from the jet lid due to the shear force on the fuel/air flow interface, so does the surrounding air flow. At this moment and this location, soot particle is not detectable because of low fuel/air flow temperature and

less pyrolysis. On the other hand, vortex produced two cycles before (6.25ms) can move ~72mm, which is outside field of view (63mm). Thus, the vortex-soot structure detected by camera was produced from previous cycle.

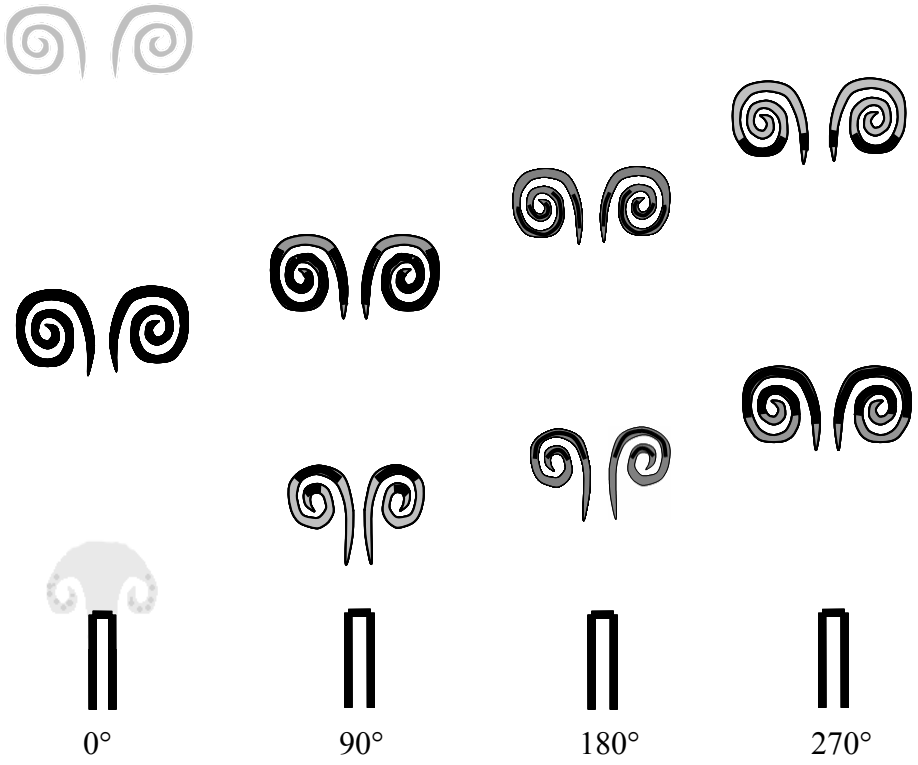

Figure 5-20. soot production and vortex interaction inside acoustic forced flame. black stands for high soot concentration, and dim gray stands for low soot concentration.

From 0º ~ 90º the acoustic pressure decrease from 0 to minimum (negative), at meantime, acoustic velocity decreases from maximum upwards (at 0º) to 0 (at 90º). Due to the small diameter of fuel jet (0.86mm i.d.), and high jet velocity, thus, it is difficult for pressure propagate downwards inside fuel jet, thereby fuel flow velocity at jet exit almost constant at jet exit, that is to say, the velocity difference between fuel and air will be increased during this period, so does the shear force. This increasing of shear force on fuel/air interface will lasted to 180º, where acoustic velocity decreases to its minimum, the shear force reach its maximum. After that, shear force decreases, until 360º. From 0º

to 90º, the new rollup or vortex can be growing with the continues supplying of energy by acoustic forcing; one the other hand, the "handsaw teeth" structure produced by shear forcing can be growing and merge to vortex structure with the continues providing energy through acoustic forcing. When this rollup or vortex structure is convected to downstream, the cold flow can be preheated by the hot products from downstream flow, some local temperature can be high enough to pyrolysis fuel rich area gradually, thus, a new rollup or vortex structure emerges some time (<0.5ms) after it emits from jet exit, the soot region grows with vortex moving further downstream, and soot vortex becomes noticeable. Due to short time period (<1ms), new structure soot concentration is still low. Thus, on the LII image of 90º, there are two soot structures; downstream one has higher soot concentration than upstream one. From 90º to 180^{o}, soot inside downstream vortex continues diluted or oxidized, while soot in new vortex is growing, at ~ 180º, the two vortex structures show similar peak soot concentration. These chemical reaction processes continue after 180º, while all soot structures can be convected further downstream. Around 270^{o}, inside upstream rollup or vortex structure, soot concentration can reaches higher level at those locates where fuel is richer; while downstream vortex soot concentration continues decrease through dilution or oxidization. At 360^{o} (0^{o} for new cycle), the remaining soot inside downstream vortex dies out from images either through further dilution and oxidization, or simply convected out of the sight of view; On the contrast, soot inside new vortex structure dominates the flowfield under camera view, where soot concentration almost reaches its maximum after developing in one cycle period.

In Kim's[83] and Ezekoye's[1] researches, they explored the mixing mechanism in acoustically excited diffusion acetylene flame, proposed partially premixing process inside jet exit during acoustic forcing, which led to less soot production. In their works, the peak acoustic velocity is higher than the mean velocity, so the total velocity could be negative at some phases. In our experiments, the jet main velocity is always higher than acoustic velocity, total velocity is always positive. On the other hand, in Kim's work, only velocities near jet exit were measured using hotwire methods; in Ezekoye's work, the soot fraction measurement was based on laser extinction technique, which contained no instantaneous spatial data. But, in our experiments, LII measurements provide spatial soot structures, which is much useful in understanding soot growing inside unsteady flow structures.

5.4 QUANTITATIVE ANALYSIS OF INSTANTANEOUS LII DATA

There are 20-50 individual frames for each flame condition (e.g. flowrate, forcing phase), and, in each frame, there are at least 200×400 pixels. Thus, there are millions of data points in each image data file (i.e. fixed condition). To handle this huge data set, statistical analysis methods are useful.

In these experiments, the Probability Distribution Function (PDF) is utilized to examine the overall soot field. At a certain soot mass fraction, the corresponding PDF value $P(f)$(1/ppm) represents the fraction of all the pixels that have soot mass fraction value between f and $f+\mathrm{d}f$, relative to the total number of pixels in a certain defined image region. That is to say, the PDF represents the distribution based on all the pixels in each image file (normally 50 frames in each file), and a spatial region of 200×400 pixels. Thus

there would typically be 4 million data points included in the PDF for each condition. To be properly normalized, the PDF function can be expressed as:

(Eq.5-3) $$\int_0^\infty P(f)df = 1$$

To calculate this continuous function from the large number of data points, it is useful to group the individual points into a fixed number of discrete *f* bins. First, the flame LII based soot concentrations were discretized to 251 levels; this chosen is to make the data set smaller and still have a high enough signal resolution. The bin width was 0.19ppm, and all pixels with concentration >48ppm were placed into the same group, since hardly any pixels reached that concentration. Then, after calculating the total number of pixels in each bin range, and comparing this to the total number data points in an image file, the probability density function within each bin can be acquired according to:

(Eq.5-4) $$P(f) = \frac{N(f_i)}{N_{tot}W}$$

Where $N(f_i)$ is total number of pixels in a certain bin i and N_{tot} is the total number of pixels in each image file (or defined region in the image), and W is the width of bin.

5.4.1 Flame Probability Distribution Functions (PDFs) data

Figure 5-21 shows the PDF's of the laminar flames, both unforced and acoustically forced for three phase angles, 0º, 72º and 144º. The phases were chosen based on the averaged image results (Figure 5-5), to highlight the typical soot concentration variations in a forcing cycle. In addition, the plot depicts the region of high soot concentrations, where the differences among the data sets are most noticeable.

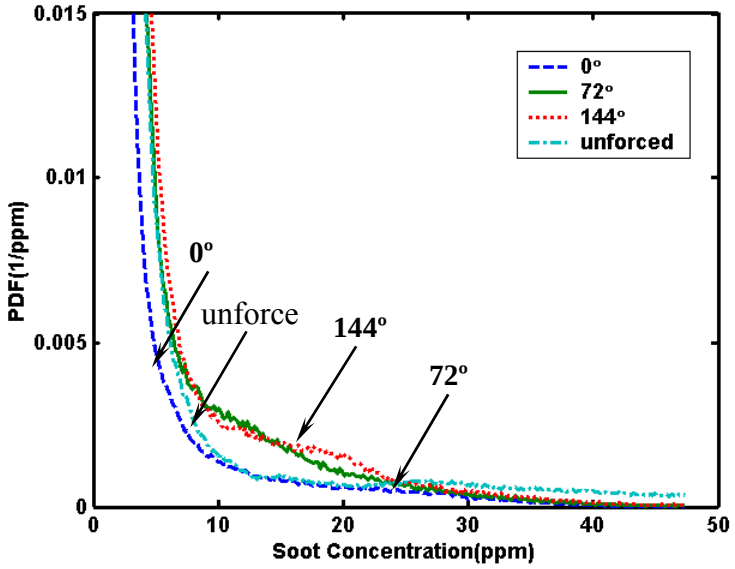

Figure 5-21. PDFs for un-acoustically excited laminar flame, and acoustic forced flame at acoustic phase 0º, 72º and144º.

Both the unforced and forced laminar flame images have a large region (number of pixels) with low soot levels, the PDF is weighted heavily toward low soot concentrations, rapidly dropping from 0 to 10ppm. Above 10ppm, the distribution gradually decreases. This corresponds to the images in Figure 5-10, in which the sooty region occupies only a small portion of the whole images. With acoustic forcing, the sooty area shrinks, and is located almost completely in the lower portion of the images. In addition, the unforced PDF has a large, nearly flat range, from 15ppm to approximately 70ppm. After acoustic forcing, the soot PDF decreases rapidly as the concentration exceeds 20ppm in the three phases. Also the region above 40ppm, which is noticeable in the unforced laminar PDF, almost totally disappears in the forced PDF. Among the forced laminar flame PDFs, 0º and 72º are also relatively flat at low soot concentration, from 10-20ppm, which has relatively more area than in the unforced flame. The 144º PDF has no flat section, it now declines rapidly for 10~20ppm. Actually, the 72º and 144º PDFs show very similar trends, especially in for soot concentrations below 4ppm. The 0º

results also exhibit a smaller PDF value at soot concentrations above 10ppm; this should be compensated by an increasing probability at low soot levels (in order to keep the integrated value at unity). This increase at low soot concentration is most likely for < 3ppm, which is close to the background value, i.e., the background represents a larger portion in this case. Essentially, the 10-20ppm region is most likely increased by forcing, dropping the high soot concentration region (>50ppm) of the flame to this low level. Because the background signal in the LII images influences the accuracy of the low concentration results, this suggests these PDFs are not fully comparable to all data set due to the size effect of soot region varying at different phases. Thus further study is need before drawing final conclusions.

Figure 5-22 shows unforced and forced flame PDFs (at three of the 16 recorded phases: 0º, 72º and 168º). Figure 5-22 (b) shows the same results as (a), but with a different vertical scaling, such that it provides more detail about the soot concentration distribution above 4ppm. There is clearly some difference in the forced PDFs, especially from 10 to 35ppm. Similar to the laminar flame results, the forced transitional flames has a large decline in both peak and low soot concentrations compared to the unforced case. All the transitional flame cases have peak soot levels that are much less than that of the unforced laminar flame. Its soot range is from 10 to 40ppm. The difference is that the soot concentration distribution in the unforced transitional flame is much higher (at least on a relative basis) than that of the forced cases for soot volume fractions above 4ppm, but it is similar for low volume fractions (<4ppm). This suggests that acoustic forcing is effective in reducing the areas of high soot concentration in the flame. Unlike the laminar case, all the PDFs for the different forcing phases are quite similar. There is, however, a

small variation at 15-35ppm. The largest drop in high (>20 ppm) soot concentrations occurs at 168º, which agrees with the overall drop in soot mass shown in Figure 5-6 for 90-180º.

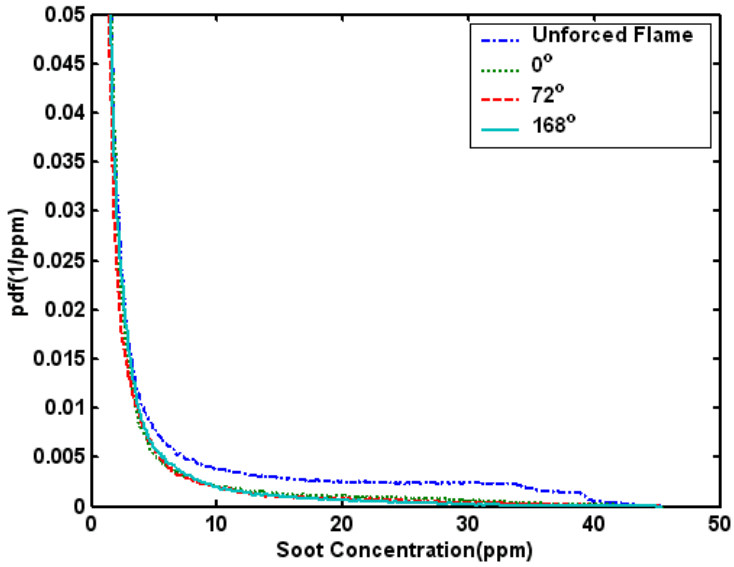

(a)

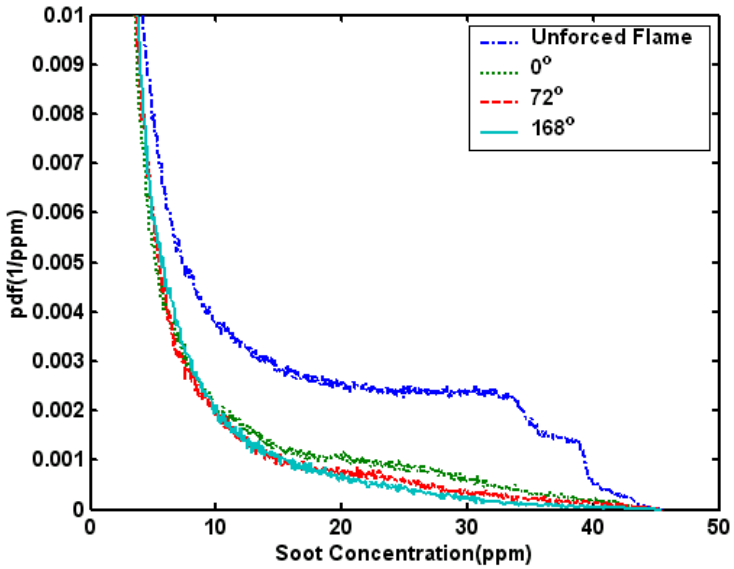

(b)

Figure 5-22. Probability densities of the unforced and forced transitional flames: (b) is expanded view of PDF in (a).

So, the probability distributions of soot concentration show that the forcing process is effective in reducing the regions of high soot concentration. For the laminar case, the high concentrations appear to shift to a medium range (10-25 ppm), while in the

higher flowrate case all concentrations above 10 ppm become less likely. The amount of reduction in soot does vary somewhat with phase relative to the forcing signal. There is some problem, however, regarding these PDFs. The unforced transitional flame covers a much longer region than the other cases (recall that three images at different heights are needed to capture it), while the forced transitional flames are ~1/3 the original height. Similarly the forced laminar flames are even smaller in extent. The statistics used to generate the PDFs above were based on all pixels in a region of interest (ROI), which is the full image in this chapter. This is important because the probability of finding a given soot concentration depends on the number of pixels in the ROI. A larger ROI with more dark pixels would lower the PDF at all levels (except zero). This is more problematic if regions without soot do not produce a zero signal level. This is addressed in the following section.

5.4.2 Background Image

The instantaneous data presented above were based on LII images that were corrected for the camera's dark noise background (see Chapter III). However, the instantaneous images contain not only LII signal but also flame luminosity, which represents an additional background signal that must be removed. The problem is that separate images of the instantaneous flame luminosity were not acquired simultaneously with the LII measurements (e.g., this would have required a second camera). These images were acquired with the laser off, but all other experimental/data acquisition parameters remained unchanged. While the luminosity signals were generally much less than the peak LII signals, the luminosity images do exhibit significant shot-to-shot variations (similar to what was seen in the LII images). Thus averaging the luminosity

background images (the method used for the average LII measurements) is not a proper way to correct the instantaneous LII data. In addition, the luminosity can comes from the complete flame volume, not just the two-dimensional region of the laser sheet-based LII measurements. So the flame luminosity is not just some simple fraction of the LII signal.

In order to separate the instantaneous LII and flame luminosity signals, the cumulative distribution function of the background images was examined. This function is given by:

(Eq.5-5) $$y(x) = \frac{1}{N}\sum_{i=0}^{x} N_i \times 100$$

where x is a given intensity level (e.g., in camera counts), N_i is the number of pixels with x counts, N is the total number of pixels, and therefore $y(x)$ is the percentage of the pixels with intensity below x.

Figure 5-23 shows the cumulative distribution function of the luminosity background images (after correction for the dark camera background), for both laminar and transitional flames in forced and unforced situation. In this representation, the signal level has been converted to equivalent soot concentration using the same calibration applied to the LII data. It is can be seen that almost all background signals are less than 6.2ppm (6700 counts). For the laminar flame, 93% of the pixels have soot concentration below 1.98ppm; while 94% of the measurements are below 1.98ppm in the transitional case. That is to say, if the signal below 1.98ppm is neglected for each instantaneous image, 93% of the pure luminosity signals will be discarded in laminar flame case, and 94% in transitional cases. Therefore there is a reasonable probability that soot concentration of 1.98ppm or below in the LII measurements may result from background luminosity. So in the instantaneous LII measurements, concentrations below 1.98ppm are

discarded, with only higher values likely to be valid soot measurements. Of course, some of the soot information may be discard in the process, but it should be a minor effect, since most of highly sooty regions have much higher concentrations, as shown in the previous distributions (Figure 5-21 and Figure 5-22). In the following sections, the effect of background luminosity on the soot distributions is examined.

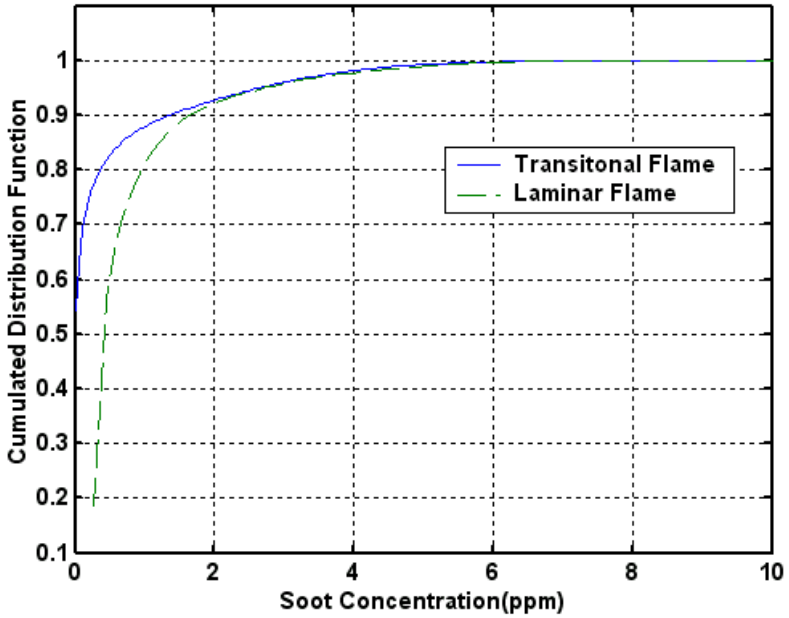

Figure 5-23. Laminar and transitional flame background image cumulative distribution function (x-axis shows the calibrated soot concentration).

5.4.3 Conditional PDFs

As noted previously, the soot PDFs presented in Section 5.4.1 depend on the size of the ROI used to produce them. On the other hand, if only the regions (pixels) where soot is actually present are included in the calculation, a better representation of how forcing effects the relative amount of high soot concentration can result. Thus, conditional soot concentration PDFs are considered; these statistics include only measurements where the concentration is above 1.98ppm, the threshold found from the background luminosity statistics.

Figure 5-24 and Figure 5-25 show conditional PDFs for the laminar and transitional flame cases. All the conditional PDFs have the same shape as the standard PDFs presented previously, just the magnitudes are changed due to the total number of pixels being reduced by the conditioning. Compared to the unconditional PDFs, the conditioned laminar results (Figure 5-24) for forcing at the 0º phase now more closely resemble the other forcing cases (72º and 144º). It is now possible to conclude that acoustic forcing tends to reduce the relative occurrence of high levels of soot (above 25ppm), while increasing the relative amount of soot at 10-25ppm. This is in contrast to the other possibility, that acoustic forcing simply reduces the physical extent of the soot region, but does not alter the distribution. The greatest shift (peak soot reduction) occurs for the 72° case, which corresponds to the point where the total soot mass in the flame drops dramatically (Figure 5-5), while the 0° phase produces the smallest shift.

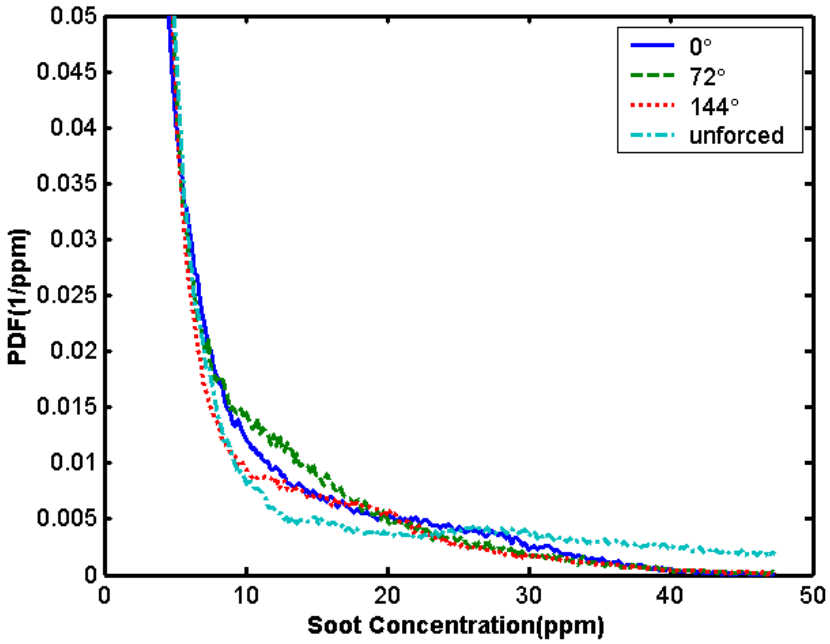

Figure 5-24. PDF of the soot concentration, conditioned on the concentration being > 1.98 ppm, for the laminar flame cases.

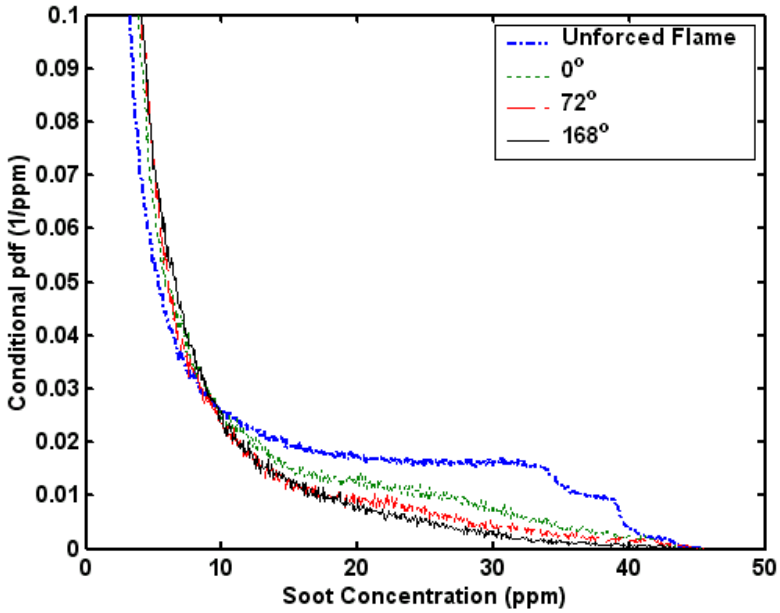

Figure 5-25. PDF of the soot concentration, conditioned on the concentration being > 1.98 ppm, for the transitional flame cases.

For the transitional flame, the conditioned PDFs (Figure 5-25) are very similar to the standard PDFs (Figure 5-22); the largest difference is that the probabilities for the unforced and forced cases are closer for the conditioned statistics. There is still a significant reduction in the relative amount of high soot levels (>10 ppm) with forcing. Thus it can be concluded that acoustic forcing is highly effective in reducing the likelihood of finding "peak" soot concentrations. Forcing likely reduces the amount of time that soot spends in hot, oxidizer free regions that favor soot growth. The 72° and 168° cases show similar effectiveness in redistributing the soot, while at 0° phase there is less redistribution, again in agreement with the variation of total soot mass (Figure 5-6).

5.4.4 CDFs

To examine how each soot concentration contributes to the total mass of soot, an alternate statistical function is useful; it is the concentration weighted cumulative

distribution function (CDF). The total fraction of soot mass below a given soot concentration *c* can be expressed as:

(Eq..5-6)
$$CDF(c) = \int_0^c xf(x)dx \Big/ M_{soot}$$

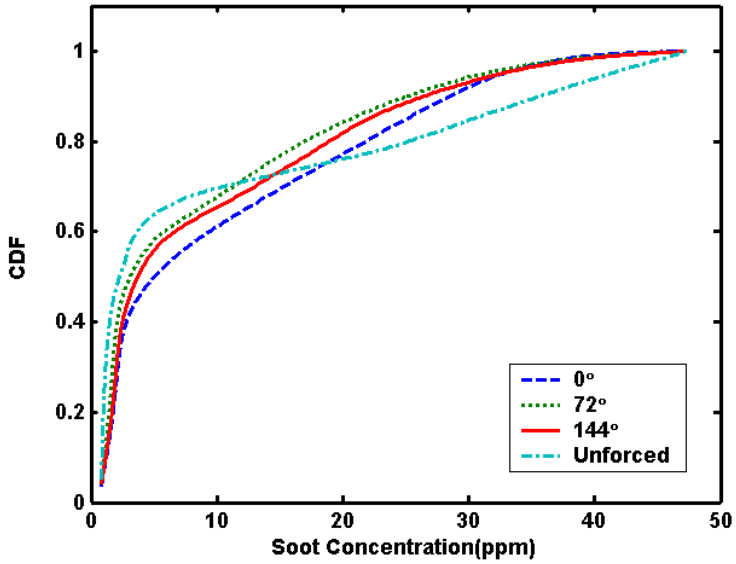

Figure 5-26.Mass weighted cumulate distribution function (CDF) for unforced and forced laminar flame cases.

Figure 5-26 shows the unconditioned CDFs for the laminar flames. It can be seen that the low soot concentration area contributes a large portion of the total amount of soot for the laminar cases, as much as ~40%. After a sharp increase at ~4ppm, the slopes of all the curves decrease, with the unforced data having the lowest slope. Below 20ppm, the weighted CDFs of the forced flame are higher than for the unforced case, with the trend reversing above 20 ppm. Thus the total amount of soot in the unforced laminar flame is higher both in the high (>25ppm) and low (<5ppm) soot concentration regions. As seen in the conditioned PDFs, the unsteady forcing preferentially decreases the amount of soot in the high concentration range. However, this does not mean the removal of high soot concentrations by simple dilution. The total measured soot mass decreased by a factor of

four with acoustic forcing; thus, most of the unforced flame soot was prevented by the unsteadiness induced by forcing. The different phases for forcing show the strongest effects for 4~30ppm instead of that variation around 10~25ppm in laminar conditional PDFs It is likelihood due to the background effect Among the three forcing phases, 72° shows the largest fraction of mass below 4ppm. This implies it has more area of pixels at the low soot concentration range, which causes it has the largest portion of soot , i.e >50%, in those low concentrate soot range, while 144° has soot mass portion <50% and 0° has 40% soot there. Overall, this implies the background takes more effect than that in the PDFs processing, at least in laminar flame case.

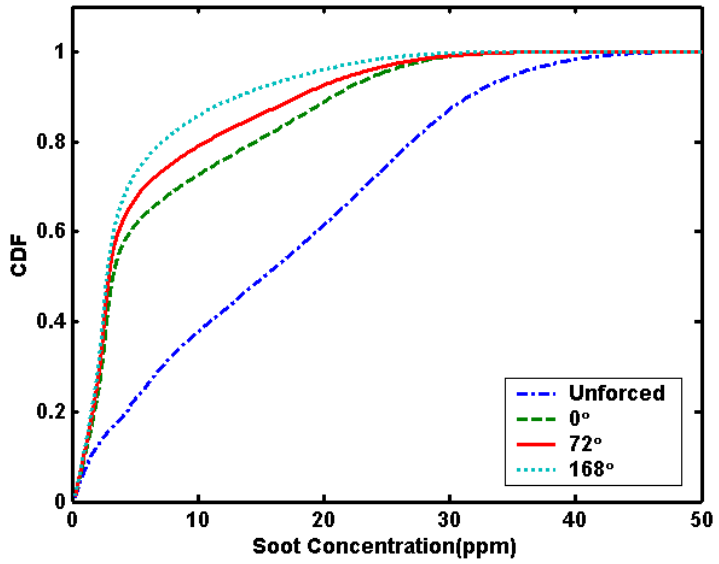

Figure 5-27. Cumulate Distribution Functions for transitional flame.

The transitional flame CDFs are shown in Figure 5-27. The three phases for the forced case have CDFs that are very similar. Below 10 ppm, the incline is steep. While for 10-30ppm, the increase slows down, and CDF nearly reaches a maximum. So for the forced transitional flames, soot above 30ppm contributes little to the soot mass, which is consistence with the PDF results. The unforced flame CDF is much different; it only has

a very small portion of its total soot mass (<10%) at low soot concentration levels (< 2ppm). For 2-40ppm, there is a nearly linear increase, and after that the CDF quickly plateaus. The unforced CDF is also above the forced CDFs. In addition, the forced CDFs show a variation with acoustic phase similar to the PDFs; the 168º CDF is most weighted towards the low soot concentration.

Notice for the process data set of transitional , the forced flame images only have around 1/3 of the original flame size, while the lost 2/3 flame size only have background information. It is kind of "background correction". That is to say, the transitional data sets have much less background problem than the laminar flame, thus, the transitional CDFs show much consistence with its conditional PDFs plot.

5.5 SUMMARY

In this chapter, quantitative soot concentrations have been measured, in forced and unforced flames, at laminar and transitional conditions. It is found acoustic forcing can reduce soot mass while increase soot temperature simultaneously. During acoustic forcing, periodically generated vortex can wrap fuel/air and produce multilayer thin and small diffusion flames, thereby improve globe mixing and reaction rate, reduce total mass of soot. At mean time, soot produced in thinner flame front can reach higher temperature.

CHAPTER 6

CONCLUSIONS AND RECOMMENDATIONS FOR FUTURE WORK

6.1. CONCLUSIONS

There were two primary objectives of this research work: (1) to develop an approach for soot velocity measurements that is compatible with LII, the leading method for making two-dimensional soot concentration measurements, and (2) to study how excitation is able to reduce soot in an acoustically forced burner by applying these quantitative soot measurement techniques.

6.1.1 Particle Vaporization Velocimetry (PVV) Development

A novel velocimetry technique, PVV, has been developed. It is a flow tagging approach based on vaporization of soot. PVV has been characterized and tested in a nonreacting laminar soot generator and a calibrated laminar diffusion flame. Additionally, PVV was extended for two-dimensional (and two-component) velocity measurements inside an acoustically excited burner.

To characterize the PVV technique, the laser intensity necessary to tag a soot region and the lifetime of the tagged region were studied. In addition, different detection methods for imaging the tagged area were studied. The results from both the soot generator and laminar flame suggest that at a fluence of 2-3 J/cm^2, the energy in the center of a roughly Gaussian beam profile is sufficient to nearly completely vaporize the

soot particles. The similarity in contrast at the higher laser fluences for both LII and scattering detection indicates that the particles are truly vaporized. While higher laser fluences can be used, they provide little added capability. The long life time of the tagged region provides the ability to make measurements over a wide range of velocities. In the absence of turbulent mixing, the measured lifetime of the tagged region was as long as 10 ms; though a shorter delay of ~1 ms was found to be optimum for local velocity measurements in the flows with *O*(1m/s) conditions, because longer delays ends up spatially averaging the velocity field.. For detection of the PVV tagged region, LII was found superior to simple particle scattering. LII generally has less background than scattering detection, therefore it is easier to identify the tagged region. This in turn produces a more reliable, less uncertain velocity.

The major sources of uncertainty for PVV result from minimum detectable displacement, which can be improved by increasing the detector resolution, and the presence of soot, since the measurement only works where soot is present. Laser perturbations to the flowfield (e.g., temperature, velocity, and pressure) are estimated to be small in typical conditions, though vaporization of the soot in flames clearly seems to inhibit production of new soot, possibly due to the C_2 radicals produced. Thus some chemical perturbation of the soot vaporized region is likely.

PVV also has some advantages over the most common method for velocity imaging in combustion flows, particle image velocimetry (PIV). PIV requires no more than one particle per pixel, and thus external seeding is necessary to determine velocity in sooty flows. A standard particle size for tracking velocity in most combustors is 0.2-1 μm. However, the scattering from such a particle would be 100× less than the scattering from

typical flame soot particles at 1 ppm with a PIV detector resolution of 10 μm/pixel. So PIV would have trouble discriminating the seed particle signal from the background soot scattering.

Thus PVV appears to be a viable method for velocity field measurements in the flame and product zones of combustors and in combustor and engine exhaust flows without the requirement for particle addition. Of course, there must be soot particles present in the flow. This is not a severe limitation, however, for many practical combustors. All that is required is a soot volume fraction above ~10 ppb, a concentration obtained in most combustors burning liquid hydrocarbon fuels, non-premixed gaseous hydrocarbon fuels (except perhaps for methane and ethane) and for turbine-engine combustor, which operate at high pressure. In fact, a small company (Metrolaser, Inc.) in cooperation with Georgia Tech developed a combined soot concentration and velocity measurement system for application in AEDC (Arnold Engineering Development Center) aircraft jet engine test cells using the LII and PVV approach. [5,84]

6.1.2 Unsteady Soot Measurements

Quantitative soot concentration measurements of a diffusion flame in an acoustically excited burner were obtained. These soot measurements were obtained in both natural (unforced) and acoustically forced, nonpremixed acetylene jet flames. Two (jet) Reynolds number cases were studied: one laminar and the other in a transitional range between laminar and fully turbulent. Broadband luminosity was also measured under each of these conditions. PVV measurements at slightly different conditions were also obtained.

The two-dimensional velocities in the flowfield of the forced flame showed the soot was primarily contained in rotating (vortical) structures. The total soot mass inside the flame was decreased by forcing; the drop was 4× for the laminar flame and 3× for the transitional flame. The total soot mass was also found to vary with acoustic forcing cycle. The total (time averaged) luminosity data indicated that the soot in the forced flames was generally hotter than in the unforced flames. Inside the unforced laminar flame, the (instantaneous) peak soot concentration is much higher than in the unforced transitional flame; while after acoustic forcing, peak soot levels in both laminar and transitional flames are decreased to about the same value (~40 ppm). The general decrease in the amount of high soot concentration region suggest that acoustic forcing can reduce the soot residence time in regions that favor soot growth. Inside the higher *Re* transitional flame, acoustic forcing reduce the peak soot level from ~45 ppm to 38 ppm. In addition, multiple-layer soot structures were observed in the soot concentration images.

The combined results suggests that with strong acoustic forcing the total velocity gradient near the jet exit is enhanced via periodical variation of acoustic velocity, and vortices are created periodically. These vortices can wrap up the fuel jet and the surrounding air flow, forming rollup structures that stretch the original fuel jet to thinner layers. It is reasonable to suggest that the high, instantaneous soot concentration regions in the forced flames are produced from a diffusion flame, but that the thinned flame provides less time for soot pyrolysis as the reduced distance between the fuel and oxidizer increases diffusion rates. Thus these periodically generated vortex structure can enhance overall reaction rates and decrease flame length and unburned fuel residence

times. In addition, most of the soot exists quite close to the high temperature flame zone, resulting in the increased luminosity to soot mass ratio.

There may be some partial premixing near the fuel jet exit, where only soot and hot products and fuel can exist after the heat release reactions (<1ms). The time it takes these soot regions to appear after the fuel leaves the jet exit (2-4 ms) is sufficient for soot nucleation and initial growth. The slow decrease in soot concentration as the vortex structures convect downstream may result from insufficient initial air entrainment. Once the thinned fuel air layers have reacted, the now thicker regions of excess fuel, soot and hot products oxidize as ambient air is entrained into the vortex.

Clearly acoustic forcing can reduce soot emissions from a combustor, while simultaneously increasing the radiative heat transfer per unit mass of soot. For laminar flames, this leads to an increase in total soot radiation, but for sufficiently unsteady flames, the total radiative load is decreased. For nonpremixed, turbulent (unforced) flames, similar flow field processes could be expected to play roles in soot formation, oxidation and radiation. Thus acoustic forcing is likely to be less effective in reducing soot for highly turbulent combustors.

6.2. RECOMMENDATION FOR FUTURE WORK

By improving the resolution of the multipoint (two-dimensional, 2-d) PVV technique, more local velocities can be measured instantaneously. This would be especially useful in studying unsteady soot flowfields, where more extensive velocity profiles are needed. This improvement can be achieved by utilizing more powerful marking laser sources, which could produce more marking beams with the required vaporization energy. Since a relatively small Nd:YAG laser was used here, this is not

difficult. Also, more efficient means are needed for producing multiple beams, e.g., through the use of single optical elements that contain a matrix of lenses. In addition to further examine the 2-d PVV technique, it may be useful to compare PVV measurements to PIV results in the same unsteady flowfield.

One drawback of the current LII soot concentration measurements was the calibration. To achieve the best results, it would be useful in the future to calibrate the system with a well studied flame of the same fuel species as that used in the experiment.

To better study the vortex structures inside the acoustically forced flame, instantaneous flame velocity profiles (e.g., profiles at different forcing phases) would be helpful. Combined PIV and PVV velocity measurements may be useful, with PIV providing velocity data in regions of low soot concentration. These velocity measurement would be helpful in obtaining a better understanding of the vortex structure interaction with the soot formation process. Besides velocity measurements, additional measurements such as OH PLIF would also be helpful. The OH radical location can help determine the local flame surface and identify where soot is being oxidized.

REFERENCES

1 Wilson, R. and Spengler, J. (Ed.), "Particles in Our Air", *Harvard University Press*, 1996 p.41-62.

2 Klingenberg, H., "Automobile Exhaust Emission Testing: Measurement of Regulated and Unregulated Exhaust Gas Components, Exhaust Emission Tests", *Springer Series in Environmental Engineering*, Springer-Verlag, New York, pp.103-119, 1996.

3 Peter N. Spotts Does "dirty air cool the climate?" *Christian Science Monitor*, June 30, 2005.

4 www.environmentcalifornia.org/reports/clean-air/clean-air-program-reports/clean-air-for-california-cutting-health-threatening-air-pollution-50-by-2010, Jan.20 2006.

5 Jenkins, T. P., Bartholomew, J.L., DeBarber; P. A., Yang, P. Seitzman, J.M.,. Howard, R. P., "Laser Induced Incandescence for Soot Concentration Measurements in Turbine Engine Exhausts*," 40th Aerospace Sciences Meeting & Exhibit*, Reno, Nevada, *AIAA* 2002-0828, 14-17 Jan. 2002.

6 Richter, H., Howard, .J.B. "Formation of polycyclic aromatic hydrocarbons and their growth to soot - a review of chemical reaction pathways", *Progress in Energy and Combustion Science,* Vol. 26 pp. 565–608, 2000.

7 Mansurov Z.A.Soot Formation in Combustion Processes (Review) Combustion, Explosion, and Shock Waves, .v. 41, No. 6, pp. 727–744, 2005.

8 Homann K.H., Wagner H.Gg. "Some new aspects of the mechanism of carbon formation in premixed flames" *11th Symposium (International) on Combustion*, the Combustion Institute, Pittsburgh, pp.371–379, 1967.

9 Crittenden, B. D, Long, R. "Formation of polycyclic aromatics in rich premixed acetylene and ethylene flame", *Combustion and Flame,* Vol. 20, pp359–68, 1973.

10 Violi, A. Voth, G.A.; Sarofim, A.F. "The relative roles of acetylene and aromatic precursors during soot particle inception", *Proceedings of the Combustion Institute*, Vol. 30, pp 1343-1351, 2004.

11 T. G. Benish, A. L. La.eur, K. Taghizadeh, and J. B. Howard, C2H2 and PAH as soot growth reactants in premixed C2H4–air flames", *Proceedings of the Combustion Institute*, Vol. 26, pp2319–2326, 1996.

12 Kazakov, A and Frenklach, M. "On the relative contribution of acetylene and aromatics to soot particle surface growth", *Combustion and Flame*, Vol.112, pp. 270–274, 1998.

13 M. Frenklach, "Reaction mechanism of soot formation in flames", *Journal of Physical Chemistry*, Vol. 4, pp 2027-2037, 2002.

14· Magnussen, B. F.; Hjertager, B. H.; Olsen, J. G.; Bhaduri, D. "Effects of Turbulent Structure and Local Concentrations on soot Formation and Combustion in C2H2 Diffusion Flames" *17th Symposium (International) on Combustion*, Leeds, England p1383-1393, 1979.

15 Sunderland,P.B., and Faeth, G. M., "Soot Formation in Hydrocarbon/Air Laminar Jet Diffusion Flames", *Combustion and Flame*, Vol. 105, Nos. 1/2, pp. 132–146, 1996.

16 El-Leathy, A. M., Xu, F. Kim, C. H, and Faeth, G. M. "Soot Surface Growth in Laminar Hydrocarbon/Air Diffusion Flames" *AIAA Journal* Vol. 41, No. 5, May 2003.

17 Weinberg, F.J., "The First Half-Million Years of Combustion Research and Today's Burning Problems" *Progress in Energy and Combustion Science*, Vol.1 pp.17-31, 1975.

18 Osborne Rynolds "An experimental investigation of the circumstances which determine whether the motion of water shall be direct or sinuous and of the law of resistance in parallel channels". *Royal Society*, Phil. Trans., 1883.

19 Pope, S. B., "Turbulent Flows" *Cambridge University Press*, Chapter 1, 2000

20 Crow SC; Champagne FH "Orderly structure in jet turbulence" *Fluid Mechanics,* Vol. 48, pp.547-591, 1971

21 Sarohia V; Bernal L.P. "Entrainment and mixing in pulsatile jets" *Third Symposium on Turbulent Shear Flows*, pp.11.30–11.35, 1981.

22 Swanson T.R., Richards C.D. "The structure of an acoustically forced, droplet-laden jet". *Atomization and Spray*, Vol. 7, pp. 561-579, 1997.

23 Meyer, T.R. Dutton, J.C. and Lucht, R.P. "Vortex interaction and mixing in a driven gaseous axisymmetric jet" *Physics of Fluids*, Vol. 11, No.11, pp.3401-3415, 1999.

24 Cho, S.K. Yoo, J.Y. Choi, H."Vortex Pairing in an axisymmetric jet using two-frequency acoustic forcing at low to moderate strouhal numbers", *Experiments in Fluids,* Vol. 25, pp.305-315, 1998.

25 Schram, C. Riethmuller, M.L. "Measurement of vortex ring characteristics during pairing in a forced subsonic air jet" *Experiments in Fluids*, Vol. 33, pp. 879–888, 2002.

26 Necker, H.A. and Liang, D. "Soot Emission, Thermal Radiation, and Laminar Instability of Acetylene Diffusion Flames" *Combustion and Flame,* Vol.52 pp.247-256, 1983.

27 Mcmanus, D.R. Vandsburger, U. and Bowman, C.T. "Combustor Performance Enhancement Through Direct Shear Layer Excitation" *Combustion and Flame,* Vol. 82, pp.75-92, 1990.

28 Santoro, R. J., Yeh, T. T., Horvath, J. J., and Semerjian, H. G., "The Transport and Growth of Soot Particles in Laminar Diffusion Flames", *Combustion Science and Technology,* Vol. 53, pp. 89-115, 1987.

29 Smyth, K.C., Harrington, J.E. *et al* "Greatly Enhanced Soot Scattering in Flickering CH4/Air Diffusion Flames*" Combustion and Flame,* Vol. 95, pp. 229-239, 1993.

30 Shaddix, C. R., and Smyth, K.C. "Laser-Induced Incandescence Measurements of Soot Production in Steady and Flickering Methand, Propane, and Ethylene diffusion Flames" *Combustion and Flame*, Vol.107, pp. 418-452, 1996.

31 Zinn, B.T., "Pulse Combustion: Resent Applications and Research Issues", *24th Symposium (International) on Combustion*, The Combustion Institute, pp. 1297-1305, 1992.

32 Kim, T.K., Park, J. and Shin, H.D, "Mixing Mechanism near the Nozzle Exit in a Tone Excited Non-Premixed Jet Flame" *Combustion Science and Technology*, Vol. 89, pp.83-100, 1993.

33 Chen, L.D., Seaba, J.P. "Buoyant Diffusion flames," *22nd Symposium (international) on Combustion*, the combustion institute, Pittsburgh, pp. 677, 1988.

34 Gebhart, B., and Mahajan, R. "Characteristic disturbance frequency in vertical natural convection flow", *International Journal of Heat Mass Transfer,* Vol.18, pp. 1143.-1148, 1975.

35 O.A. Ezekoye, K.M. Martin, F. Bisetti "pulsed flow modulation of soot production in a laminar jet-diffusion flame" *Proceedings of the Combustion Institute* Vol.30 pp1485–1492, 2005.

36 Jagoda, J., private communication.

37 Dobbins, R. A., Fletcher, R. A., and Lu, W., "Laser Microprobe Analysis of Soot Precursor Particles and Carbonaceous Soot", *Combustion and Flame*, Vol.100, pp. 301-309, 1995.

38 Köylü, Ü. Ö., McEnally, C. S., Rosner, D.E., and Pfefferle, L. D., "Simultaneous Measurements of Soot Volume Fraction and Particle Size/Microstructure in Flames Using a Thermophoretic Sampling Technique*," Combustion and Flame*, Vol. 110, 494-507, 1997.

39 Puri, R., Richardson, T. F., Santoro, R. J., and Dobbins, R. A., "Aerosol Dynamic Processes of Soot Aggregates in a Laminar Ethene Diffusion Flame," *Combustion and Flame* Vol. 92, pp. 320-333, 1993.

40 Van de Hulst, H. C., *Light Scattering by Small Particles*, Dover Publications, New York, 1981.

41 Eckbreth, A.C., "Effects of Laser Modulated Particulate Incandescence on Raman Scattering Diagnostics", *Journal of Applied Physics*, Vol. 48, pp 4473-4479, 1977.

42 Melton, L.A "Soot Diagnostics Based on Laser Heating" *Applied Optics*, Vol.23, pp.2201-2208,1984.

43 Taylor, A. M. K. P. ed., *Instrumentation for Flows with Combustion*, Academic Press, London, 1993.

44 Willert, C. E. and Gharib, M., "Digital Particle Image Velocimetry," *Experiments in Fluids*, Vol. 10, pp. 181-193 1991.

45 Buchhave, P., "Particle Image Velocimetry – Status and Trends" *Experimental Thermal and Fluid Science* Vol. 5, pp. 586-604, 1992.

46 Palmer, H. B. and Cullis, H. F., "The formation of carbon from gases" *Chemistry and physics of carbon*, Vol. 1, pp. 265-325, 1965.

47 Gaydon AG. *Spectroscopy and combustion theory*. London, Chapman and Hall, 1948.

48 Bockhorn H, editor. Soot formation in combustion: mechanisms and models, Berlin: Springer, 1994.

49 Richter, H., Howard, .J.B. "Formation of polycyclic aromatic hydrocarbons and their growth to soot - a review of chemical reaction pathways**"** *Progress in Energy and Combustion Science*, Vol.26, pp.565–608, 2000.

50 Homann, K. H., Wagner H. Gg., "Some new aspects of the mechanism of carbon formation in premixed flames". *11th Symposium (International) on Combustion*, the Combustion Institute, Pittsburgh, pp. 371–379, 1967.

51 Glassman, I., "Sooting Laminar Diffusion Flames: Effect of Dilution, Additives, Pressure and Microgravity" *27th Symposium (International) on Combustion*, the Combustion Institute, Boulder, pp. 1589–1596, 1998.

52 Garo, A., Said, R. and Borghi, R., "Model of soot formation: coupling of turbulence and soot chemistry" *Soot formation in Combustion*, Springer-Verlag, Berlin, 1994.

53 Smooke, M.D., *et. al.* "Soot formation in laminar diffusion flames" *Combustion and Flame,* Vol.143 pp 613–628, 2005.

54 Bockhorn, H. "Ultrafine particles from combustion sources: approaches to what we want to know", *Philosophical Transactions of the Royal Society of London Series A-Mathematical*, *Physical and Engineering Sciences*, 2000, No. 358, pp 2659-2672, 2000.

55 Smith, George W. "Kinetic Aspects of Diesel Soot Coagulation"**,** *Proceedings - Society of Automotive Engineers*, pp 299-309, 1982.

56 Eckbreth, A.C., "Effects of Laser Modulated Particulate Incandescence on Raman Scattering Diagnostics", *Journal of Applied Physics*, Vol. 48, pp 4473-4479, 1977.

57 "Soot Diagnostics Based on Laser Heating" *Applied Optics*, Vol.23, pp.2201-2208,1984.

58 Hofeldt, D.L., "Real-time Soot Concentration Measurement Technique for Engine Exhaust Streams", *SAE paper,* 930079, 1993.

59 Mewes, B. and Seitzman, J. M. "Soot Volume Fraction and Particle Size Measurements with Laser-Induced Incandescence", *Applied Optics*, Vol. 36, No.3 pp709-717, 1997

60 McCoy, B.J., and Cha, C.Y., "Transport phenomena in the Rarefied Gas Transition Regime", *Chemical Engineering and. Science*, Vol.29, pp381-388, 1983.

61 Siegel, R., and Howell, J.R., *Thermal Radiation Heat Transfer*, 3rd edition, Hemisphere Publishing Corporation, Washington, 1992.

62 Miles, R. B., Zhou, D., Zhang, B., Lempert, W. R.and She, Z., "Fundamental Turbulence Measurements by Relief Flow Tagging," *AIAA Journal*, Vol. 31, pp. 447-452, 1993.

63 Pitz, R. W., Brown, T. M., Nandula, S. P., Skaggs, P.A., DeBarber, P. A. and Brown, M. S., "Unseeded Velocity Measurement by Ozone Tagging Velocimetry," *Optics Letters,* Vol. 21, pp. 755-757 1996.

64 Stier, B. and Koochesfahani, M. M., "Molecular Tagging Velocimetry (MTV) Measurements in Gas Phase Flows," *Experiments in Fluids,* Vol. 26, pp. 297-304, 1999.

65 Dasch, C. J., "Continuous-Wave Probe Laser Investigation of Laser Vaporization of Small Soot Particles in a Flame," *Applied Optics,* Vol. 23,pp. 2209-2215, 1984.

66 Santoro, R. J., Yeh, T. T., Horvath, J. J. and Semerjian, H. G., "The Transport and Growth of Soot Particles in Laminar Diffusion Flames," *Combustion Science and Technology* Vol. 53, pp. 89-115, 1987.

67 Megaridis, C. M. and Dobbins, R. A., "Comparison of Soot Growth and Oxidation in Smoking and Non-Smoking Ethylene Diffusion Flames" *Combustion Science and Technology*, Vol. 66, pp. 1-16, 1989.

68 Wainner, R. T. "An Analytical and Quantitative Analysis of the Laser Induced Incandescence of Soot", *Ph.D. thesis*, Appendix B, Georgia Institute of Technology, 1999.

69 Greenberg, P. S. and Ku, J. C., "Soot Volume Fraction Imaging" *Applied Optics*, Vol. 36, No. 22, pp. 5514-5522, August, 1997.

70 Allen, T., *Particle Size Measurement*, 4th Edition. Chapman and Hall, London, 1990.

71 Randy L. Vander Wal and Mun Y. Choi "Pulsed laser heating of soot: morphological changes" Carbon, Vol. 37, Issue 2 , pp. 231-239, February 1999.

72 Leider H. R., Krikoria O.H., Young D.A., "Thermodynamic Properties of Carbon Up to Critical-Point", *CARBON* , Vol.11, No. 5, pp 555-563, 1973.

73 Bengtsson, P.-E., Alden M.J., "Soot-visualization strategies using laser techniques laser-induced fluorescence in C2 from laser-vaporized soot and laser-induced soot incandescence" *Journal of Apply Physics*. *B: Lasers and Optics*, Vol. 60, No.1, pp 51-59 Jan, 1995.

74 Greenhalgh, D.A.,"RECLAS: resonant-enhanced CARS from C2 produced by laser ablation of soot particles", *Applied Optics*, Vol. 22, No. 8, pp 1128-1130, Jan. 1983.

75 Larsson, G., "The C3 molecule: A Literature Study and Spectroscopic Investigations in Flames and on Graphite", *Lund Reports on Combustion Physics*, LRCP-82, 2002.

76 Walewski J, Rupinski M, Bladh H, *et al.*"Soot visualisation by use of laser-induced soot vapourisation in combination with polarisation spectroscopy", *Applied Physics B-Laser and Optics*, Vol.77 No.4, pp447-454, Oct 2003.

77 Michelsen, H. A.,"Understanding and Predicting the Temporal Response of Laser-Induced Incandescence from Carbonaceous Particles" *Journal of Chemical Physics*, Vol. 118, No. 15, pp. 7012-7045, April 2003.

78 Kruseand T., Roth P., "Kinetics of C2 Reactions during High-Temperature Pyrolysis of Acetylene", *Journal of Physical Chemistry A*, Vol.101, pp2138-2146, 1997.

79 Wang J. H., Han K. L., He G. Z., Li Z., Morris V. R., "Theoretical Study of the C2+H2O Reaction Mechanism", *Journal of Physical Chemistry A*, Vol.107, pp. 9825-9833, 2003.

80 Santoro, R. J., Yeh, T. T., Horvath, J. J. and Semerjian, H. G., "Soot Particle Growth and Transport in Laminar diffusion flames", *Combustion Science and Technology*. Vol. 53, pp.89,1987.

81 White, F. M., *Fluid Mechanics*, 4th edition, pp331, 1999.

82 Ezekoye, O.A., Martin, K.M., Bisetti, F., "Pulsed flow modulation of soot production in a laminar jet-diffusion .flame" *Proceedings of the Combustion Institute,* Vol. 30, pp. 1485–1492, 2005.

83 Kim, T.K., Park, J. and Shin, H.D, "Mixing Mechanism near the Nozzle Exit in a Tone Excited Non-Premixed Jet Flame", *Combustion Science and Technology*, Vol. 89, pp.83-100, 1993.

84 Jenkins, T. P., Bartholomew, J.L., DeBarber; P. A., Yang, P. Seitzman, J.M.,. Howard, R. P., "A Laser-Induced Incandescence System for Measuring Soot Flux in Aircraft Engine Exhausts", *AIAA/ASME/SAE/ASEE Joint Propulsion Conference*, Indianapolis, July 7-10, 2002.